Biophysical Studies of Ligand-gated Ion Channels

Thesis by

Betty K. Wong

In Partial Fulfillment of the Requirements for

the degree of

Doctor of Philosophy

CALIFORNIA INSTITUTE OF TECHNOLOGY

Pasadena, California

2017

(Defended May 22, 2017)

To my family:

婆婆, 爸爸, 媽媽, *Ada, and* 兩隻狗

ACKNOWLEDGEMENTS

There are many people to whom I want to give a bounty of thanks.

First and foremost, I want to thank my graduate advisor, Professor Dennis Dougherty, for his above-and-beyond support and guidance over the years. Dennis is a great man embodying great intellect, compassion, and sagacity. I am grateful to have an advisor with whom I can entrust my vulnerabilities with, knowing he would take that and help me grow. I am grateful for his discerning my strengths and believing in me. He empowered me to explore my curiosities – at and beyond the bench – with free rein. His support led to the culmination of this dissertation, as well as a skillset that goes beyond the science and theories described here.

My gratitude also extends to my second advisor, Professor Henry Lester, who adopted me into his lab. I respect his scientific dedication and keenness of mind. I have become a better scientist under his rigorous mentorship. I appreciate his candor most and allowing me to reciprocate this open communication. Running into him outside the lab, in the hallways, or at the gym, or while he was walking his precious puppy, was always a delight, sprinkled with enlightening scientific conversations. I always departed with a myriad of ideas and excitement to pursue them.

I am indebted to Dr. Brandon Henderson, a former member of the Lester Lab and my mentor, collaborator, and friend. Whenever I had a question, I could always drop by his desk; and when he left to become a professor, I could always call. Ultimately, his generosity with his time, help, and advice pulled me through my graduate studies, especially at the home stretch. The mentorship that he gave me in science and my personal life is priceless. Also, the work described in Chapters 5 and 6 would have been impossible without his edification and collaboration. Not once have I concluded a conversation without acquiring a greater breadth of knowledge or motivation. Grateful is an understatement.

I also am beholden to my graduate committee members. Professor Doug Rees has been a supporter since day one, that is, since interviewing me to being my option's faculty representative, committee chair, and graduate dean. I am also thankful to my thesis committee

member, Professor Viviana Gradinaru, and my candidacy committee members, Professors Frances Arnold and Dave Tirrell, for their generosity with time and attention.

Further, I am obliged to my amazing collaborators at USC – Dr. Cosimo "Mimmo" Arnesano, Dr. Francesco Cutrale, Dr. Jason Junge, and Professor Scott Fraser – for sharing with me their expertise, resources, and time. Mimmo and Francesco trained me when I was a complete novice in fluorescence microscopy. They patiently taught me through countless imaging sessions and stimulating discussions and via numerous emails of questions and answers. Completion of Chapters 2, 3, and 4 would not have been realized without them. Jason was a major contributor to the work described in Chapter 4, driving much of the experimental design and collecting the data together. Scott was generous to share the resources in his lab with me, namely the microscopes and his lab's expertise. I also want to thank Georgiann Keller for easing my travels by continually renewing my parking permits, as well as access to the building. Knowing these amazingly warmhearted people were there, the one-hour drive of 14 miles in traffic from Pasadena to USC became much less dreadful.

Furthermore, I want to thank those who helped shape the computational studies described in Chapter 6. My gratitude extends to Shyam Saladi, a computational superstar, for all his contributions in computational modeling; Professor Bill Goddard for his scientific advice and lending his lab's computing resources; and Dr. Soo-Kyung Kim and Daniel Brooks for helping troubleshoot my many computational problems. Concurrently, I want to thank Professor Steve Mayo for giving me access to his lab's computing resources.

Former and current members of the Dougherty Lab have together cultivated an incredible work environment. The lab itself is a great, big family with low barriers to frankness and even lower barriers to helpfulness. Dr. Clint Regan helped me with the synthesis of the fluorophore described in Chapter 2. He taught me much of what I know about practical organic chemistry, including synthetic design, NMR, and LC/MS, to name a few. Dr. Noah Duffy helped me with the synthesis of the unnatural amino acid described in Chapter 2, especially with designing the synthetic route. Dr. Ethan Van Arnam introduced me to TIRF. Dr. Tim Miles, Dr. Kristina Daeffler, Dr. Chris Marotta, Dr. Matt Rienzo, Dr. Oliver Shafaat, Matt Davis, and Paul Walton all welcomed me into their lab and trained me on many the techniques used for the

work described in this dissertation. Catie Blunt is a very kindhearted person and a great desk mate who always cheerfully kick-started my Mondays with a caring "How was your weekend?" – and thank you for saving my eyes in the chemistry lab. In addition, Matt Davis's humor, Paul Walton's eccentricity, Annet Blom's strong will, Bryce Jarman's camaraderie spirit, Richard Mosesso's pragmatism, Gabby Tender's pep, and Steve Grant's composure – all these people have created a great place for work, for at least 2,000 hours every year.

My sincere thanks extend to many members of the Lester Lab. Purnima Deshpande and Jonathan Wang, in particular, provided wonderful support, especially for all of my last-minute concerns and requests. Thank you, Jonathan, for the dog calendars. Charlene Kim, Matt Mulcahy, Aron Kamajaya, and Aaron Nichols were also delightful company.

Apart from the above, I want to thank many Caltech's staff members. In particular, I am grateful to Dr. Andres Collazo from the Caltech Biological Imaging Facility, who generously sacrificed his time to provide me with many insights in fluorescence microscopy. The CCE Department's administrative staff are laudable for their expeditious support and gracious care: Linda Syme, Joe Drew, and Anne Penney. A special recognition is extended to Alison Ross, who was my option administrator and more so a friend, whose office was always open to me for many splendid chats. I am grateful to Felicia Hunt, previously Assistant Dean and currently Title IX Coordinator, for providing me with an emotional and mental haven.

Although not directly related to this dissertation, receiving my master's degree in electrical engineering tremendously contributed to my intellectual tenure at Caltech. Thus, I would like to thank those who have made this achievement possible: Natalie Gilmore, Assistant Dean, for encouraging me to broaden my horizons and initiating the pursuit of the degree; Brian Hong for his brilliance and patience in teaching me many EE concepts; and my teaching assistant in EE111, Srikanth Tenneti, a great teacher. Innumerable classmates and professors also helped this scientist become a newly-minted engineer. Thanks to all of you.

Graduate school is a roller coaster ride. I lucked out to have been able to share the ride and many fond memories with my friends and confidants at Caltech. While these wonderful human beings were graduating one after the other, leaving Caltech to continue bettering this

world, I knew that my time at Caltech should be coming to an end as well. Dr. Liz Wang and Dr. Dr. Gloria Sheng have been my cheerleaders; and, undeniably, a sizeable piece of me became devoid of vitality when they graduated. First brought together through our passion for food and co-parenting of a kitten, I continue to feel the affinity of our bond through our shared outlook on relationships, kinship, and careers. Liz's fervent love for her job motivates me to never settle for anything less in my own career. Gloria's powerful empathic nature propels me to introspect deeply and treat others with compassion.

I am grateful for the friendship with Dr. Jackson Kenai Blender Cahn who has been my source of wit and a confidant during a rough transition in research directions. I am also blessed by the friendship with Dr. Victoria Hsiao for her steady stream of humor. Thank you to the ever-resilient Tami Khazaei for her unhindered friendship and fascinating storytelling. Additionally, with Dr. Emzo de los Santos, Dr. Seth Lieblich, Dr. Branimir Ćaćić, Dr. Devin Trudeau, Dr. Naeem Husain, Stephanie Barnes, Sandy Nandagopal, and Liz Jensen, I am grateful to have had such a wonderful excursion group for good food and movies. Moreover, Dingyi Sun, Shannon Stone, Blake Farrow, JingXin Liang, Sam Ho, Camille McAvoy, and a baker's dozen of people, thank you for celebrating with me my successes, commiserating with me over my setbacks, and making my life at Caltech a memorable joy. All in all, I am understating the meaningfulness of our friendships, as many of you have also inspired me through conversations about life, community, career, and beyond.

To my family who lives afar, but support is never subpar, the deepest thanks for everything is simply insufficient. I am immeasurably fortunate to have been able to visit my family many times throughout the years. Coming home to a table full of homemade food, smiles, love, warmth, and embraces—these allowed me to reset and tackle my research again with vigor. I am grateful that my parents learned how to use an iPhone and texted me mini stories and pictures of our lovely dogs—these pulled me through the tough days and made the good days even better.

Without my family as my role models, I would not have become the person I am today. I adopted wisdom from my dad, ambition from my mom, integrity from my sister, and rectitude from my grandma. I look up to my grandma for her grace. I look up to my dad, who defies the

meaning of the proverb ' 江山易改，本性難移 '. I look up to my mom, whose tenacity, determination, and integrity with work and family stand up to the test of time — 有其母必有其女. I look up to my sister for remaining resolute in helping those who have been overlooked and underserved, and for achieving her dreams of starting her own law firm at the age of 27 – it is no easy feat, and I am enormously proud to be her annoying little sister.

Thank you, tiger mom, for granting me the freedom to pursue anything that spanned from interest to passion and for giving me room to breathe when needed. Thank you for keeping my bedroom unchanged (but dusted). Thank you for engraving my mind with many Chinese proverbs and strong morals. Thank you for editing my English papers and the grammar in this acknowledgements section. Thank you for making this American-born Chinese bilingual.

To my parents, who immigrated here and dedicated their love and lives to this family, and to spoiling me, there is no one else that I would rather dedicate this Ph.D. to—than to them—Mama and Papa Wong.

I would end here, but for those who know me should know that I would also want to give special credit to all the food that kept me physically alive and satiated, in some particular order: my mom and dad's food that I'd drive 364 miles to eat, Ocean Star, Lunasia, Yama Seafood, Sushi Gen, Sushi Enya, Spicy City, UberEats, Wang Xing Ji, Benten Ramen, Tasty Noodle House, Suehiro, Boiling Crab, Raffi's Place, Marugame Monzo, Blaze Pizza, Factory Tea Bar, Fosselman's, Yangji Gamjatang, India's Restaurant, Mokkoji, A Ri Rang Tofu House, Young Dong Tofu, Korean BBQ, Houston's, The Athenaeum, Ralphs, Vons, and Ranch 99.

ABSTRACT

This dissertation describes building a methodology for and the biophysical studies of ligand-gated ion channels (LGICs).

The primary focus of the first half of this dissertation is on developing a fluorescence-based assay to broadly study LGICs. Chapter 2 describes the site-selective incorporation of a turn-on fluorophore via unnatural amino acid mutagenesis on the mouse muscle-type nicotinic acetylcholine receptor (nAChR) in *Xenopus laevis* oocytes as a proof-of-principle study. This method has proven to yield very low levels of undesired fluorescent background, which was a problem for previous incorporation techniques. Chapter 3 describes efforts towards imaging this in vivo system using lifetime imaging with efforts hampered by the inability to detect a clear signal. Chapter 4 describes efforts to apply the lifetime imaging approach towards a different system involving 5-HT_3 proteins fused to fluorescent proteins in COS-7 cells.

The second half of this dissertation focuses on studies of menthol, a flavorant added to cigarettes that contributes to smoking addiction, as a negative allosteric modulator of the $\alpha4\beta2$ nAChR. Chapter 5 reveals the stereochemical effects, or rather lack of, of menthol on the two stoichiometries of the $\alpha4\beta2$ receptor. Chapter 6 seeks to identify the residue interactions with menthol of the $\alpha4\beta2$receptor using a combination of computational and experimental studies.

TABLE OF CONTENTS

Chapter 1

INTRODUCTION

Neuronal membrane proteins serve vital physiological functions for the cell in our brains and body. They act at billions of synapses to enable rapid communication among networks of nerve cells. One subclass, called ion channels, plays a plethora of roles, including brain activity, light detection in the eye, and muscle contraction. They function as facilitators of diffusive ion transport across the cell's lipid bilayer to generate transient electrical signals, which in turn trigger downstream signaling events in the cell. Ion channel activity can be modulated directly by electrical, mechanical, or chemical signals. Receptors stimulated by small-molecule chemical signals, including neurotransmitters such as serotonin, dopamine, and acetylcholine, are called ligand-gated ion channels (LGICs) (Figure 1.1).[1-2]

Dysfunctional ion channels have been implicated in many human diseases, such as *M. gravis*, epilepsy, addiction, migraine, and pain excessiveness or insensitivity, making them regular targets for new drug design.[1-2] Unfortunately, currently available drugs are not fully efficacious and may also cause undesirable side effects.[2] Understanding the structures of ion channels and the molecular mechanisms that govern their functional properties can aid in designing better drugs.

Ligand-gated Ion Channels

The non-covalent binding of a natural small-molecule ligand, e.g., a neurotransmitter, induces an LGIC to undergo a transition into an ion-conducting state in most cases. In the ion-conducting state, ions such as Na^+, K^+, Ca^{2+}, and/or Cl^- are allowed to pass through (Figure 1.1). One superfamily of this class of ion channels comprises the Cys-loop receptors, which are the focus for this dissertation. The receptors of the Cys-loop superfamily are named after a characteristic loop that is formed by a disulfide bond between two cysteines in the extracellular domain (ECD) (Figure 1.2). These receptors can either be excitatory (depolarizing the membrane) or inhibitory (hyperpolarizing the membrane) to the neuron. The excitatory

receptors contain the cation-selective channels, including the nicotinic acetylcholine (nACh) and 5-hydroxytryptamine (type 3, 5-HT_3) receptors. The inhibitory receptors contain the anion-selective receptors, including the γ-aminobutyric acid (type A and C, $GABA_{A/C}$) and glycine receptors.

The Cys-loop receptors are pentameric, containing either five homologous (heteromeric) or identical (homomeric) subunits, each contributing to a β-sheet heavy ECD, α-helical transmembrane domain (TMD), and a smaller intracellular domain (ICD). The binding of a neurotransmitter at the interface of two subunits in the ECD can then cause a conformational rearrangement at the receptor gate ~60 Å away (Figure 1.3).

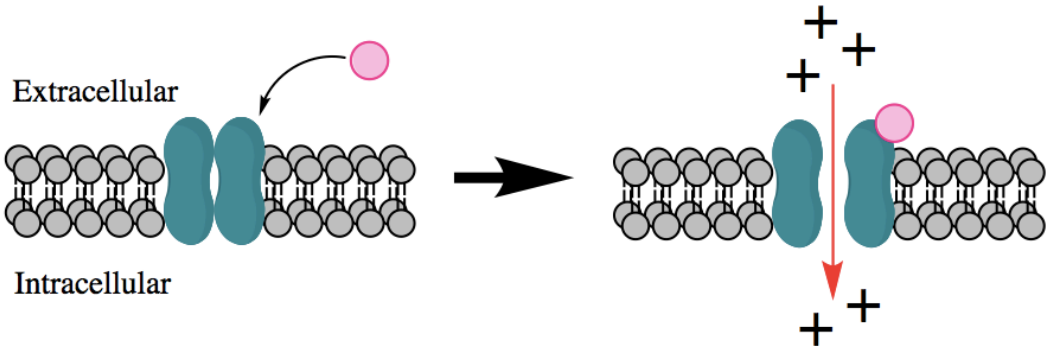

Figure 1.1. Ligand-gated ion channels. The binding of a neurotransmitter(s) induces the ligand-gated ion channel to adopt the ion-conducting, open state, allowing ions to pass through.

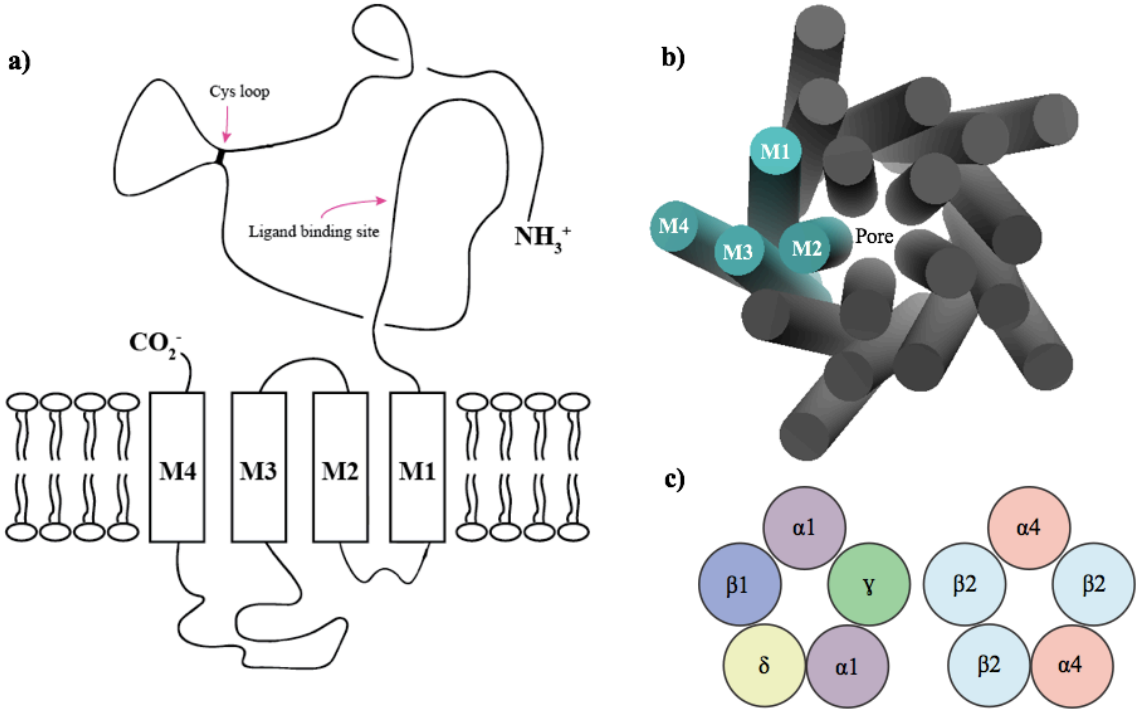

Figure 1.2. Structural arrangements of Cys-loop receptors. a) A representation of the homologous regions for a single subunit (adapted from Ethan Van Arnam's thesis)[3]. b) Transmembrane domain depicting the M1-M4 helices, where M2 lines the pore. c) Examples of the heteromeric arrangements of the mouse muscle nAChR $(\alpha1)_2\beta1\delta\gamma$ nAChR and the $(\alpha4)_2(\beta2)_3$ nAChR.

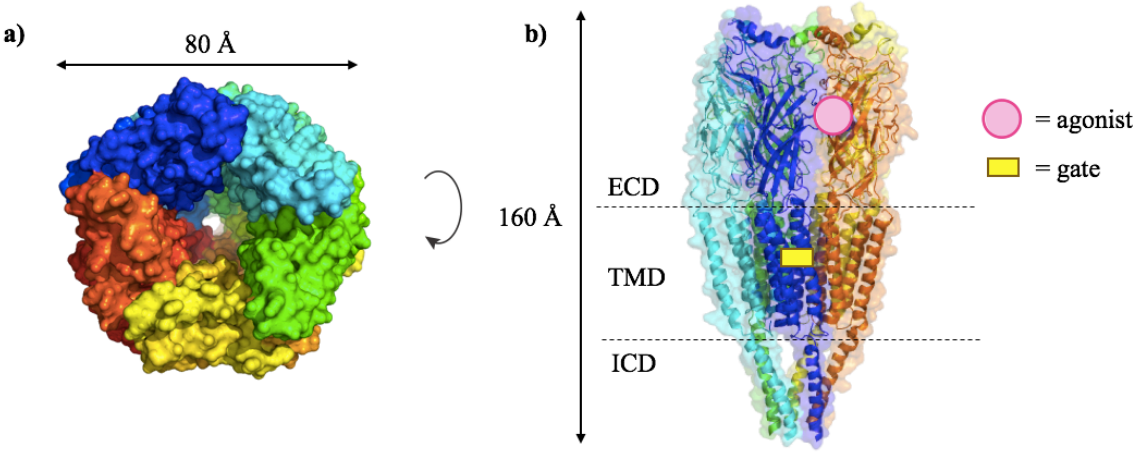

Figure 1.3. *Torpedo* nAChR EM structure.[4] a) View down the axis and b) from the side, parallel with the plasma membrane showing the agonist binding site and receptor gate. Protein figures constructed in PyMOL with PDB 2GB9.

LGIC Conformations

One part of this dissertation work is developing a methodology to study the conformational states of an LGIC. An ion channel can have multiple conformational states – at least one open state and one or two closed states – each stable conformation representing a different functional state. The three functional states are: closed and activatable (resting), open (active), or closed and non-activatable (refractory or desensitized).[1] Once open, the channel can remain open for several milliseconds before closing. Once closed, it can also remain closed for several milliseconds before reopening. The transition between these states is called *gating* and can occur virtually instantaneously (in less than 10 microseconds, the present limit of experimental measurements).[1] One model suggests that the ion-conducting pore, lined by the M2 helix, opens through a twisting motion of the extracellular domain coupled to the tilting of two M2 and M3 transmembrane helices (Figure 1.2).[5] Despite its functional importance, little is still known of the exact molecular mechanisms of gating.[1,5]

Gating mechanisms can be affected by desensitization, antagonist inhibition, and allosteric regulation. LGICs can undergo desensitization after prolonged exposure to the activating ligand, causing it to transition into the refractory state. A competitive antagonist can block the endogenous ligand by occupying its binding site. Some LGICs have an allosteric binding site that can affect the normal gating mechanisms as well.[1, 6] The molecular mechanisms underlying desensitization and allosteric modulation are not well understood. The following questions remain: what are the structures of desensitized states; what are the structural changes during gating; how large are these gating motions; and is there symmetry in the motion of the subunits during gating?

Allosteric Modulation

The second major area of this dissertation work is investigating menthol's role as a negative allosteric modulator to the nicotinic receptor. Neurotransmitters, i.e., agonists, have been the focus of ion channel gating. Allosteric modulators are also important in channel gating. Agonists bind at the receptor's orthosteric site, leading to activation, and antagonists can also bind here, leading to inactivation. Allosteric modulators are a class of ligands that can enhance

receptor activation (positive allosteric modulators) or reduce receptor function (negative allosteric modulators) indirectly by binding in locations adjacent to the orthosteric site or tens of angstroms away. The theory is that the allosteric molecule stabilizes a particular open, closed, or desensitized state or changes the energy barrier(s) for conformational changes. Allosteric modulators as drugs, such as the plant alkaloid galatamine which positively modulates the human α7 and α4β2 nAChRs, have been used to successfully treat neurodegenerative disorders. Allosteric modulators for ion channels are attractive candidates as drugs for treating many neurodegenerative diseases because they can be designed to have high specificity with low adverse off-target effects. An increasing body of research has accrued towards understanding positive and negative allosteric modulators for treating neurodegenerative diseases and addiction.[7]

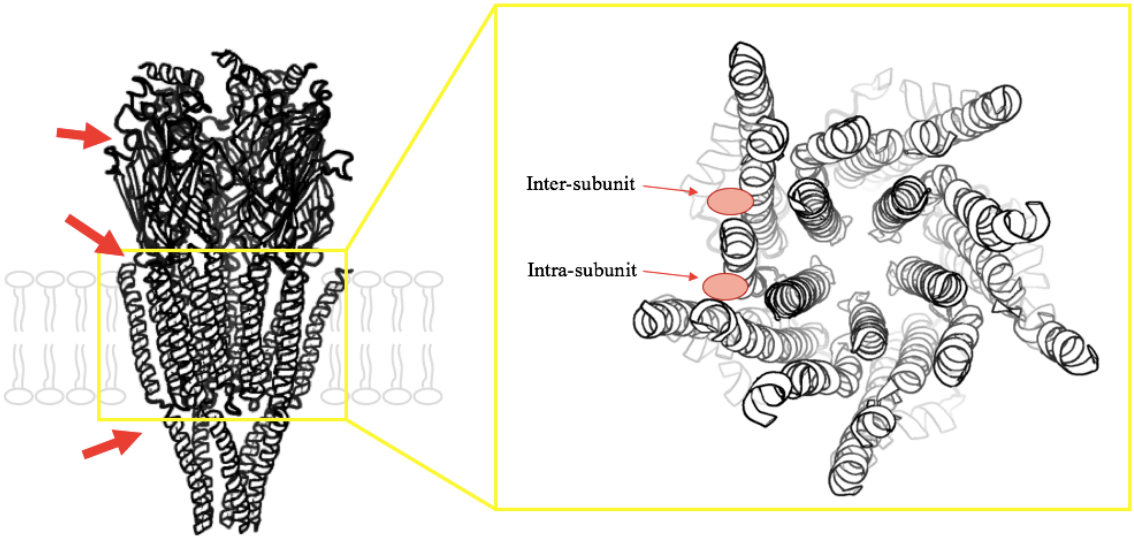

Figure 1.3. Locations of allosteric ligands. Putative-binding sites illustrated by arrows of allosteric modulators for a typical four transmembrane LGIC such as nAChR. Representation built based on Hogg, et al.[7]

Methods for Interrogating Structure and Function

Elucidating the structure and function of ion channels has been attempted with success using electron microscopy (EM), X-ray crystallography, electrophysiology, and mutagenesis. EM has revealed the overall topology of nAChR from the *Torpedo* electric organ, including the ECD, TMD, and ICD, and that it is formed by five subunits organized around a pseudosymmetrical

five-fold axis, forming a rosette cylinder that is ~8 nm in diameter and ~16 nm in length (Figure 1.2).[4] With X-ray crystallography, the crystal structure of the acetylcholine (ACh) binding protein (AChBP),[8] a homolog of the ECD of nAChR, the ECD of a single subunit (α1) of the mouse muscle nAChR[9], and the human α4β2 nAChR[10] was solved. The mouse nAChR α1 subunit can be successfully superimposed onto an AChBP monomer, making AChBP a possible template of the ECD for drug design.[8,11] This has been the basis for making a nAChR homology model for drug design – that is until the recent publication of the X-ray crystal structure of the human α4β2 nAChR. Structural information from EM and X-ray studies is immensely useful when combined with the results from functional studies.

Site-directed unnatural amino acid (UAA) mutagenesis and electrophysiology have also been used for interrogating the structure-function relationships of ion channels. Implementation of these two techniques, for example, has helped reveal in nAChR a cluster of aromatic residues that comprise the ligand-binding site and particularly a cation-π interaction between the cationic moiety of the ligand (e.g., ACh) and the electron-rich π-system of the indole moiety of a tryptophan residue.[12]

Although each technique has contributed to a generous breadth of knowledge, they also have their inherent limitations. The EM structure has provided a great topological overview, but the low-resolution nature of EM is insufficient for accurately understanding local molecular interactions. X-ray crystallography provides a high-resolution atomic image of protein structure but is also notoriously difficult to apply to membrane proteins.[13] It also only provides one snapshot of the protein conformation, which is usually in the desensitized state due to the overdosing of the protein with agonists during the crystallization process. Electrophysiology can primarily distinguish between the open state and the closed state but lacks in identifying structural movements that may occur during transitions of dark states, i.e. non-conducting states. Techniques that can distinguish the open and the numerous closed states ion channels can adopt are needed. Fluorescence-based techniques have the potential to address this. Despite this, electrophysiology is a powerful tool for investigating ion channel function and the role of various drugs such as allosteric modulation.

Unnatural Amino Acid Mutagenesis

Since being first reported in 1989, unnatural amino acid (UAA) mutagenesis has proven to be a powerful tool for engineering novel functionalities into proteins by expanding the genetic code to more than the twenty amino acids that nature provides.[14] Two main approaches have been developed: one utilizes an evolved tRNA synthetase with specificity for a cognate amino acid for acylation onto tRNA[15], and the other utilizes chemical acylation of the tRNA without a tRNA synthetase[16]. In the Dougherty lab, the chemical acylation approach is implemented. The chemical acylation strategy has enriched us with vast diversity of unique protein functionality, as almost any UAA can be chemically synthesized. The only broad limitation is that the incorporation of the UAA is dependent on the tolerance by the ribosome. Experimentally, the UAA is synthesized and then chemically coupled to dinucleotide dCA and lastly to the tRNA. The aminoacyl-tRNA along with mRNA with a stop or "nonsense" codon introduced at the desired position is physically injected into *Xenopus laevis* oocytes for protein expression. This *in vivo* nonsense suppression methodology to incorporate UAAs have been utilized and optimized in the Dougherty/Lester labs. Then, electrophysiology and/or bio-imaging experiments are performed on the oocytes.[17] (Figure 1.3)

Xenopus Laevis Oocytes Expression System

Xenopus laevis oocytes have been established as an excellent cellular host for the heterologous expression of mammalian neuroreceptors and ion channels. Since multimeric ion channels typically require sophisticated cellular protein processing and transport, a vertebrate cell like the oocyte is a suitable system. Upon mRNA injection, the proteins are folded, modified, assembled into pentamers, and trafficked to the plasma membrane. The large size (~1 mm in diameter for Stage V and IV) also make handling the cells easier for mRNA or DNA injection and voltage clamp electrophysiology. Although *Xenopus* oocytes is equipped with an array of endogenous ion channels, the signal from heterologous receptors can still be clearly distinguished from the endogenous ones. Typically, the currents produced by these endogenous ion channels are very small compared to that of heterologous ones. These cells have also been

optimized for UAA mutagenesis of several ion channels in our lab, thereby further establishing *Xenopus* oocytes as a good expression system.[17-19]

Electrophysiology

The two-electrode voltage clamp (TEVC) is a conventional electrophysiological technique used to study the properties of electrogenic membrane proteins in large cells, such as *Xenopus* oocytes. TEVC artificially controls the membrane potential (V_m) using two intracellular electrodes – a voltage electrode as a V_m sensor and a current electrode for current injection to adjust V_m. This allows the membrane potential to be set at desired values and the membrane current to be recorded for analysis of ion channel activity. To study how chemical factors (e.g. neurotransmitters, hormones, intracellular messengers, or exogenous drugs) may modulate LGICs such as the nicotinic acetylcholine receptor (nAChR), the electrical conductance of LGICs is measured in response to the addition of chemical stimulants, and EC_{50} experiments for agonists or IC_{50} for inhibitors can be performed. The injected current, which is used to adjust V_m to a constant holding potential, is recorded as the membrane current.[14]

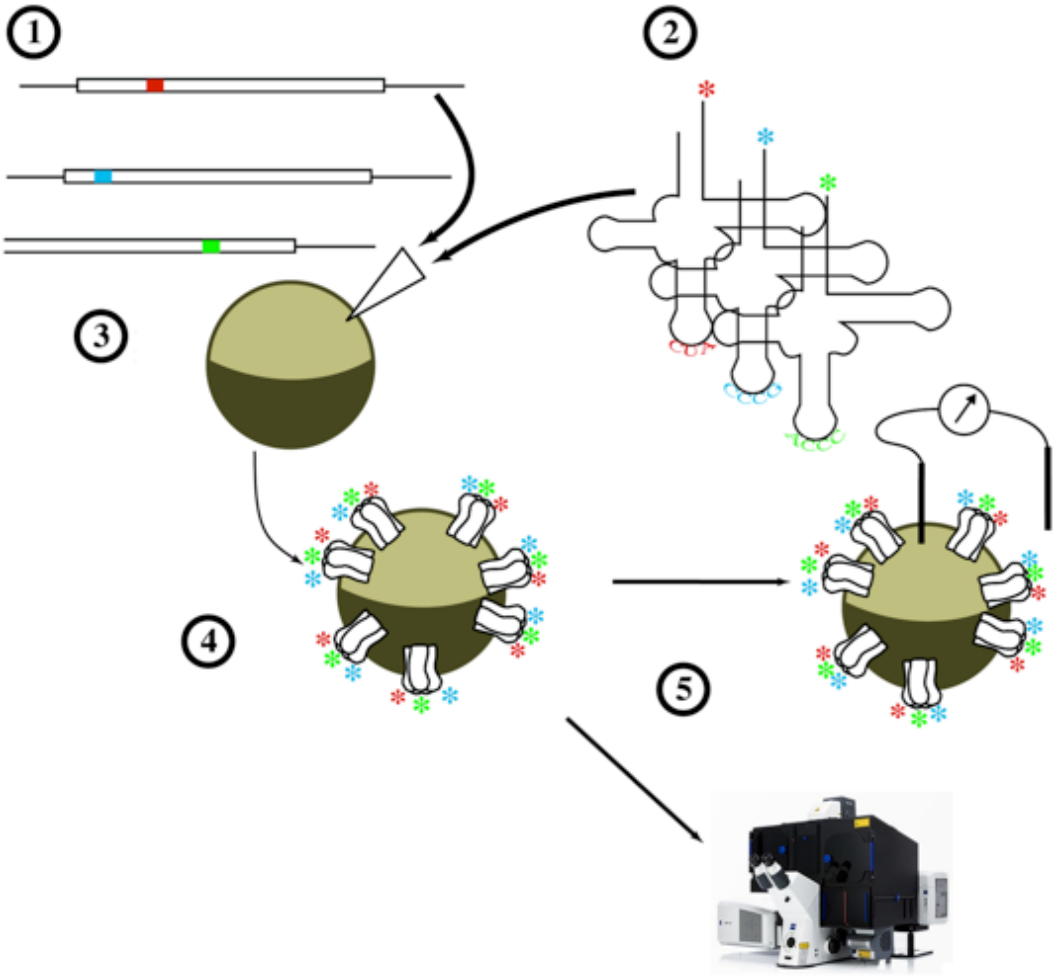

Figure 1.3. General procedure of experiments. For experiments performed in Chapter 2 and 3 of this study: 1) Suppression mRNA construction, 2) chemical acylation of tRNA with UAA, 3) injection of mRNA and tRNA, 4) protein expression, and 5) electrophysiology and/or bio-imaging. In Chapter 5 and 6, only mRNA is injected and studied using electrophysiology.

Summary of Dissertation Work

Part one of this dissertation, namely Chapter 2 and 3, details the development of a novel fluorescence-based biophysical tool to probe these structural changes that underlie the function of LGICs, by employing unnatural amino acids, fluorescence, microscopy, and electrophysiology. Chapter 4 describes attempts to use many of the learnt lessons from Chapter 2 to develop a fluorescence assay to study protein stoichiometry, which can also be extended to studying protein-protein interactions, cellular signaling, protein trafficking, and the like. Part two, namely Chapter 5 and 6, focuses on investigating the role of menthol as an allosteric modulator to the α4β2 nicotinic receptor, a protein that plays a key role in smoking addiction.

Chapter 2 describes the development of a bio-orthogonal labeling method for the incorporation of a "turn-on" fluorophore in the mouse muscle nAChR (α1β1γδ) receptor and imaging with single-molecule TIRF microscopy to optimize and understand fluorescently labeled nAChRs in live oocytes. The novel design of the chemical synthesis of the turn-on fluorescent UAA is also described.

Chapter 3 describes the efforts in measuring the lifetime of the turn-on fluorophore incorporated in the α1β1γδ nAChR towards building a FRET (Förster resonance energy transfer) assay based on fluorescence lifetime imaging microscopy (FLIM). Progress was hampered by uncertain and low fluorescence signals.

Chapter 4 describes efforts in applying the FLIM-FRET approach towards studying the $5HT_3$ receptor stoichiometry using fluorescent protein and expression in mammalian COS-7 cells. Progress was hampered by the ability to distinguish plasma membrane receptors from receptors in the endoplasmic reticulum.

Chapter 5 describes studies investigating the role of menthol stereochemistry in α4β2 receptor inactivation and stoichiometry. We find that the two main stereoisomers of menthol do not differ in acute inhibition levels for both stoichiometries of the α4β2 nAChR.

Chapter 6 describes efforts towards identifying the menthol binding sites on the α4β2 nAChR using a combination of computational docking and experimental mutagenesis screening. The results of the sites tested thus far did not seem to suggest a menthol binding site has been identified.

Chapter 2

A LOW-BACKGROUND FLUORESCENT LABELING STRATEGY FOR THE SINGLE-MOLECULE IMAGING OF NACHRS

2.1 Abstract

Fluorescent labeling of nAChRs, and more broadly LGICs, is valuable in probing conformational changes upon ligand binding. Incorporation of fluorogenic unnatural amino acids (UAAs) via nonsense suppression has enabled the site-selective labeling of these receptors. The *in vivo* imaging of these fluorescent-labeled proteins has previously yielded high background fluorescence, hampering progress in conducting further studies. We developed a strategy for the incorporation of turn-on small-molecule fluorophores into the mouse muscle nAChR via UAA mutagenesis and the tetrazine ligation reaction, imaging with total internal reflection fluorescence (TIRF) microscopy. This set of turn-on fluorophores yielded very small non-specific background fluorescence *in vivo*. This fluorophore labeling strategy will expand the number sites that can be probed and allow the use of a greater variety of dyes. A second fluorophore can be introduced using fluorogenic UAAs or by utilizing the chemoselectivities of different bioorthogonal reactions to enable intermolecular Förster resonance energy transfer (FRET) studies.

2.2 Introduction

Fluorescent labeling of proteins is valuable for probing biophysical properties of the protein and for understanding its role in biological processes. In many cases, fluorescent proteins (FPs) are incorporated through fusion with the protein of interest via genetic encoding. FPs have been used to identify protein-protein interactions and identify the stoichiometry of the subunits for ion channels.[14, 20] However, FPs can interfere with protein function, folding, and stability, and they are limited to incorporation on the protein surface due to their typically large size (~27 kDa). On the other hand, chemical fluorophores would be more desirable for studying intramolecular interactions in a protein due to their small size. One study incorporated a small-molecule fluorophore into the channel lumen of mouse muscle nAChRs in *Xenopus* ooctyes *via* unnatural amino acid (UAA) mutagenesis and was imaged using single-molecule TIRF microscopy.[21] TIRF was used to reduce the background intracellular fluorescence of oocytes. This study is significant for successfully incorporating a small-molecule fluorophore at a non-cysteine site and detecting single-molecule receptors in live cells. Unfortunately, further progress with this study was impeded due to high background from fluorescent UAA inside the cell, and prior efforts to alleviate fluorescence background have been unfruitful.[18] The main advantage of incorporating small-molecule UAAs is the ability to probe an expanded the number of sites on the protein with site-selectivity. However, in order to fully take advantage of fUAAs, undesired background fluorescence signals must be minimized.

We developed a new labeling strategy for the site-selective incorporation of fUAAs using click chemistry (tetrazine ligation reaction) with turn-on fluorescence. We designed a novel synthesis of a turn-on Bodipy-UAA, showed successful turn-on fluorescent labeling of the mouse muscle nAChR in live *Xenopus laevis* oocytes, and dramatically reduced undesired background fluorescence. We used single-molecule TIRF microscopy to image fluorescent nAChRs *in vivo*.

The Turn-on Fluorescent Labeling Strategy

The tetrazine ligation reaction is implemented in the fluorescent labeling strategy. Bicyclononyne (BCN) is incorporated as a lysine-derived UAA (Figure 2.1) into nAChRs by the

chemical acylation approach. After mutant nAChRs are expressed on the plasma membrane, a small-molecule fluorophore conjugated to tetrazine is supplemented. The site of BCN incorporation by this strategy is chosen so as to the have adequate accessibility of the fluorophore.

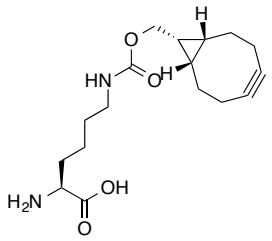

Figure 2.1. BCN-lysine UAA.

Bio-orthogonal Chemistry – The Tetrazine Ligation Reaction

The tetrazine ligation reaction used in these studies is a strain-promoted azide-alkyne cycloaddition (SPAAC), which has several advantages for bio-orthogonal labeling. Not only does this reaction not require a metal catalyst, it also proceeds quickly and efficiently at ambient temperatures and in simple, biologically relevant solvents like buffered-water. In the tetrazine ligation reaction, a bicyclononyne and an *s*-tetrazine follow an inverse-demand Diels Alder reaction and then a retro-Diels Alder reaction to eliminate nitrogen gas (Figure 2.2). The advantage of using tetrazine as a reactive group is its fast reaction with BCN (~ 0.14 M^{-1} s^{-1} [22]) and also its ability to induce "turn-on" fluorescence when conjugated to a small-molecule fluorophore.[23]

Turn-on Fluorescence with Tetrazine-conjugation of Small-molecule Fluorophores

Tetrazine plays a dual role as both a quencher and bioorthogonal reactant, making activatable "turn-on" tetrazine-linked fluorophores an attractive feature for bio-imaging. Upon tetrazine reacting with a dienophile (e.g., BCN), the fluorophore conjugated to the tetrazine may have emission increased by 20-fold or even up to 11,000-fold[24] (Figure 2.2). This fluorescence increase is particularly important for dyes that exhibit non-specific binding. The mechanism for fluorescence quenching is suspected to be *via* through-bond energy transfer (TBET), where energy is transferred via a contiguous scaffold of π bonds.[24]

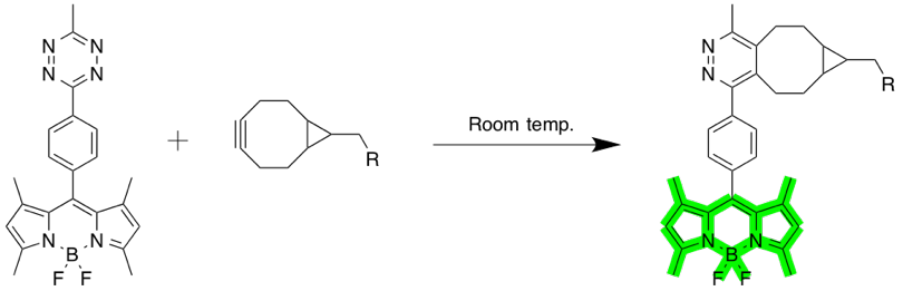

Figure 2.2. Turn-on fluorescence of Bodipy. The reaction of a *p*-methyl-tetrazine-Bodipy with a BCN results in the unquenching of fluorescence emission of Bodipy.

Some tetrazine-conjugated dyes that have been used in these studies are commercially available (Cy3, Cy5, 5-FAM, and Atto 488), while another requires in-house chemical synthesis (Bodipy). Coumarin is another fluorophore candidate that is not commercially available and the tetrazine-conjugated version has not been synthesized in-house yet. The tradeoffs for each dye take into consideration commercial availability and the turn-on ratio, which is an indicator of the undesired fluorescence signal level. On one hand, tetrazine-conjugated BODIPY (Tz-Bodipy)[25] and Tz-Coumarin[26] exhibit high turn-on abilities but also require in-house chemical synthesis, which is time-consuming and low yielding; coumarin and BODIPY have also been used as pairs in ensemble FRET measurements.[27-28] On the other hand, Tz-Cy3 and Tz-Cy5 are commercially available, but exhibit extremely low to negligible turn-on fluorescence; Cy3 and Cy5 are known to be highly efficient FRET pairs for single-molecule FRET.[29-30]

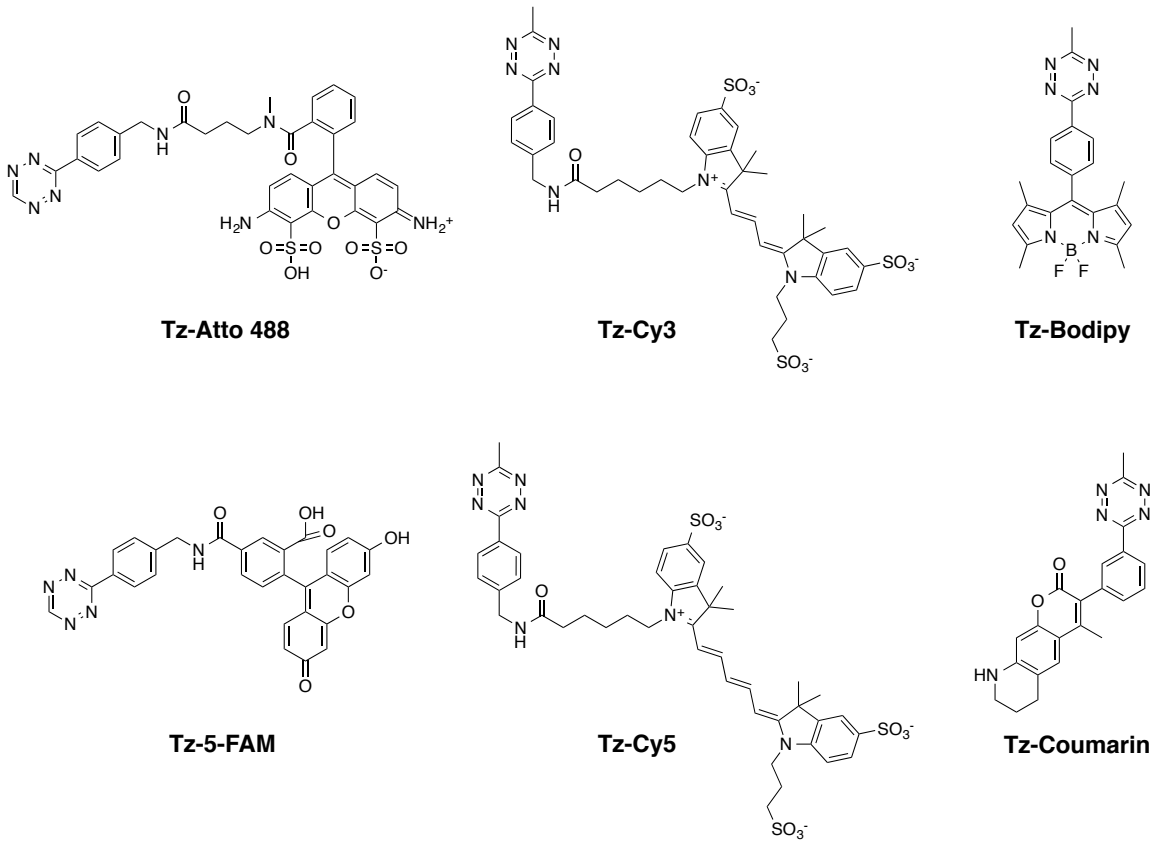

Figure 2.3. Chemical structures of tetrazine-conjugated dyes.

2.3 Results and Discussion

Synthesis of *para*-methyl-tetrazine-Bodipy

The synthesis of *para*-methyl-tetrazine-Bodipy has been reported in the literature (Scheme 1).[25] However, the reported synthetic route requires a final purification step between a methylated tetrazine compound and an unmethylated one. To avoid this purification step, an alternative route was attempted that would directly yield a methyl-tetrazine group conjugated to Bodipy by adapting from various literature sources (Scheme 2). To start, the aldehyde group on 4-cyanobenzylaldehyde (**1**) is reduced to an alcohol, yielding a cyanobenzylalcohol (**2**). Next, the nitrile group is converted to a methyl-1,2,4,5-tetrazine (**3**). Tetrazine-benzylalcohol undergoes an oxidation reaction to yield a tetrazine-benzylaldehyde (**4**). Finally, the Bodipy is formed (**5**).

Although the formation of the Bodipy yielded a multitude of side products, careful purification between *p*-methyl-tetrazine-Bodipy and tetrazine-Bodipy was not necessary. Extremely small fractions were obtained during a silica flash column chromatography step. The molecular weight of each fraction was analyzed using liquid-chromatography mass-spectrometry (LC/MS), and the fraction containing the compound with the correct mass-to-charge ratio was further verified using NMR. Upon reacting this compound with (1R,8S,9S)-Bicyclo[6.1.0]non-4-yn-9-ylmethanol (BCN-OH), fluorescence emission turn-on was observed under a long-wavelength UV lamp. Our synthetic route directly produced *p*-methyl-tetrazine-Bodipy at a higher overall yield (4.9%) than the original published synthesis (2.4%, assuming ~30% yield as well for synthesis of *p*-cyanobenzyl-Bodipy[25]).

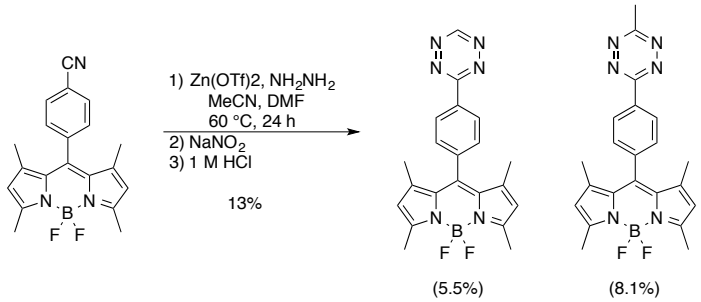

Scheme 1. Published synthesis of a mixture, including *p*-methyl-tetrazine-Bodipy.[25]

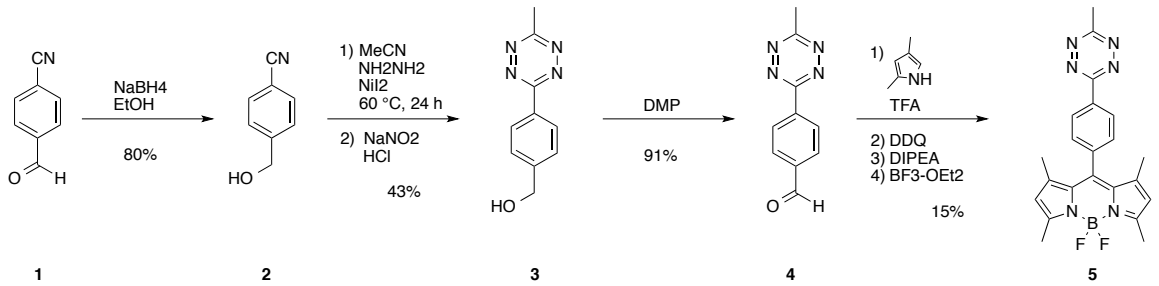

Scheme 2. Our synthesis for *p*-methyl-tetrazine-Bodipy.

Synthesis of α-NVOC-Lysine(BCN)-THG73 tRNA

The synthesis of (1R,8S,9S)-Bicyclo[6.1.0]non-4-yn-9-yl (BCN) UAA for acylation onto tRNA has never been achieved. The synthetic route first attempted followed standard protocols for the preparation of α-NVOC-amino acid-dCA (Scheme 3). This involves: 1) NVOC-protection of amine group, 2) cyanomethylation of carboxylic acid, 3) coupling to dCA, and 4) ligation to 74mer tRNA. The production of α-NVOC-L-Lysine(BCN)-O-dCA failed at the cyanomethylation step (Scheme 4). The reaction was analyzed with LC/MS, revealing mass traces that corresponded to BCN alone. We suspect that BCN may have hydrolyzed off of α-NVOC-L-Lysine during the reaction.

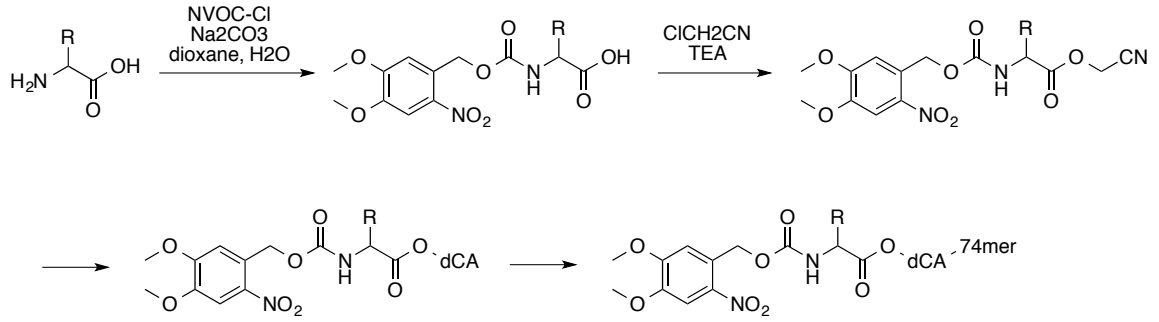

Scheme 3. Standard synthesis for modified UAA-tRNA.

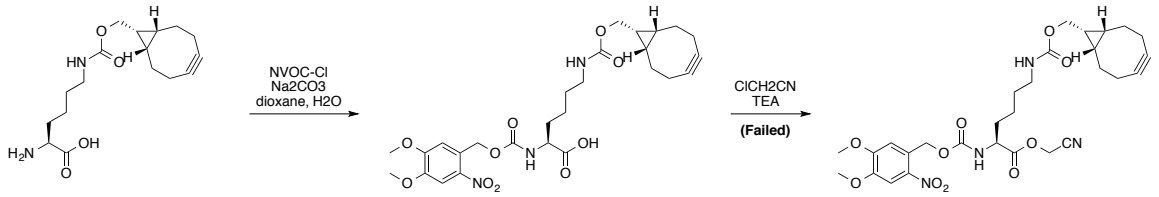

Scheme 4. First attempted synthesis based on standard protocols (failed).

Therefore, a second route, in which the BCN group was attached after cyanomethylation, was attempted (Scheme 5). We started with N-ε-Boc-Lysine for NVOC-

protection followed by cyanomethylation, yielding α-NVOC-N-ε-Boc-Lysine-OMeCN (**8**). Next, the Boc protecting group was removed, followed by the formation of a carbamate upon reaction with BCN-succinimidyl ester (BCN-OSu). dCA coupling and tRNA ligation followed suit, yielding α-NVOC-Lysine(BCN)-O-dCA and α-NVOC-Lysine(BCN)-O-dCA-74mer. The 74mer tRNA from *Tetrahymena thermophila* was used. It recognizes the amber stop codon [11] and has been mutated at the position 73 (THG73) to remove its recognition by the glutamine synthetase. Matrix assisted laser desorption ionization mass spectrometry (MALDI-MS) was used to confirm the production of the modified aminoacyl-tRNA (**13**). Approximately 8 μg in 25 μL of water of α-NVOC-Lysine(BCN)-O-dCA-74mer was produced.

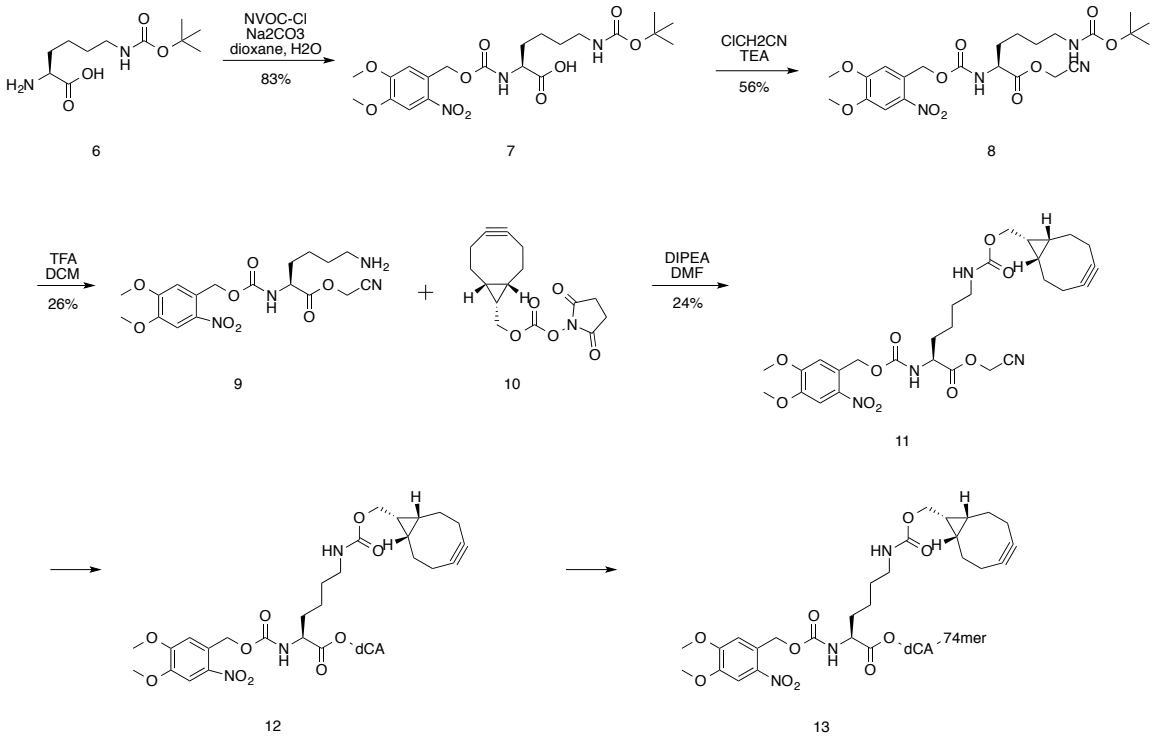

Scheme 5. Second attempted synthesis, yielding α-NVOC-Lysine(BCN)-O-dCA-74mer (success.)

Turn-on Fluorescence

The fluorescence turn-on abilities of the tetrazine-conjugated dyes were tested by reaction with excess BCN-OH in water. Their turn-on ratios were calculated based on the peak intensity of fluorescence emission (Table 2.1). Tz-Bodipy and Tz-Coumarin have the highest turn-on ratios (from published literature). Tz-5-FAM and Tz-Atto 488 have a longer linker

length and lower turn-on ratios. Lastly, Tz-Cy3 and Tz-Cy5 have the longest linker length and lowest turn-on ratios. This trend may suggest that the linker length between the tetrazine-benzyl group and the dye could potentially affect TBET efficiency – or whichever quenching mechanism it may be. If this trend holds up and high quenching ability is necessary, we may be motivated to synthesize in-house particularly Tz-Cy3 and Tz-Cy5 with a shorter linker length for higher turn-on ability, since Cy3 and Cy5 is an established good FRET pair.

Probe	Fluorescence increase in water
Tz – 5-FAM	9-fold
Tz – Atto 488	20-fold
Tz – Cy3	2-fold
Tz – Cy5	4-fold
Tz – Bodipy	900-fold[25]
Tz – Coumarin	11000-fold[26]

Table 2.1. Turn-on fluorescence ratios. Tetrazine-conjugated dyes exhibited increase in fluorescence emission upon reaction with BCN-OH in water for ~ 30 minutes.

Expression and Electrophysiology of Mutant nAChR

Potential detriment to expression of functional nAChR due to UAA mutagenesis was tested using two-voltage clamp electrophysiology. For the initial round of testing, a tryptophan 'unnatural amino acid' (Trp-UAA), in which a tryptophan was chemically acylated onto $THG73_{TAG}$ tRNA, was used, since tryptophan and BCN are both nonpolar and bulky. A $THG73_{TAG}$ 76mer was used as a negative control to gauge the 'read-through' background of functional receptors without the UAA.

Six sites on the δ and β subunits of the mouse muscle-type nAChR were mutated to the UAG amber stop codon. δ and β subunits were chosen since there is only one subunit – compared to two for the α subunit – in nAChR for future FRET studies, in which a 1:1 ratio of each fluorophore is desired. The sites were selected for their similarity in location to α-70, which has previously been shown to be a permissive site[31]. One of the drawbacks of this labeling approach is the permeability of the tetrazine-dye, limiting the accessible sites to mostly residues in the ECD. The expression conditions in the first test round were too high, exceeding the instrument's limit in measurements of currents. In the second round, two sites were tested with

BCN-UAA incorporation with milder expression conditions (single injection with 24 h expression rather than a double injection with 48 h).

The currents of the 76mer control are comparable to that of UAA-incorporated proteins for all sites, except for δ-303, suggesting that the sites are permissive, since they are far from the channel lumen and the ligand-binding site (Table 2.2). The high currents from the 76mer control experiment may be due to the reacylation of the uncharged tRNA. Uncharged suppressor tRNAs may be recharged, or reacylated, with natural amino acids by endogenous synthetases and then delivered to the UAG mutation site, producing functional receptors.[17] These functional 'read-through' nAChRs would contribute to ionic current and cannot be distinguished from UAA-incorporated nAChR by electrophysiology alone. Consequently, TIRF microscopy is necessary to confirm the incorporation of the BCN-UAA in nAChR.

Average I_{max} (μA) – 48 h, double inject				
Probe	Trp-UAA	N	76mer	N
δ-285	-36.1	4	-23.7	4
δ-279	-38.3	1	-21.1	4
δ-303	–		–	
β-276	-82.3	1	-30.2	4
β-270	-34.1	3	-40.1	2
β-294	-47.6	4	-41.1	5
5 ng w/t	-33.5 (N=2)			

Average I_{max} (μA) – 24 h, single inject				
Probe	BCN-UAA	N	76mer	N
δ-285	-8.958	1	-7.866	2
β-294	-18.019	3	-9.489	3
α-70	-27.889	2	-19.861	3

Table 2.2. Average maximum current induced by 1 mM ACh of nAChR with single mutations. N is the number of oocytes.

TIRF Imaging

Non-specific binding

Xenopus oocytes without mRNA and tRNA injection were incubated with the tetrazine and α-Bungarotoxin (αBtx) dyes. αBtx binds to the α1-β1 subunit interface (Figure 2.6). All receptors at the plasma membrane – with or without the UAA – will be labeled by the αBtx dyes. After the usual washing steps, TIRF imaging detected near-zero puncta from tetrazine-dye labeling, suggesting negligible non-specific binding (images not shown). A very sparse amount of puncta from labeling with αBtx dyes was observed, suggesting some non-specific binding (Figure 2.4).

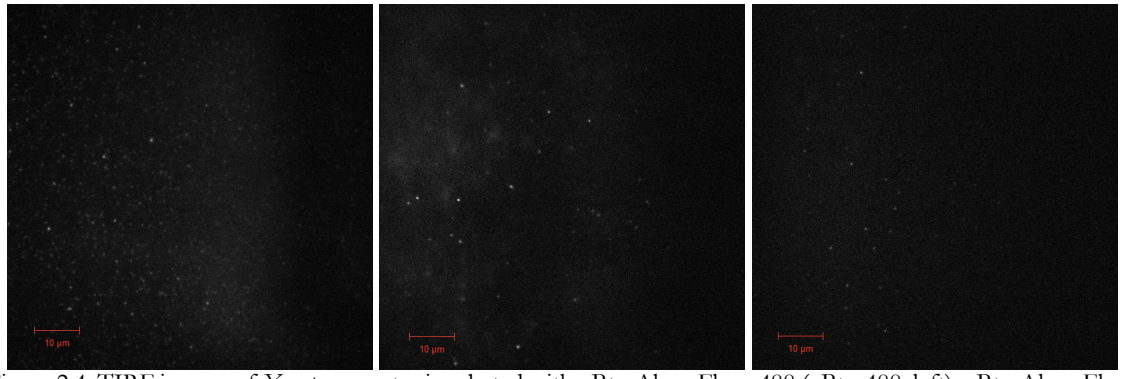

Figure 2.4. TIRF images of *Xenopus* oocytes incubated with αBtx-Alexa Fluor 488 (αBtx-488, left), αBtx-Alexa Fluor 555 (αBtx-555, middle), and αBtx-Alexa Fluor 647 (αBtx-647, right).

Tetrazine-dye labeling at a70 site

After 48 h of expression and two injections of mRNA and L-Lysine(BCN)-THG73$_{TAG}$ (one initial injection and one at 24 h), sparse fluorescent puncta were observed when Tz-Bodipy, Tz-Cy3 or Tz-Cy5 were independently added (Figure 2.5). Puncta were not detectable with a single injection of mRNA and tRNA with 24 h of expression however. Expression at 24 h with a single injection is insufficient for UAA-incoporated nAChR expression.

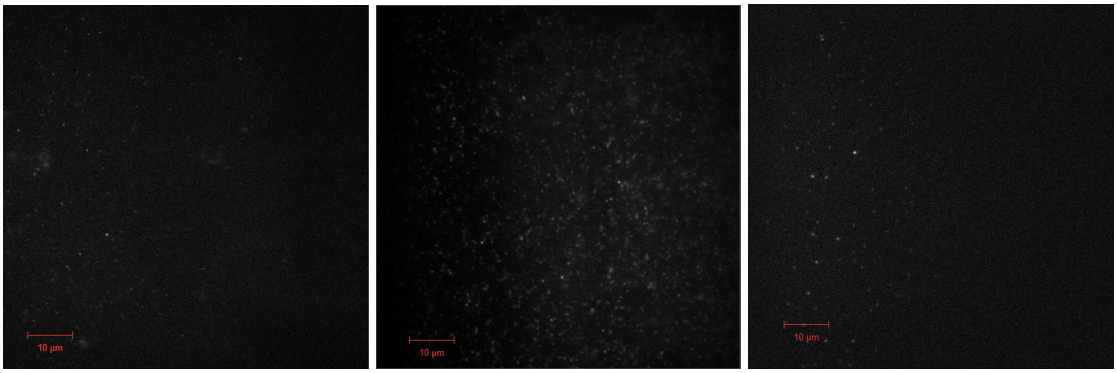

Figure 2.5. TIRF image of α-70 nAChR expressed in *Xenopus* oocytes incubated with Tz-Bodipy (left), Tz-Cy3 (middle), and Tz-Cy5 (right).

Tetrazine-dye and aBtx-dye co-labeling at α-70 site:

Using the 48 h, double-injection conditions for expression, oocytes were co-labeled with a tetrazine-dye and a αBtx-dye of a different spectral profile. αBtx-binding does not block the α-70 site (Figure 2.6). The optical setup of the TIRF microscope has multiple laser lines and two sensitive cameras, allowing concurrent imaging of both dyes. Since αBtx binds to nAChR, we expect puncta for all nAChRs even those without the BCN-UAA. Sparse puncta were again observed in the channel corresponding to the tetrazine dye (right frame in Figure 2.7a and 2.7c and left frame in Figure 2.7b). However, in the channel corresponding to αBtx-dye, the images were saturated with puncta (left frame in Figure 2.7a and 2.7c and right frame in Figure 2.7b). This indicates that there was a saturation of 'read-through' receptors, which is in line with the electrophysiology results from the 76mer control. Because of the oversaturation of read-through nAChR and the limited mutant nAChR, photobleaching analysis could not be reliably performed.

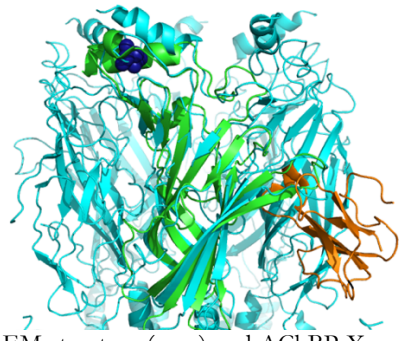

Figure 2.6. ECD of *Torpedo* nAChR EM structure (cyan) and AChBP X-ray structure (green) with αBtx (orange). Residue at α-70 site highlighted as dark blue spheres. Figure generated in Pymol with PDB 2bg9 (cyan) and 2qc1 (green and orange).

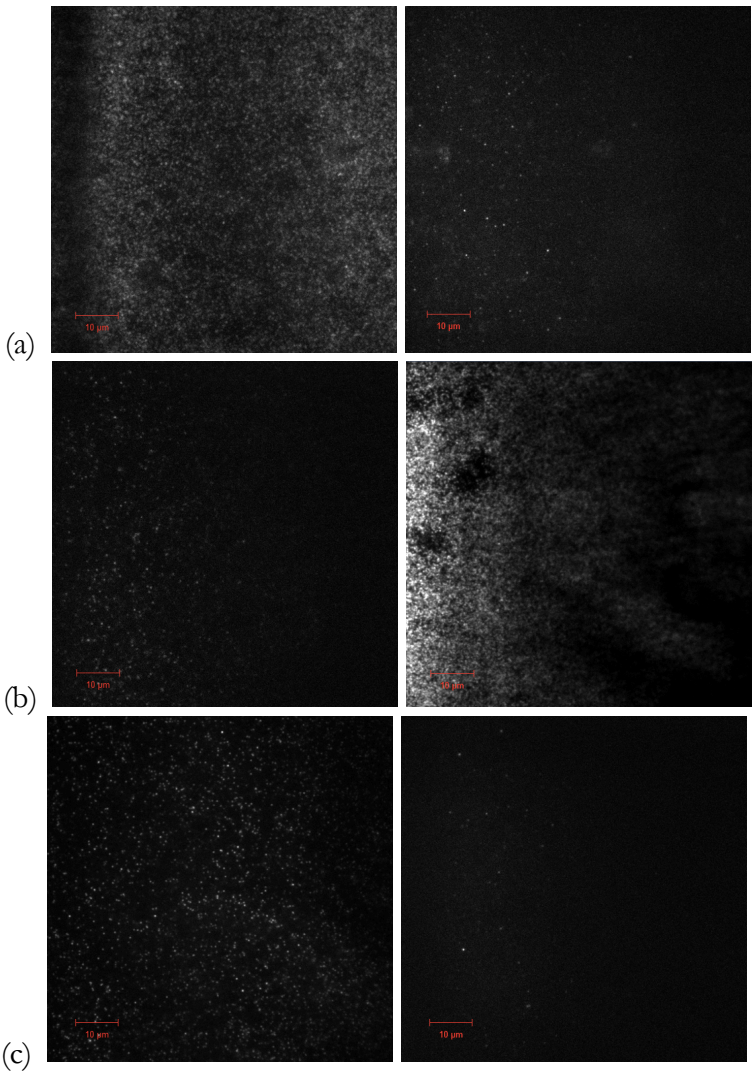

Figure 2.7. TIRF images of α-70 nAChR expressed in *Xenopus* oocytes incubated with (a) Tz-Cy5 and αBtx-647 (488 nm laser (right) and 642 nm laser (left)), (b) Tz-Cy3 and αBtx-488 (488 nm laser (right) and 561 nm laser (left)), and (c) Tz-Cy5 + αBtx-488 (488 nm laser (right) and 642 nm laser (left)).

In summary, with TIRF microscopy, we successfully: 1) detected sparse puncta from fluorescently labeled nAChR at the membrane, 2) determined the expression conditions needed for adequate expression of UAA-incorporated nAChR, 3) observed negligible non-specific binding from tetrazine-dyes and little from αBtx-dyes, and 4) supported the electrophysiology studies that a significant concentration of functional nAChR are without the bio-orthogonal handle BCN-UAA. Photobleaching and N&B analysis cannot reliably be used to study receptor clustering and another approach is needed.

Localization of Intracellular Autofluorescence Revealed with 3D Stack Construction

Xenopus oocytes are known to have high intracellular fluorescence.[21] Autofluorescence was studied by constructing a 3D z-stack image of oocytes expressing wild-type nAChR with and without labeling of αBtx-Alex Fluor 488 (αBtx-488). Since αBtx-488 is membrane-impermeable and binds only nAChRs expressed at the membrane surface, αBtx-488-labeling gives a point of reference to the location of autofluorescence.

The molecules near the plasma membrane of the oocyte were studied using a 488 nm excitation laser. 3D z-stack images of uninjected and αBtx-488 labeled oocytes were constructed, where each frame or 'layer' was ~ 2 microns thick, totaling ~ 86 microns. Further than 86 microns, negligible fluorescence was observed and therefore not recorded. The 3D image of αBtx-488 labeled oocytes was indistinguishable from that of uninjected oocytes (Figure 2.8). That is, there is no clear delineation between the fluorescence at plasma membrane and autofluorescence near the membrane, further suggesting that autofluorescence is closely localized to the plasma membrane. This confirms our observations from TIRF studies; autofluorescence is observed when the TIRF penetration depth is increased (Figure 2.9). Although autofluorescence is indistinguishable from αBtx-488 in the 3D image, this does not preclude the ability of TIRF to drastically reduce autofluorescence from the images. The penetration depth of the evanescent wave (~ 0.1 microns) is much smaller than the thickness of each layer from the 3D z-stack imaging (2 microns). Unfortunately, the optical setup is unable to image layers in the nanometer range.

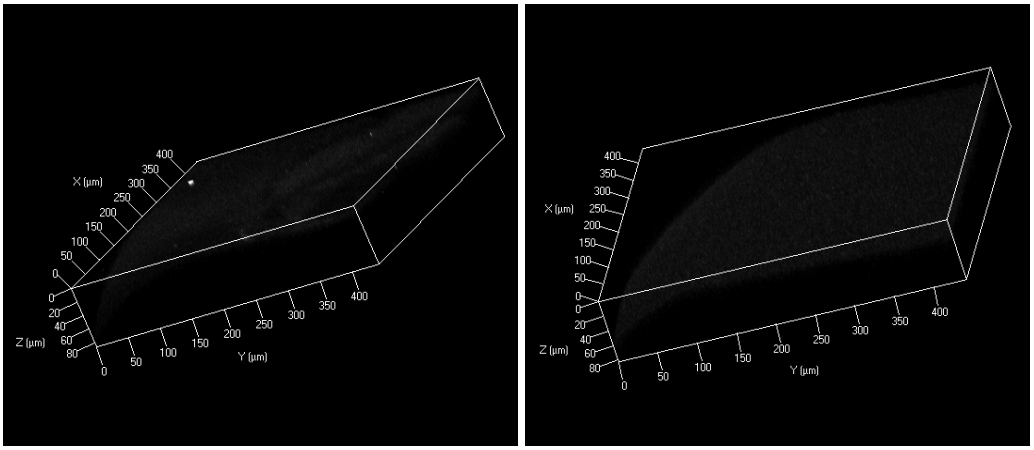

Figure 2.8. 3D z-stack image of wild-type nAChR expression *Xenopus* oocyte incubated with αBtx-488 (right) and uninjected oocyte (left).

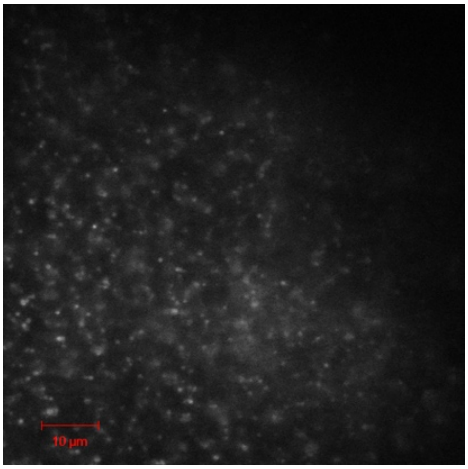

Figure 2.9. TIRF image of wild type nAChR expressing *Xenopus* oocyte.

2.4 Conclusions

Background fluorescence has been an inherent problem for *in vivo* imaging with fluorescent labeling of ion channels via unnatural amino acid mutagenesis and nonsense suppression. We have successfully developed a labeling strategy by incorporating turn-on fluorophores via nonsense suppression that leads to extremely low background fluorescence that previous strategies have not been able to achieve.

Future efforts remain in the development of two-color labeling if this method were to be expanded into FRET studies. The strategies for incorporating the second fluorophore include either incorporating a fluorogenic UAA as the second fluorophore or utilizing the chemoselectivity of different bioorthogonal reactions. In the first strategy, a fluorogenic UAA and BCN-UAA would be concurrently introduced *via* different suppression methods, choosing from frameshift or nonsense suppression. An advantage of incorporating fluorogenic UAA is that non-ECD sites can be reached. In a previous study, a fluorescent lysine-Bodipy was incorporated into the channel lumen of the mouse muscle nAChR.[21] One of the potential disadvantages is a high background signal from intracellular fluorogenic UAAs. In a different strategy, two different UAAs with selective specificity for modified fluorophores can be incorporated *via* different suppression methods. Similar one-pot dual-labeling methods have previously been done (Figure 2.10 and 2.11).[32-33] Bioorthogonal pairs that do not cross-react, such as BCN with one tetrazine derivative and norbornene with a different tetrazine derivative, can be used.

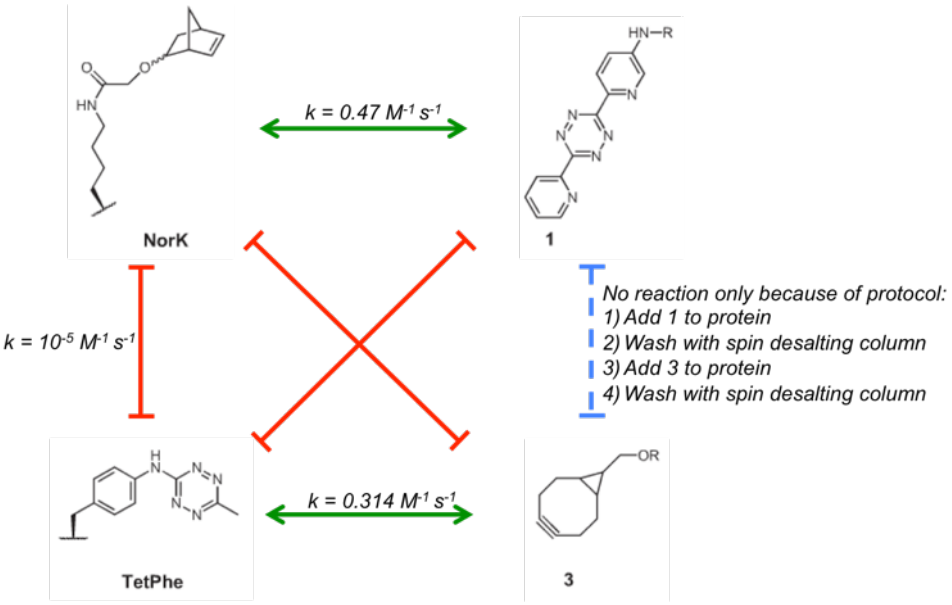

Figure 2.10. Selective reactivities and reaction rate amongst norbornene-lysine (NorK), tetrazine-phenylalanine (TetPhe), and two tetrazine derivatives (1 and 3). Red lines indicate no cross-reaction or extremely slow reaction rates. Figure generated based on the results of Kaihang, et al.[33]

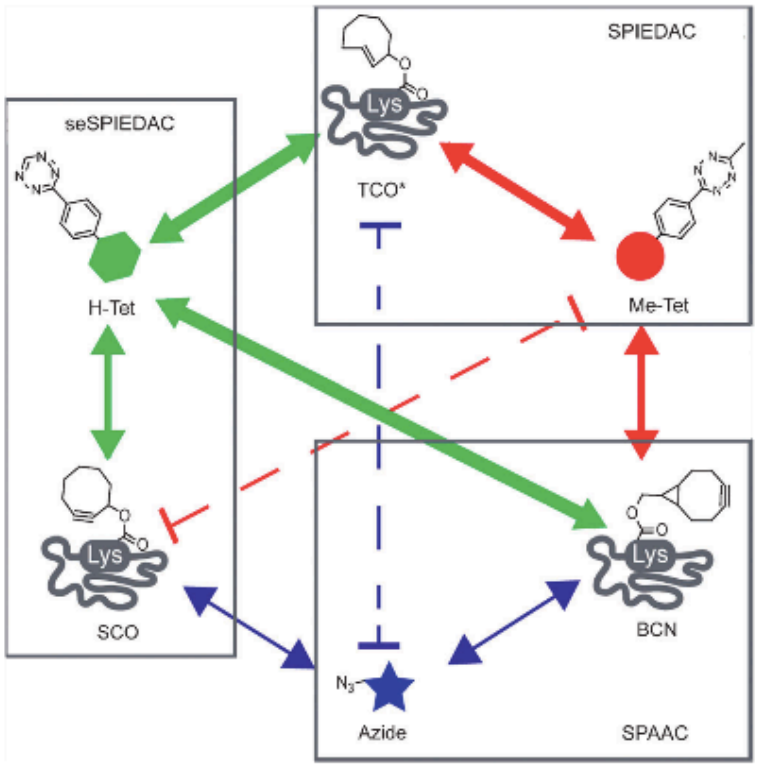

Figure 2.11. Reactivities of TCO, SCO, and BCN with azide (blue), H-tet (green), and Me-tet [34]. Reaction rates are correlated to the thickness of the arrow. Dashed lines highlight reactants that do not cross-react. Figure taken from Nikić, et al.[32]

2.5 Experimental Methods

2.5.1 Organic Synthesis

General Information. All reactions were performed in a flame-dried round-bottom flask and in freshly dried solvents unless otherwise specified. Reactions were monitored with thin-layer chromatography using silica gel (EMD/Merck silica gel 60 F254 pre-coated plates, 0.25 mm) and LC/MS (Agilent 6140 Quadropole). Silica flash column chromatography was performed using silica gel 60 (EMD).

Materials. Reagents were obtained and used as received from Sigma Aldrich. Dry solvents were freshly distilled from CaH_2 prior to use. Deuterated chloroform solvent for NMR was purchased from Cambridge Isotope Laboratories.

Instrumentation. Proton NMR was recorded on a Varian Mercury-300 (300 MHz) NMR spectrometer.

Synthesis of *p*-methyl-tetrazine-BODIPY

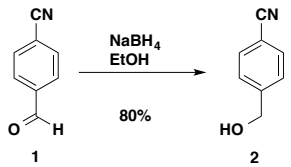

(2). Sodium borohydride (79 mg, 2.1 mmol) was added to a stirred solution of 4-cyanobenzylaldehyde (compound **1**, 250 mg, 1.9 mmol) in absolute EtOH (20 ml). The reaction stirred at room temperature for 5 hours and was then concentrated *in vacuo* using a rotary evaporator. The residue was dissolved in DCM (100 ml). The organic layer was extracted three times with distilled water (3 x 100 ml). The combined organic extract was dried over Na_2SO_4 and concentrated *in vacuo*, yielding the respective 4-cyanobenzylalcohol (compound **2**, 202.8 mg, 1.53 mmol, 80%). Compound **2** was verified by ^{1}H NMR. This reaction was based on Wiles, et al.[35] ^{1}H NMR (500 MHz, Chloroform-*d*) δ: 7.67 (d, J = 7.6 Hz, 1H), 7.49 (d, J = 32.8 Hz, 1H), 4.80 (s, 1H).

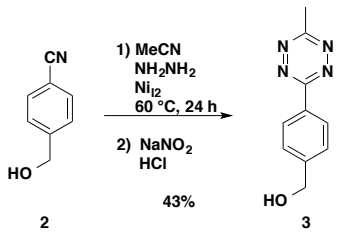

2 3

(3). To compound **2** in a microwave reaction tube under a stream of argon was added 5% NiI_2 catalyst (58.7 mg, 0.188 mmol), MeCN (0.196 ml, 3.75 mmol) and NH_2NH_2 (0.589 ml, 18.7 mmol). The vessel was sealed and allowed to stir at 60 °C for 24 hours. It was then allowed to cool and the septum was removed. To the reaction mixture, $NaNO_2$ (518 mg, 7.51 mmol) in 20 ml of water was added, followed by a slow addition of 1 M HCl until gas evolution ceased and pH = 3. The aqueous phase was extracted three times with EtOAc (200 ml), dried over Na_2SO_4, and concentrated *in vacuo* using a rotary evaporator. The crude mixture was purified using silica flash column chromatography (EtOAc:hexanes, 1:1) to give compound **3** (32 mg, 0.17 mmol, 43%). Compound **3** was verified by ^{1}H NMR. This reaction was based on Yang, et al.[36] ^{1}H NMR (500 MHz, Chloroform-*d*) δ: 8.59 (s, 2H), 7.60 (s, 2H), 4.84 (s, 2H), 3.10 (s, 2H).

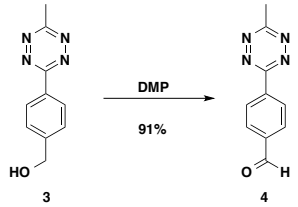

3 4

(4). To a stirring solution of compound **3** (94 mg, 0.46 mmol) in dry DCM (21 ml) under a stream of argon at room temperature, Dess-Martin periodinane (DMP, 33 mg, 0.51 mmol) was added and allowed to stir for 3.5 hours. The reaction mixture, an orange slurry, was treated with saturated aqueous $NaHCO_3$ (12.5 ml) and saturated aqueous $Na_2S_2O_3$ (12.5 ml), stirring for 15 minutes at room temperature. The aqueous layer was extracted two times with DCM (2 x 50 ml). The combined organic layers were then washed with water and dried over Na_2SO_4 and concentrated *in vacuo* with a rotary evaporator. The crude mixture was purified using silica flash column chromatography (100% EtOAc), yielding a red tetrazine-benzaldehyde, compound **4** (85 mg, 0.43 mmol, 91%). Compound **4** was verified by ^{1}H NMR. This reaction

was based on the Dess-Martin reaction from Soenen, et al.[37] ^{1}H NMR (500 MHz, Chloroform-*d*) δ: 10.17 (s, 1H), 8.80 (s, 2H), 8.12 (s, 2H), 3.15 (s, 3H).

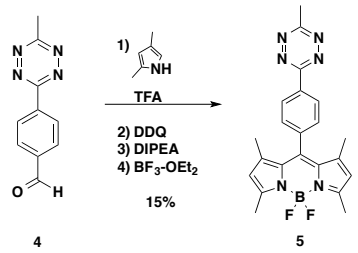

(5). To a stirring solution of compound **4** (45 mg, 0.23 mmol) in dry DCM (6 ml) under a stream of argon at room temperature, 2,4-dimethylpyrrole (50 µl, 0.49 mmol) was added followed by 2 drops of diluted (~1:1) TFA. After 30 minutes, thin layer chromatography (TLC) showed the disappearance of compound **4**. To the reaction mixture, DDQ (51 mg, 0.225 mmol) dissolved in DCM (6 ml) was added, followed by DIPEA (460 µl) and $BF_3 \bullet OEt_2$ (460 µl), stirring for 1 hour. The aqueous layer was extracted three times with DCM (3 x 50 ml). The combined organic extracts were dried over $MgSO_4$ and concentrated *in vacuo* using a rotary evaporator. The crude mixture was purified using silica flash column chromatography (100% toluene), yielding compound **5** (13.7 mg, 0.0327 mmol, 15%). Compound **5** was verified by ^{1}H NMR and LCMS. This reaction was based on Carlson, et al.[25] ^{1}H NMR (300 MHz, Methylene Chloride-d_2) δ: 8.75 (d, J = 8.4 Hz, 1H), 7.60 (d, J = 8.4 Hz, 1H), 6.06 (d, J = 43.8 Hz, 1H), 3.12 (s, 2H), 2.54 (s, 5H), 1.49 (s, 5H).

Synthesis of α-NVOC-Lysine(BCN)-THG73$_{TAG}$

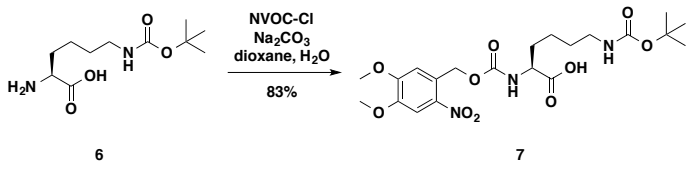

(7). To a stirring solution of Na_2CO_3 dissolved in water (10 ml), N-ε-Boc-Lysine (**6**, 93 mg, 0.38 mmol) dissolved in dioxane (10 ml) and NVOC-Cl (115 mg, 0.41 mmol) dissolved in dioxane (5 ml) was added, stirring for 3-4 hours. Dioxane was removed *in vacuo* using a rotary

evaporator. The reaction mixture was acidified with 0.2 N aqueous HCl to pH ~2. The organic layer was extracted three times with DCM (3 x 10 ml), combined, dried over Na_2SO_4, and concentrated *in vacuo*. The crude mixture was purified using silica flash column chromatography (one column volume of 100% EtOAc followed by one column volume of EtOAc plus 0.5% acetic acid), yielding compound **7** (153 mg, 0.32 mmol, 83%). Compound **7** was verified by ^{1}H NMR and LCMS (NES10B). ^{1}H NMR (500 MHz, Chloroform-*d*) δ: 7.72 (s, 1H), 7.02 (s, 1H), 5.79-5.68 (m, 1H), 5.61 (d, *J* = 15.5 Hz, 1H), 5.45 (s, 1H), 4.64 (s, 1H), 4.39 (s, 1H), 3.97 (s, 6H), 3.14 (s, 2H), 1.46 (s, 9H).

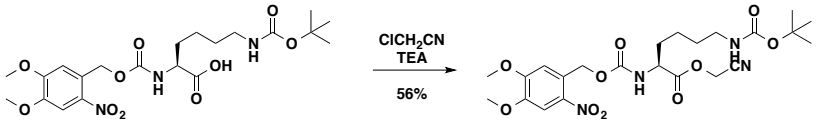

7 8

(8). Compound **7** (153 mg, 0.32 mmol) was dissolved in $ClCH_2CN$ (1.5 ml) to which distilled dry TEA (216 µl, 1.58 mmol) was added and reacted under a stream of argon at room temperature for 24 hours. Excess TEA was removed *in vacuo*. The reaction mixture was purified using silica flash column chromatography (25% EtOAc, 75% DCM), yielding compound **8** (92 mg, 0.173 mmol, 56%). Compound **8** was verified by ^{1}H NMR and LCMS (PES10B, m/z = 547, corresponding to compound 8 plus sodium ion, 524 + 23). ^{1}H NMR (500 MHz, Chloroform-*d*) δ: 7.73 (s, 1H), 7.05 (s, 1H), 5.65 (d, *J* = 15.2 Hz, 1H), 5.44 (d, *J* = 15.3 Hz, 1H), 4.85 (d, *J* = 15.7 Hz, 1H), 4.71 (d, *J* = 15.6 Hz, 1H), 3.99 (d, *J* = 32.1 Hz, 6H), 3.14 (s, 3H), 1.44 (s, 12H).

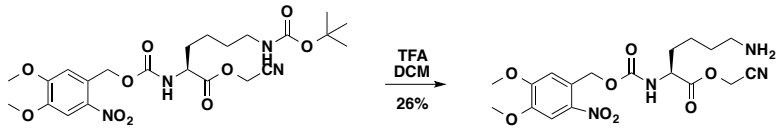

8 9

(9). TFA (500 µl) was added to compound **8** dissolved in dry DCM (500 µl), stirring for 1 hr. Upon addition of TFA, reaction mixture turns green-blue in color. The reaction mixture is concentrated *in vacuo* and purified using silica flash column chromatography (10% MeOH in DCM), yielding compound **9** (9.1 mg, 0.0214 mmol, 26%). Compound **9** was verified by ^{1}H

NMR and LCMS (PES10B). ^{1}H NMR (300 MHz, Methanol-d_4) δ: 7.71 (s, 1H), 7.16 (s, 1H), 5.69-5.26 (m, 3H), 4.91 (s, 1H), 4.41-4.23 (m, 1H), 3.98 (s, 3H), 3.89 (s, 3H), 3.34 (s, 0H), 3.30 (s, 0H), 2.93 (s, 1H), 2.04-1.89 (m, 1H), 1.84-1.66 (m, 1H), 1.61-1.45 (m, 1H), 1.26 (s, 1H).

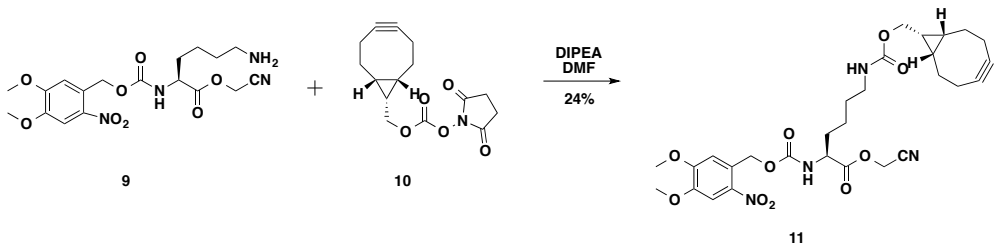

9 10 11

(11). BCN-OSu, compound **10** (Sigma Aldrich, 71.64 mg, 0.246 mmol) was dissolved in DMF (300 µl) and added drop-wise, not via cannula, with a syringe to a stirring solution of compound **9** (241 mg, 0.24 mmol) dissolved in DIPEA (130 µl) and DMF (400 µl), then stirred under a stream of argon for 24 hours. The reaction mixture was diluted with Et_2O (30 ml) and washed with water (3 x 30 ml). The organic layer was combined, dried over Na_2SO_4, and purified using silica flash column chromatography (gradient 50% - 70% of EtOAc in hexanes), yielding compound **11** (36 mg, 0.06 mmol, 24%). Compound **11** was verified by 2D COSY NMR (D-chloroform) and LCMS (PES10B). ^{1}H NMR (300 MHz, Chloroform-*d*) δ: 7.71 (s, 1H), 7.26 (s, 1H), 7.02 (s, 1H), 5.70 (s, 1H), 5.64 (s, 0H), 5.59 (s, 1H), 5.47 (s, 1H), 5.42 (s, 0H), 4.87 (s, 0H), 4.82 (s, 1H), 4.73 (s, 1H), 4.68 (s, 0H), 4.39 (s, 1H), 4.10 (s, 0H), 3.19 (s, 1H), 2.20 (s, 5H), 1.89 (s, 1H), 1.81 (s, 0H), 1.63 (s, 1H), 1.54 (s, 2H), 1.30 (s, 1H), 0.91 (s, 1H).

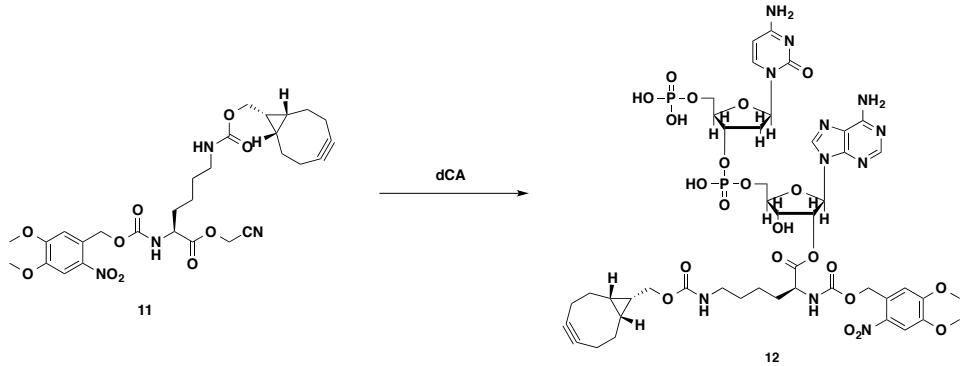

11 12

(12). Compound **11** (15 mg, 0.025 mmol) and dCA (10 mg) were dissolved in dry DMF (1 ml), stirring under a stream of argon for 24 hours. The presence of sample was confirmed using analytical HPLC. The reaction mixture was then purified using preparative HPLC (gradient of 95% to 0% 25 mM NH_4OAc, pH 4.5). Compound **12**, α-NVOC-Lysine(BCN)-O-dCA, was verified by matrix assisted laser desorption ionization mass spectrometry (MALDI MS, 6-aza-2-thiothymine matrix) 1179.3 $[M+H]^+$.

Compound **12**, α-NVOC-Lysine(BCN)-O-dCA, was ligated to $THG73_{TAG}$ (74mer-tRNA) with T4 RNA ligase, yielding α-NVOC-Lysine(BCN)-$THG73_{TAG}$ as previously described (Pantoja ref. 38-40). The product is desalted using a CHROMA SPIN-30 DEPC-H_2O colum (Clonetech). The concentration of the product was measured using the Nanodrop 2000 Spectrophotometer (Thermo Scientific) and verified using matrix assisted laser desorption ionization mass spectrometry (MALDI MS) 24,857.55 $[M+H]^+$. The major peak indicated that α-NVOC-Lysine(BCN)-$THG73_{TAG}$ was the major product.

2.5.2 Turn-on Fluorescence Measurement

Recordings were performed on 2 mL or 3 mL of 2 μM of Tz-Atto 488 and Tz-5-FAM dissolved in water in a 1 cm x 1 cm quartz cuvette using the steady-state fluorometer Fluorolog-3 (Jobin Yvon Inc.). The emission spectra of pre-activated solution (before addition of BCN initiates the fluorogenic reaction) and post-activation were measured. A 300-fold excess of BCN and norbornene was added for a facile comparison of fluorescence turn-on magnitudes. Activation ratios were calculated from the peak emission intensity of the reacted product and the corresponding baseline intensity (pre-activated solution).

2.5.3 Construct Preparation and mRNA Transcription

The α, β, γ, and δ subunits of mouse muscle nAChR are in the pAMV vector. All the TAG constructs including α70, β-276, β-270, β-294, δ-285, δ-279, and δ-303 were prepared by QuikChange mutagenesis on the masked respective subunits in the pAMV vector. The mutation was verified by sequencing (Laragen). The plasmid DNAs were linearized by *Not*I restriction digest. The mRNAs were prepared from linearized DNA, using a T7 mMessage mMachine kit

(Ambion), and purified with the RNeasy Mini kit (Qiagen). Concentration of mRNA was determined by absorption on the Nanodrop 2000 Spectrophotometer (Thermo Scientific).

2.5.4 Oocyte Preparation and Injection

Stage VI oocytes from *Xenopus laeivis* were isolated and incubated at 18 °C in ND96 solution (96 mM NaCl, 2 mM KCl, 1 mM $MgCl_2$, 1.8 mM CaCl2, 5 mM HEPES, 2.5 mM Na pyruvate, 50 μg/mL, 0.6 mM theophylline, pH 7.5). Prior to injection, α-NVOC-L-Lysine(BCN)-$THG73_{TAG}$ was irradiated at 350 nm to cleave the NVOC protecting group, yielding the deprotected L-Lysine(BCN)-$THG73_{TAG}$. L-Lysine(BCN)-$THG73_{TAG}$ was mixed with mRNA at a 1:1 volume mixture while maintained at 4 °C and then loaded for injection. Each oocyte was injected with 20 ng of L-Lysine(BCN)-$THG73_{TAG}$ and 15 ng of mRNA in 75 nl. For α70'TAG mRNA, α, β, γ, and δ were mixed at a ratio of 10:1:1:1. For β'TAG mRNAs, α, β, γ, and δ were mixed at 2:5:1:1. For δ'TAG mRNAs, α, β, γ, and δ were mixed at 2:1:1:5. For wild-type (WT) naChR, α, β, γ, and δ were mixed at a ratio of 2:1:1:1 and 1 ng, 5 ng, or 10 ng per 50 nl were injected per oocyte. Oocytes with TAG mRNAs were injected twice (at 0h and 24 h) with the same concentrations over 48 h of expression for imaging. For electrophysiology experiments, oocytes were only singly injected with a 48 h expression time. Oocytes with WT nAChR were injected once at 0h with a 24h or 48 h expression time.

2.5.5 Small-molecule Fluorescent Dye Labeling

Oocytes were labeled with tetrazine-conjugated dyes (Atto 488, Bodipy, Cy3 and Cy5) and α-bungarotoxin (αBtx) conjugated dyes (Alexa Fluor 488, 555, and 647), dissolved in ND96. They were incubated with 5 nM Tz-dyes and 40 nM αBtx-dyes for 4-8 h, and incubation was terminated by a series of washes before imaging (twice in ND96, then 10 minutes in 5 mg/mL bovine serum albumin solution, followed by two 20-minutes washes in ND96).

2.5.6 Electrophysiology

Currents from oocytes were recorded using a two-electrode voltage clamp on the OpusXpress 6000A (Axon Instruments). Recordings were performed after 24 h or 48 h after

initial injection. Currents were induced with 1 mM acetylcholine (ACh) for a maximum current response. Pipette microelectrodes were filled with 3 M KCl for resistances that ranged between 0.5–2 MΩ and at a holding potential of -60 mV. Calcium-free ND96 solution (96 mM NaCl, 2 mM KCl, 1 mM $MgCl_2$, and 5 mM HEPES, pH 7.5) was continuously circulated for the oocytes.

2.5.7 Microscopy

The microscopes used belong to the Translational Imaging Center located at the University of Southern California (USC). Images were processed using the Zen software (Zeiss) unless indicated otherwise.

TIRF

The imaging chamber with the glass coverslip (NA 1.5) was cleaned via sonication in 6 M NaOH for 20 minutes and then stored in filtered Millipore water. *Xenopus* oocytes were prepared for single-molecule TIRF microscopy by removing the vitelline membrane and transferring to an imaging chamber with the animal pole oriented towards the cover slip. The oocyte was first incubated in hypertonic solution (220 mM sodium aspartate, 10 mM EDTA, 2 mM $MgCl_2$, and 10 mM HEPES, pH 7.4) for ~ 5 minutes, and then the vitelline membrane was removed with forceps under a dissecting microscope. Subsequently, the oocyte was washed with ND96 solution for a few seconds prior to transferring to an imaging chamber filled with ND96 solution. Oocytes were incubated in the imaging chamber for ~ 10 minutes to maximize adherence.

Transmitted bright-field illumination was used to confirm adherence and focus on the plasma membrane. The TIRF microscope for collecting images was the Zeiss ELYRA Superresolution PALM SIM microscope (Carl Zeiss Microscopy). A 63x oil TIRF objective with NA=1.40 (Plan-Apochromat) was used with immersion oil (NA=1.516). Images were captured with an EM-CCD (Andor ixon 89) camera. Solid-state lasers with excitation sources at 488 nm, 561 nm, and 642 nm were used at 30% or 50% power. The power of each laser is 100 mW. Images were acquired with an exposure time of 100 ms and a gain of 200.

3D Z-Stack

A Zeiss LSM-780 inverted confocal microscope (Carl Zeiss Microscopy) was used to obtain 3D z-stack images. *Xenopus* oocytes were prepared in the same fashion as for TIRF imaging. Transmitted bright-field illumination was similarly used to confirm adherence and focus on the plasma membrane. A 32x water immersion objective (NA 0.85) with a 0.99 AU pinhole was used, collecting frames at 2.09 microns thick. An infrared laser with 488 nm excitation was used and two ranges of emission were collected (490-553 nm and 570-695 nm).

Chapter 3

EFFORTS TOWARD DEVELOPING A FLIM-FRET ASSAY FOR NACHRS USING TURN-ON FLUORESCENCE

3.1 Abstract

Interpreting FRET data has typically been labor-intensive and unreliable, especially for intensity-based FRET measurements.[38] Measuring FRET based on lifetime is more robust. This work aims to develop a FLIM-FRET assay using our previously described (Chapter 2) fluorescent labeling strategy: the site-selective incorporation of a turn-on fUAA on nAChRs *in vivo*. We describe our strenuous attempts to measure the lifetime of our turn-on fUAA, Tz-Bodipy, along with other dyes on the mouse muscle nAChR in *Xenopus laevis* oocytes using FLIM. For FRET, a robust strategy will eventually need to be developed for the incorporation of a second fluorophore. Progress was hampered by the inability to verify the source of the fluorescence signal due to the many limitations from combining our turn-on fUAA incorporation strategy with FLIM. Marked variability was observed in the phasor plots for different samples of the same conditions. Progress will continue to be hampered until these variations are understood and accounted for.

3.2 Introduction

Fluorescence-based approaches have been widely employed to characterize the structure and function of proteins, including ion channels. They overcome the limitations associated with EM, X-ray, and electrophysiology, as they can probe dynamical movements of protein interactions and structural rearrangements. Some of the beginning fluorescence studies of ion channels involved a cysteine substitution for fluorescent dye labeling and then recording the dye's emission simultaneously with ionic current to identify the functional state of the channel. However, the results from this method are an indirect representation of the protein's conformational changes.[39-40]

A more direct and informative fluorescence approach to probe protein structural rearrangements is based on FRET (Förster resonance energy transfer). FRET is a physical phenomenon that has been implemented at the ensemble level to study the *Shaker* potassium channel, revealing a conformational change – a twisting motion – associated with gating.[41] Ensemble FRET has been extended to single-molecules, which is advantageous when motions are not correlated between different ion channels in an ensemble.[42] One significant proof-of-principle experiment was the detection of single-pair FRET within a gramicidin A ion channel embedded in a lipid bilayer with simultaneous recording of the ionic currents.[34] However, they reported that fluorescence and electrical measurements did not always correlate, which could have been due to protein aggregation near the lipid membrane edge and limited FRET signal compared to background.[34] This study was challenging for a small protein like the gramicidin A channel (~ 1.9 kDa[43]). Executing such study to LGICs, such as nAChRs, which are much larger and more complex pentameric structures (290 kDA[4]), would be even more challenging.

One of the major pitfalls of the FRET studies performed on ion channels thus far is the measurement of intensity of the FRET signal. The interpretability and reliability of intensity-based FRET measurements is problematic for several reasons including: 1) donor or acceptor spectral bleed-through, 2) distinguishing between increase in FRET efficiency and increase in FRET population (i.e. concentration of FRET species), and 3) high noise signal in intensity

levels.[38] Despite numerous negative control measurements, intensity is still an unreliable measurement of FRET efficiency.

The measurement of lifetime of a fluorophore by fluorescence lifetime imaging microscopy (FLIM) is a more robust engagement of FRET efficiency. The output signal is independent of concentration, and thus alleviates the problem that concentration can falsely increase apparent FRET efficiency. Also, it requires only the measurement of the donor, thus avoiding spectral bleed-through problems.[38] Although FLIM is unquestionably more rigorous in quantifying FRET efficiency than intensity-based approaches, widespread adoption of FLIM is hampered because the instrumentation is expensive to obtain and maintain.[38, 44]

The Phasor Approach to FLIM

In principal various conformational states of LGICs can be elucidated by measuring FRET efficiencies, which is an indicator of distance, using FLIM between many pairs of fluorescently-tagged residues on a receptor. Lifetime data acquired by frequency domain (FD) FLIM can be analyzed using the phasor approach. In the FD method, the excitation laser-source is modulated, and the emission signal is analyzed for changes in phase (phase shift) and amplitude (modulation) relative to the excitation source; the fluorescence lifetime is extracted from the phase shift and modulation.[45] The phasor approach can reveal fluorescence lifetime data – and FRET efficiency – for each pixel in the image, and thus provide a statistically significant analysis on an ensemble at the single-molecule level.

In the phasor approach, data at each pixel can be decomposed into simple phasor coordinates (g, s) on the plot. Lifetime data are treated like phase vectors, or *phasors*. Data measured in FD – and time domain (TD) – can be decomposed into *g* and *s* coordinates in the phasor plot (Equation 3.1 and 3.2). Pixels that contain two components (i.e., two fluorophores with different lifetimes) can be resolved into their fractional contributions (Equations 3.3 and 3.4). Since the phasors are treated like vectors, the multi-exponential component is the linear combination of the single components. The ratio of the linear combination determines the fraction of the components (f_k). Pixels with three components will lie inside the triangle formed by all three phasors.

$$g_{i,j}(\omega) = m_{i,j}\cos(\varphi_{i,j})$$

$$s_{i,j}(\omega) = m_{i,j}\sin(\varphi_{i,j})$$

Equations 3.1 and 3.2. ω is the laser repetition angular frequency (angular frequency of light modulation), $m_{i,j}$ is the modulation, $\varphi_{i,j}$ is the phase of the emission ($m_{i,j}$ and $\varphi_{i,j}$ with respect to the excitation), and the indexes *i* and *j* identify a pixel of the image.

$$g_{i,j}(\omega) = \sum_k \frac{f_k}{1+(\omega\tau_k)^2}$$

$$s_{i,j}(\omega) = \sum_k \frac{f_k\omega\tau^2}{1+(\omega\tau_k)^2}$$

Equations 3.3 and 3.4. f_k is the intensity weighted fractional contribution of the component with lifetime τ_k.

The phasor approach to calculating FRET efficiency is based on its classical definition (Equation 3.5). First, the phasor of the donor in the absence and independently in the presence of the acceptor is obtained. Then, all possible phasors that are quenched with different efficiencies are calculated, resulting in a curved trajectory. The amount of quenching (i.e. FRET efficiency) is determined by the position along the trajectory of the experimental phasor of a given pixel.[46]

$$E = 1 - \frac{\tau_{da}}{\tau_d}$$

Equation 3.5. FRET efficiency *E*. τ_{da}/τ_d is the ratio of the lifetime of the donor in the presence of an acceptor to that in the absence of an acceptor.[47]

To study the various conformational states nAChR adopts, we aimed to measure FRET efficiency (i.e., distance) using FLIM between many pairs of residues on nAChR expressed in *Xenopus* oocytes in the presence and absence of agonists, allosteric modulators, and antagonists. We aimed to develop a FLIM-FRET assay using our previously described (Chapter 2) fluorescent labeling strategy – the site-selective incorporation of a turn-on fUAA on nAChRs *in vivo*. We describe our strenuous attempts to measure and understand the lifetime phasor plots of our turn-on fUAA, Tz-Bodipy, along with other dyes on the mouse muscle nAChR in *Xenopus laevis* oocytes using FLIM. We also describe our efforts to increase the signal-to-noise ratio by imaging membrane patches as opposed to whole cells.

3.3 Results and Discussion

Creating a phasor 'fingerprint' map

In order to calculate the FRET efficiency, the phasor plot of a donor only sample as well as of autofluorescence must first be mapped, essentially creating a 'fingerprint' map. We measured the lifetimes of all molecular and chemical species that we use to build our FLIM-FRET assay, including autofluorescence of *Xenopus* oocytes, Tz-Bodipy, and various αBtx-dyes. In the phasor approach, these lifetimes are measured and transformed into *g* and *s* phasor coordinates.

Autofluorescence near membrane is predominantly retinoic acid

The lifetime decay of intracellular autofluorescence near the plasma membrane in the oocyte was measured. The phasor plot shows one major fluorescent species, likely to be retinoic acid (RA) when comparing its phasor plot to that of pure RA from previously published data[48] (Figure 3.1). RA, with an absorbance around 350 nm[49], and its receptors have been identified in *Xenopus* oocytes for over a decade.[50] Based on this, RA is likely the molecular species observed under TIRF and FLIM imaging.

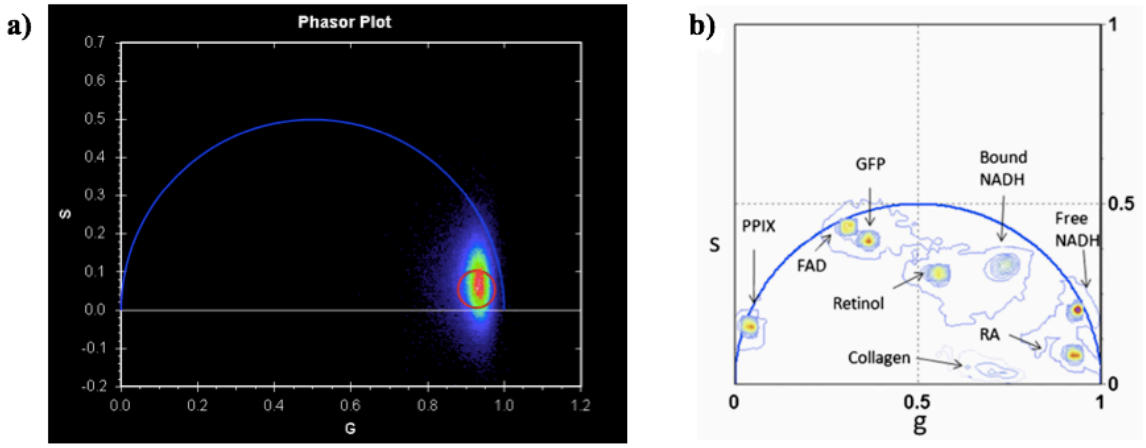

Figure 3.1. (a) Phasor plot of the molecular species in *Xenopus* oocytes. (b) Phasor plot of RA amongst other molecular species excited at 900 nm.[48]

Imaging whole cell oocyte with fluorescent beads

To verify that we are measuring lifetimes at and near the cellular plasma membrane, we image a plain uninjected oocyte atop 200-nm (diameter) fluorescent beads that have an excitation and emission wavelength of 365 nm and 415 nm, respectively (Figure 3.2d). In the phasor approach to FLIM, we can relate the phasor plot to an image. We first measure the lifetime of the fluorescent beads alone, resulting in the phasor plot (Figure 3.2a). We then generate the phasor plot of the cell atop beads system (Figure 3.2b). The pixels in the FLIM image with lifetimes that are encompassed in the circle on the phasor plot are colored with the corresponding color. For example, the pixels corresponding to the phasor points in the green circle are highlighted green in the FLIM image. The resulting FLIM image clearly shows small round features corresponding to the fluorescent beads, as highlighted in green (Figure 3.2c).

Towards shorter lifetimes (i.e., near g, s coordinates of 1, 0), the non-bead molecular species are highlighted, indicating that the region of the phasor plot near the red circle is the phasor of the cellular species. We believe that the cellular species is RA given the short lifetime of RA and by comparing the phasor plot in Figure 14. RA and the fluorescent beads are unlikely to exhibit FRET. Thus, the phasor plot should feature points that correspond to a linear combination of the two lifetimes, namely from pixels that have fluorescence from RA and beads.

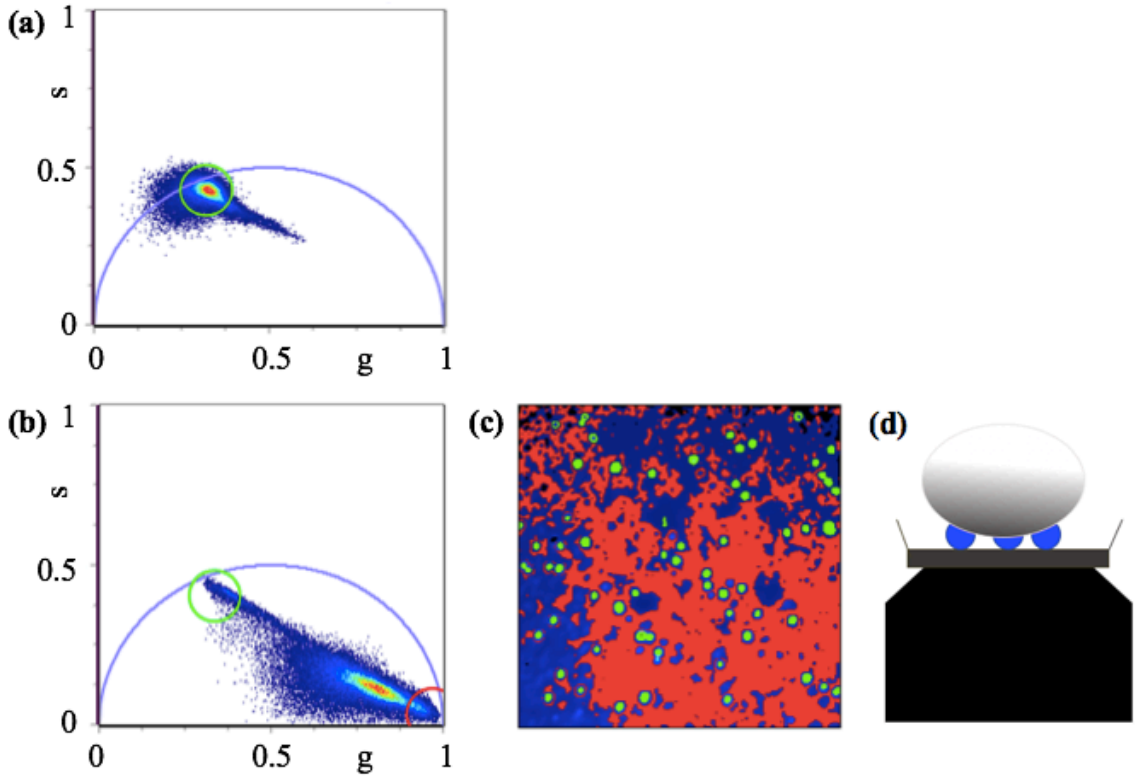

Figure 3.2. (a) Phasor plot of 200 nm Microspheres (Life Technologies) fluorescent beads that have an excitation/emission wavelength of 365/415nm and were excited at 740 nm. Lifetime of the beads is measured to be 3.2 ns. (b) Phasor plot, (c) FLIM image, and (d) schematic of fluorescent beads and plain oocyte excited at 740 nm. Green and red colors on the FLIM image correspond to the points within the green and red circles in the phasor plot.

Membrane photodamage from 2-photon excitation

The laser power had to be reduced to as low as 1% (6 mW) due to damage to the membrane from 2-photon excitation. A previous paper that published the 'fingerprint' map of intracellular autofluorescent species used 5 mW in laser power to excite live tissue.[48] Above 2% (12 mW) in laser power, small bubbles formed on the plasma membrane at the site of excitation, indicative of photodamage, which was problematic for data collection. The bubbles created too much light scattering and oversaturated the detector.

Most FLIM instrumentation is set up using 2-photon excitation, due to the ease of modulation for lifetime acquisition with a 2-photon laser. Very few FLIM microscopes are set up using a 1-photon laser. A one-photon laser system exists at UC Irvine in Enrico Gratton's lab, although it is set up with a iCCD camera, which generally has poorer resolution than the

new state-of-the-art EMCCD cameras. We constantly are striking a balance between availability, accessibility, and resolution of our instrumentation, as well as other factors concerning our biological system such as photodamage and signal-to-noise ratios. For our biological system with nonsense suppression, expression of fluorescently labeled nAChRs is quite low, risking low signal-to-noise ratios compared to expression of FPs. Because there is not much that can be done to the biological expression system to increase protein expression by a substantial magnitude, increasing the laser power can help strengthen the signal. However, due to the oocyte's whole-cell sensitivity towards photodamage in 2-photon excitation, we attempt to eliminate this issue by imaging plasma membrane patches.

Membrane patch imaging

Membrane patching adds an additional variable to our methodology. Because we are no longer working with a live whole cell, we will need to test that the ion channels are still similarly functional *in vitro* in the membrane patches. Experimentally, membrane patching adds time and variation. To prepare whole cells for imaging, the vitelline membrane, a clear membrane outside of the plasma membrane of *Xenopus* oocytes, needs to be manually removed; this process helps the oocyte stick to the imaging glass slide. The success rate of this process depends on the human preparer, and with experience, the success rate can be as high as 90%. However, the process of stripping the oocyte to a membrane patch has a success rate of less than 50% – even with a batch of healthy oocytes and on a good day with very careful hands. About ten times as many oocytes need to be prepped for imaging membrane patches than for imaging whole cells. In whole cell imaging, the visibly large cell acts as a guide to find the area of interest, but searching for the membrane patch, as it is largely transparent, becomes more time-consuming and requires a trained eye.

Imaging buffer does not have a fluorescence lifetime signal

Membrane patches are prepared in ND96 Ca^{2+}-free buffer, which was imaged with FLIM and analyzed using the phasor approach. It does not have a fluorescence signal. The periodic nature of the signal seen in the phasor plot indicates detector noise signal (Figure 3.3).

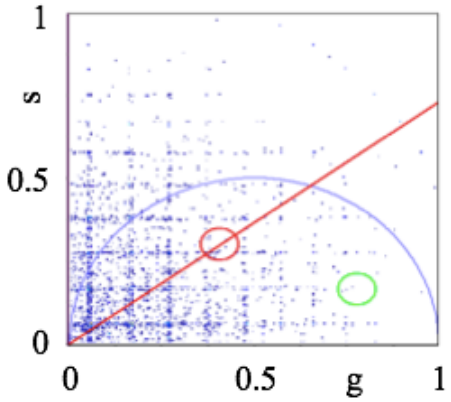

Figure 3.3. Phasor plot of ND96 Ca^{2+}-free buffer. Periodic signal indicates signal is due to detector noise.

FLIM and TIRF imaging of oocyte membrane patch

Imaging the membrane patch of uninjected oocytes using FLIM reveals a phasor footprint different to that of whole cell (Figure 3.4). We also check that membrane patching has not perturbed the fluorescence signal by imaging oocytes expressing wildtype mouse muscle nAChR labeled with α-Bungarotoxin Alexa Fluor 488 (αBtx-488). The TIRF images of the whole cell (Figure 3.5a) and the membrane patch (Figure 3.5b) show a reduction in background signal corresponding to intracellular autofluorescence.

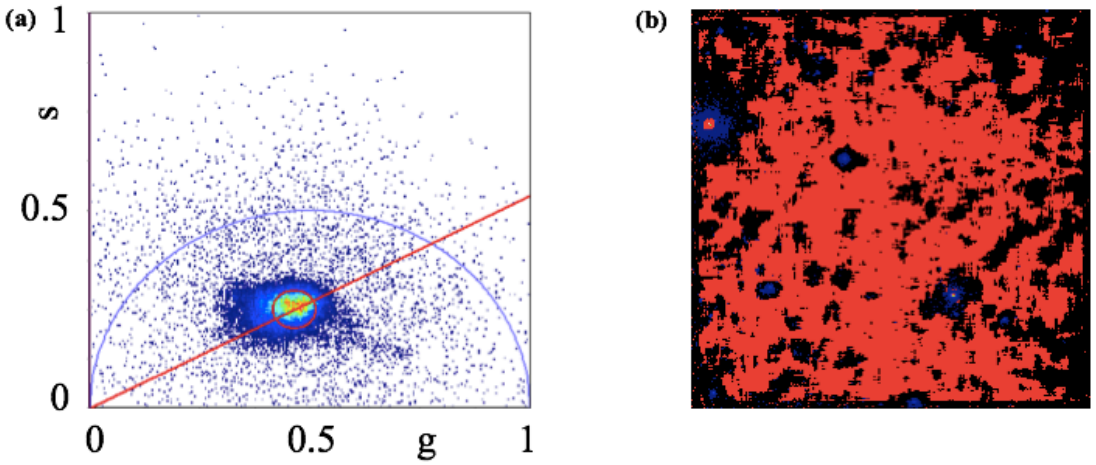

Figure 3.4. (a) Phasor plot and (b) FLIM image of a membrane patch of a plain, uninjected oocyte. A large spread of points in the phasor plot is due to low signal from the sample. The measured lifetime is 3.21 ns.

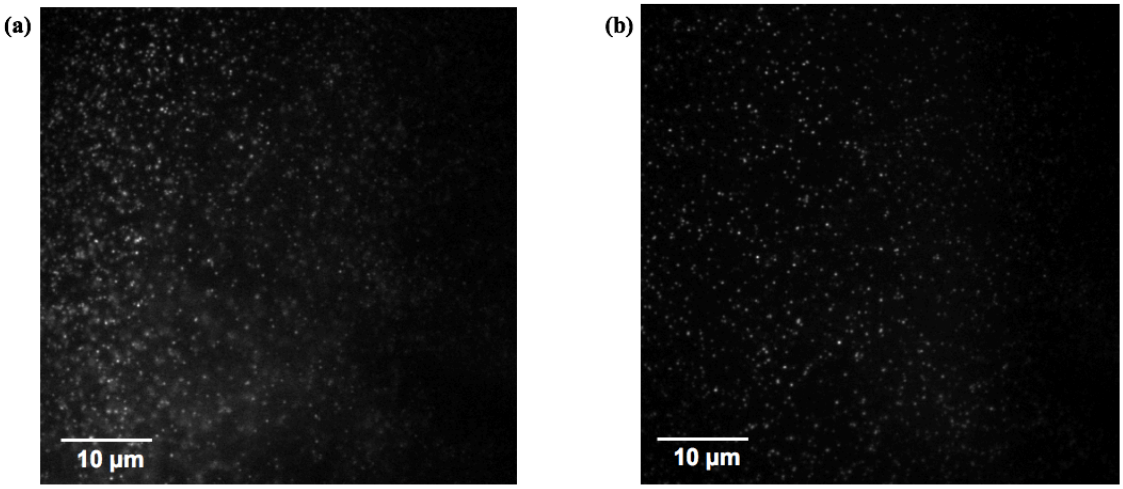

Figure 3.5. TIRF images of (a) whole cell and (b) membrane patch of the same oocyte expressing mouse muscle nAChR labeled with αBtx-488.

Phasor plots of Tz-Bodipy, αBtx-488, and αBtx-555 in solution and in vivo

After mapping the phasors of the biological specimen, namely autofluoresence, we have to map the phasors of the dyes *in vivo*. The phasors of the dyes in solution were measured to help interpret the dyes *in vivo* because dyes *in vivo* will be a linear combination of the dyes and cellular species, e.g. autofluorescence. The phasor lifetimes of αBtx-488 and activated Tz-Bodipy (i.e., Tz-Bodipy reacted with an excess of BCN-OH) in solution were measured. The lifetime from the phasor plot is interpreted as the center, which has the highest number of pixels in the FLIM image that correspond to that lifetime. The phasor plots of the dyes lie on the universal circle, indicating a single exponential, since there is only one fluorescent species (Figure 3.6). The measured lifetime of αBtx-488 has a single lifetime of 3.89 ns (Figure 3.6a), compare to 4.1 ns previously measured[51]. Similarly, the measured lifetime of activated Tz-Bodipy lies on the universal circle and is a single exponential of 3.02 ns (Figure 3.6b).

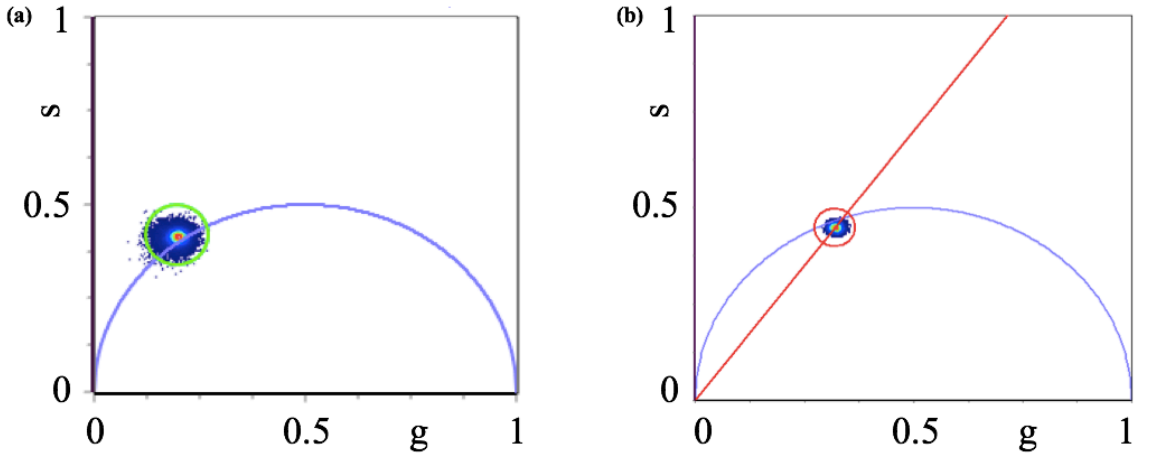

Figure 3.6. Phasor plots of (a) αBtx-488 in solution with a measured lifetime of 3.89 ns and (b) Tz-Bodipy with BCN-OH in solution with a measured lifetime of 3.02 ns.

We attempted to measure the lifetime and phasor plot of Tz-Bodipy *in vivo* but acquiring easily interpretable signals was difficult. Much of the effort described in this chapter was driven towards decomposing the phasor plot and verifying that the phasor plot corresponds to Tz-Bodipy. Theoretically, the phasor plot of Tz-Bodipy *in vivo* should be a linear combination of the dye in solution and autofluorescnece. We express mouse muscle nAChR labeled with Tz-Bodipy in *Xenopus* oocytes, prepare the membrane patches, and the image them. The resulting phasor map of the Tz-Bodipy *in vivo* sample does not lie on the universal circle, indicating multiple lifetime exponentials (Figure 3.7).

Tz-Bodipy may be contributing a low signal in the *in vivo* sample because our nonsense suppression methodology tends to lower protein expression, and thus the number of fluorescent dyes, substantially. Therefore, we tested the sensitivity of the FLIM system by imaging membrane patches of oocytes expressing wildtype mouse muscle nAChR with αBtx-488 and αBtx-555 labeling – the signal should be orders of magnitude higher as wildtype mouse muscle nAChR expression is very high. First, to interpret the phasor plot of the sample *in vivo*, we measure the phasor lifetimes of the dyes in solution (Figure 3.8). We acquire the phasor lifetimes of αBtx-488 and αBtx-555 mixed together in solution at different ratios, which shows a perfect linear combination of the lifetime exponentials. The measured lifetime of αBtx-555 in solution is 1 ns, whereas published results indicate a 0.3 ns lifetime[51]. The phasor plots of membrane

patches of ooctyes expressing wild type nAChR labeled with αBtx-488 only and co-labeled with both αBtx-488 and αBtx-555 have similar phasor plots, suggesting that αBtx-488 dominates the signal (Figure 3.9).

There is substantial variability amongst *in vivo* samples under the same conditions. Two similarly prepared *in vivo* samples with Tz-Bodipy and αBtx-555 co-labeling have different phasor maps (Figure 3.10 and 3.11). The signal near (g, s) of (1, 0) in Figure 3.10 and 3.11 is fluorescence from retinoic acid due to insufficient washing of the membrane patches. The phasor plot of different membrane patches and on different oocyte batches shows variation. There are two distinct clusters of phasor liftimes for the same condition but different membrane patches (Figure 3.10). Further validation is necessary to verify the phasor footprint is that of Tz-Bodipy.

When comparing the phasor maps of αBtx-555 in solution to *in vivo*, either αBtx-555 has a wildly shifted lifetime *in vivo* or αBtx-555 fluorescence is not being captured. We investigate this by measuring the emission intensity over a spectrum of wavelengths for the two dyes. We observe that the emission intensity of αBtx-488 is about twenty times higher than that of αBtx-555 at a 2pe wavelength of 900 nm, considering that the laser power exciting αBtx-555 is twice that of αBtx-488 (Figure 3.12). This discrepancy in emission intensity may explain why αBtx-555 is not observed *in vivo* in the presence of αBtx-488 but not why it is not observed *in vivo* alone.

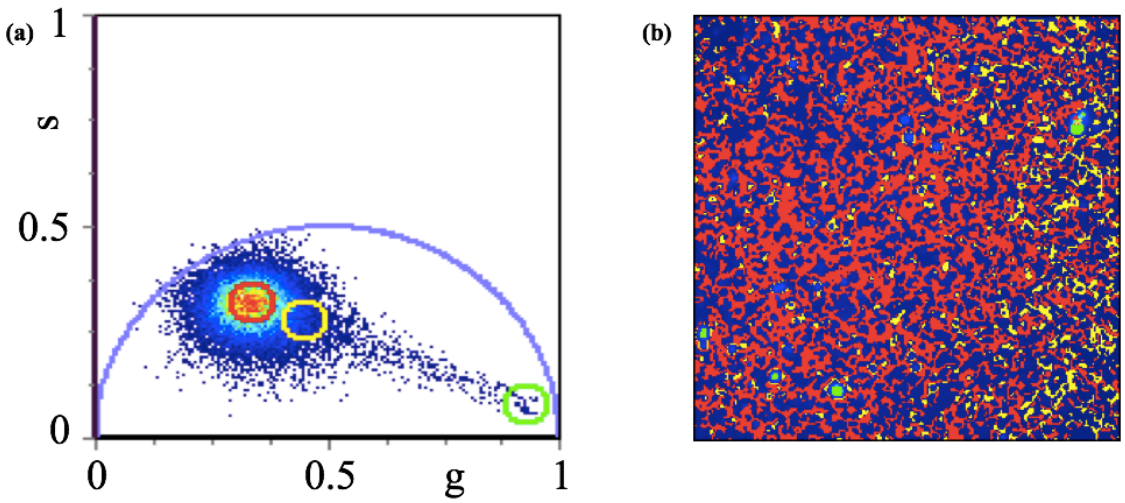

Figure 3.7. (a) Phasor plot of a membrane patch of an oocyte expressing α70-nAChR labeled with Tz-Bodipy. Measured lifetime is 3.19 ns (for red circle).

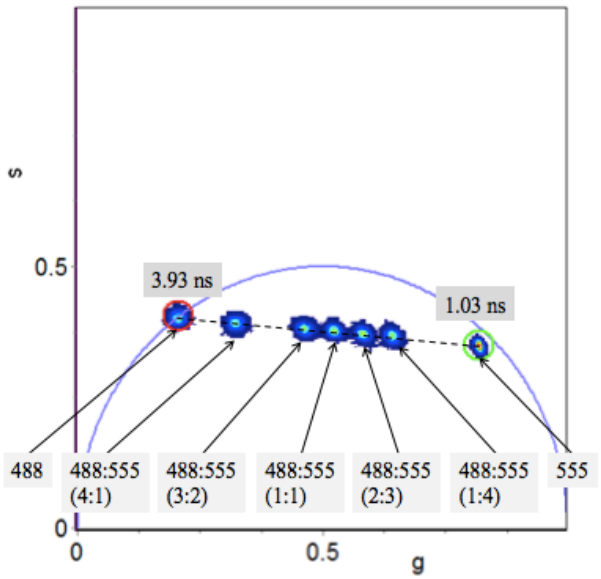

Figure 3.8. Phasor plots of αBtx-488, αBtx-555, and a mixture of the two dyes at different ratios in solution superimposed onto one plot. The phasor of αBtx-488 (lifetime of 3.93 ns) and of αBtx-555 (lifetime of 1.03 ns) lie on the universal circle, suggesting a single exponential lifetime. The lifetimes of the mixtures are a linear combination of the two dyes, and the location of the phasor is shifted towards the higher concentration dye.

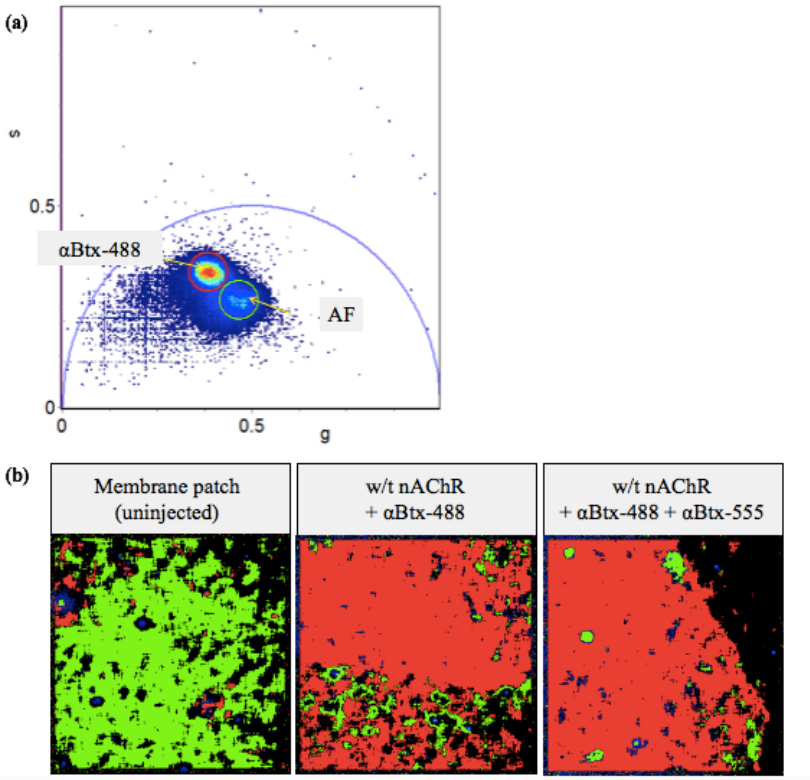

Figure 3.9. Individual phasor plots for each FLIM image in (b) are superimposed into one phasor plot (a). Each FLIM image and phasor plots are of different membrane patches of an oocyte: not transfected (uninjected), expressing wildtype (w/t) mouse muscle nAChR labeled with αBtx-488 only or co-labeled with αBtx-555.

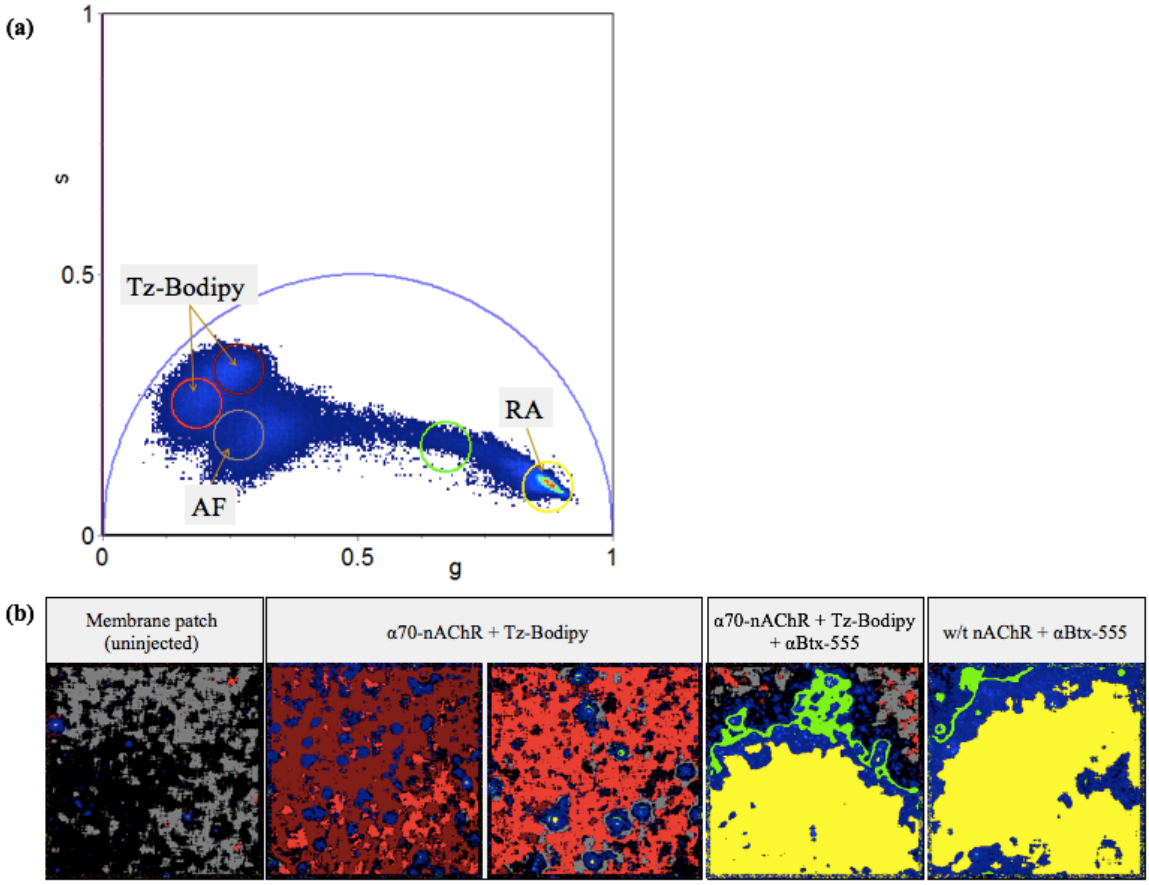

Figure 3.10. Individual phasor plots for each FLIM image in (b) are superimposed into one phasor plot (a). Each FLIM image and phasor plots are of different membrane patches of an oocyte: not transfected (uninjected), expressing mouse muscle mutant α70-nAChR with Tz-Bodipy only or co-labeled with αBtx-555, or wildtype (w/t) mouse muscle nAChR labeled with αBtx-555.

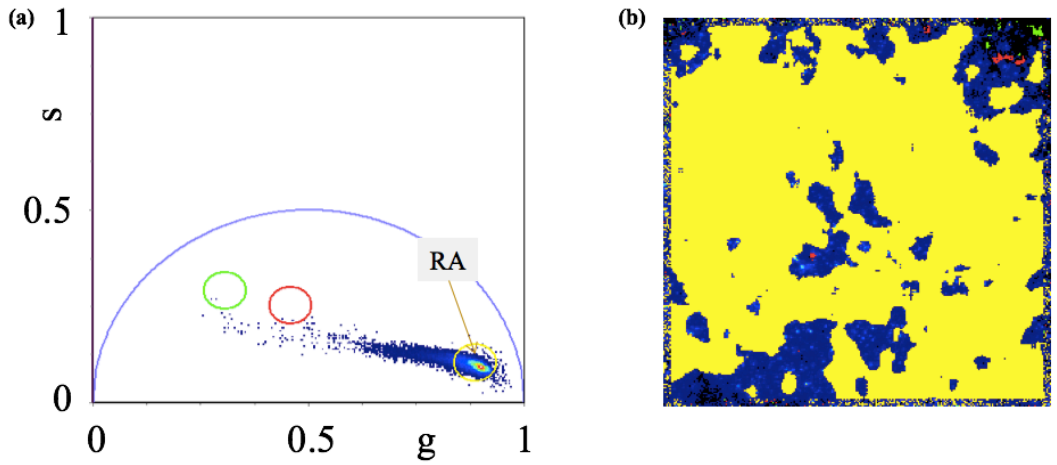

Figure 3.11. (a) Phasor plot and (b) FLIM image of a membrane patch of an oocyte expressing α70-nAChR labeled with Tz-Bodipy and αBtx-555. Green and red circles indicate location on the phasor plot that Tz-Bodipy and autofluorescence have been observed in other samples. The signal in the yellow circle is likely retinoic acid (RA).

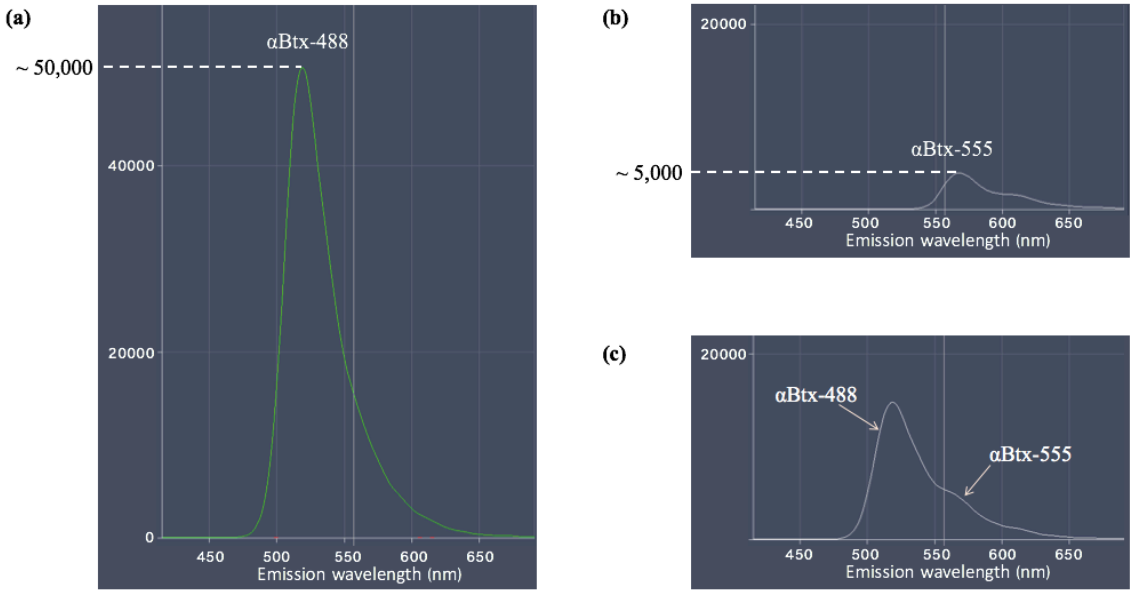

Figure 3.12. Fluorescence emission intensity spectra of (a) αBtx-488 at 15% laser power, (b) αBtx-555 at 30% laser power, and (c) a 1:1 mixture of αBtx-488 and αBtx-555.

3.4 Conclusions

Overall, the fluorescence labeling technique via unnatural mutagenesis and tetrazine click chemistry with Bodipy poses severe limitations with low signal-to-noise ratios due to 2-photon excitation and FLIM imaging. The phasor approach to FLIM is a powerful technique, as it allows a lifetime, i.e. phasor plot, to be mapped to an image. However, the assay we attempted to build does not fully utilize the power of this technique. Our expression system, i.e. oocytes, and the membrane patches covers the whole image field relatively uniformly. Although FLIM is a theoretically more robust technique for FRET, there are many other issues that arise. Whole-cell oocyte fluorescence lifetime imaging with 2-photon excitation results in either membrane photodamage or intracellular autofluorescence signal that overpowers target fluorescence signals, e.g. Tz-Bodipy. Imaging membrane patches has reduced autofluorescence signal, as seen in both FLIM measurements and TIRF images. However, variability between samples of the same conditions is large, and the signal from Tz-Bodipy is weak. If these variations are accounted for and signal-to-noise ratios can be improved, a robust strategy for the incorporation of a second fluorophore will eventually need to be developed to perform FRET studies.

3.5 Experimental Methods

Oocyte preparation, dye preparation, and TIRF imaging is described in Chapter 2 Experimental Methods.

3.5.1 Membrane Patching

The vitelline membrane of the oocyte is first manually removed as described in Chapter 2 and then immediately placed on glass Petri dishes filled with ND 96 Ca^{2+}-free buffer. Oocytes are placed side-by-side, essentially maximally packing the glass slide with oocytes. The de-vitellinized oocytes are left on the glass slides for at least 20 minutes. The oocytes are then forcefully removed using a glass Pasteur pipette, leaving a patch of membrane on the glass slide; the success rate is ~50%. If any of the intracellular yolk is leaked into the buffer, this will reduce the success of patching to near 0%. The membrane patches are then washed at least 10 times by exchanging the buffer; only a maximum of 90% of the buffer is removed at any time because if the membrane patch is exposed to air, the patch disappears. The membrane patches are then imaged immediately.

3.5.2 FLIM Imaging

A Zeiss LSM-780 inverted confocal microscope (Carl Zeiss Microscopy) with 2-photon excitation (Chameleon femtosecond Ti:Sa laser) was used to acquire fluorescence lifetime data. A LD C-Apochromat 63x/1.15 W Korr M27 objective was used. Data were acquired using the FLIM Box (ISS) with a sampling rate of 300 MHz, pixel dwell time of 12.61 microseconds, and scan time of 1.94 seconds. All FLIM images are 256 by 256 pixels with a pixel size of 0.53 μm, resulting in an image size of 134.4 by 134.4 μm. The spectral emission filters ranged from 467 to 499 nm and 524 to 550 nm. A dichroic filter of 538 nm was used. FLIM data for validating the phasor approach calculations were calibrated using coumarin 6 (Sigma-Aldrich, dissolved in 100% ethanol) with a lifetime of 2.55 ns. Data were analyzed using the GLOBALS for Images software (Laboratory for Fluorescence Dynamics, UCI, Irvine, CA) and Vista Vision. Samples were excited at a 2-photon wavelength of 900 nm unless noted otherwise.

Chapter 4

EFFORTS TOWARD DEVELOPING A FLIM-FRET ASSAY FOR LGICS IN COS-7 CELLS

4.1 Abstract

The phasor approach to FLIM is most powerful when applied to a system that takes advantage of lifetime differences that can be mapped to physical attributes in a FLIM image. We made initial attempts in applying this technique towards building a FLIM-FRET assay to study LGICs expressed in mammalian cells. This chapter describes efforts to image fluorescent protein fused to the $5HT_3$-A/B serotonin receptor expressed in COS-7 monkey kidney cells using confocal microscopy and measured lifetimes using FLIM and the phasor approach. We made preliminary attempts to calculate the FRET efficiencies of $5HT_3$-A(CYP)/B(YFP) at the plasma membrane by applying a masking of the phasor signal, but results do not match published results. Continued investigation is needed to validate our approach.

4.2 Introduction

Previously, the stoichiometry of the $5HT_3$-A/B receptor was studied using fluorescence recovery after photobleaching (FRAP), an intensity-based FRET approach, in HEK283T mammalian cells, revealing a $5HT_3$-A_3B_2 stoichiometry. This study noted a difference in FRET efficiencies between measuring fluorescence signal from whole cells and membrane sheets. Fluorescence signal from receptors in plasma membrane is usually overcome by fluorescence from receptors in the endoplasmic reticulum (ER) in whole cell imaging. The ER network extends throughout the cytosol in a netlike labyrinth of branching tubules and flattened sacs, and its membrane is where all transmembrane proteins are produced.[52]

In this chapter, we describe our efforts to investigate whole cell imaging of COS-7 cells for the development of a FLIM-FRET assay for the $5HT_3$-A/B receptor. The COS-7 expression system could be advantageous for whole cell imaging. We hypothesize that the ER network, although may extend throughout the cytosol, may not extend as prominently into the outer regions of the cell due to its relatively flat morphology. To test this new expression system, we first attempted to reproduce the FRET results of the prior study of $5HT_3$-A/B stoichiometry[20] using the phasor approach to FLIM imaging and a COS-7 mammalian cell expression system. We imaged COS-7 cells expressing $5HT_3$-A/B receptors fused to CFP and YFP using confocal microscopy and measured lifetimes using FLIM. Several imaging and post-processing methods to capture fluorescence signal from the plasma membrane are also discussed. Successful implementation of this technique would allow us to ask questions surrounding protein stoichiometry, trafficking, protein-protein interactions, and other biological processes in the context of cellular compartmentalization.

4.3 Results and Discussion

ER Network in COS-7 Cells

First, we studied how the ER is distributed in COS-7 cells with hopes of finding that the distribution of ER across the cell is less prominent in the outer regions. Imaging COS-7 cells transfected with $5HT_3$-A(YFP)-B using a confocal microscope reveals its morphology as well as an ER network (Figure 4.1a). The ER has a netlike organization (Figure 4.1b)[52]. The ER appear to not extend to the outermost region of the cells (circled in red, Figure 4.1a).

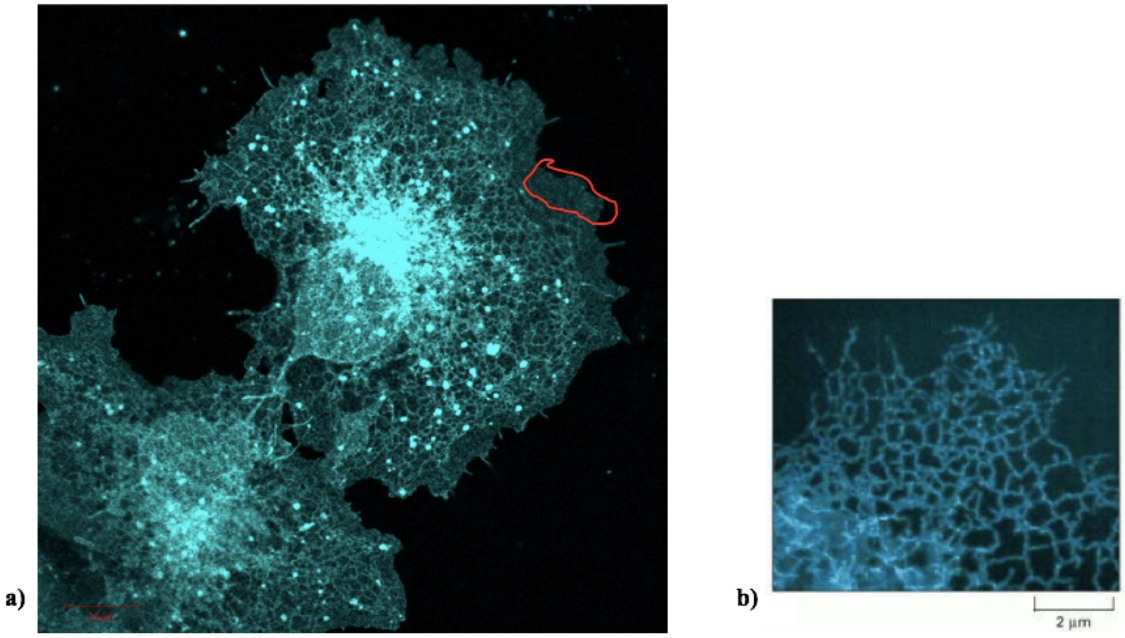

Figure 4.1. (a) Confocal image of two COS-7 cells undergoing cell division during cytokinesis. COS-7 cells were transfected with $5HT_3$-A(YFP)-B. Scale bar is 20 microns. Circled in red appears to be one region of the cell that ER does not extend to. (b) Part of the ER network in a cultured mammalian cell, stained with an antibody that binds to a protein retained in the ER.[52]

To further probe the ER, we imaged COS-7 cells transfected with $5HT_3$-A(YFP)-B as well as the mPlum fluorescent protein targeted to the Golgi and the mCherry targeted to the ER (Figure 4.2). It was difficult to distinguish ER, Golgi, and plasma membrane from these transfection conditions. Testing different transfection amounts of DNA could help find better labeling conditions of these organelles. However, labeling cells with a chemical small-molecule dye was a more straightforward approach.

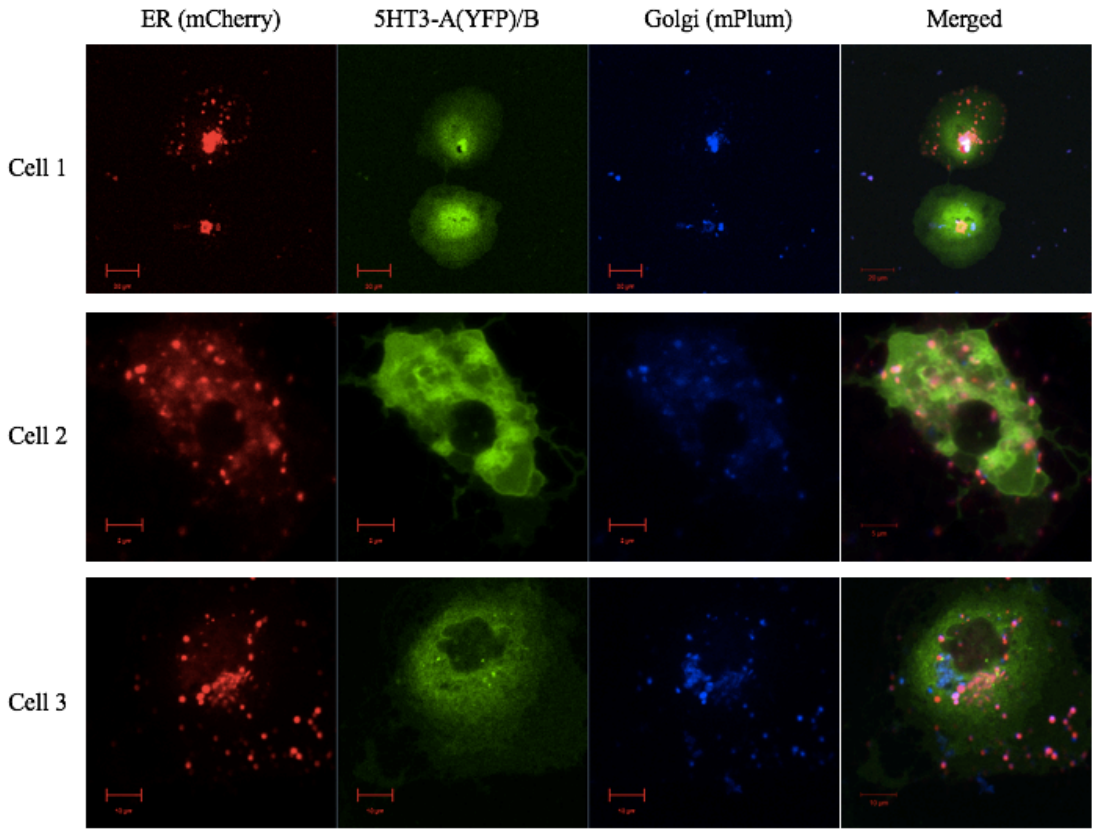

Figure 4.2. Confocal images of COS-7 cells transfected with $5HT_3$-A(YFP)-B, Golgi-targeted mPlum, and ER-targeted mCherry. Each column represents a different emission channel for that particular fluorescent protein, or all of them merged. Scale bar is ten microns.

Plasma membrane and ER of COS-7 cells were successfully imaged using chemical dyes on a confocal microscope. ER was the main target because of its supposed large reach in the whole cell, as compared to the Golgi. A Golgi-targeted chemical dye was not used, as it was not easily accessible. COS-7 cells transfected with $5HT_3$-A(YFP)/B were co-labeled with ER-Tracker™ Red (BODIPY TR Glibenclamide) to stain the ER and CellMask Deep Red to stain the plasma membrane. These dyes were selected to have minimal overlap in their emission spectra with each other and YFP (Figure 4.3). The image of these COS-7 cells clearly shows that a high density of the fluorescence from YFP is in the ER (Figure 4.4). That is, most of the $5HT_3$-A(YFP)/B protein is trapped in the ER and not trafficked to the plasma membrane.

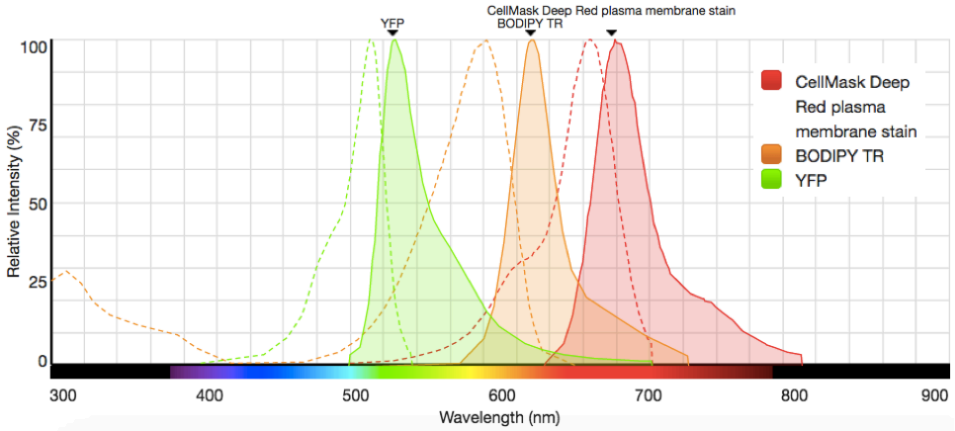

Figure 4.3. Excitation (dotted line) and emission (solid line) spectra of CellMask Deep Red, BODIPY TR, and YFP generated from ThermoFisher Scientific website.

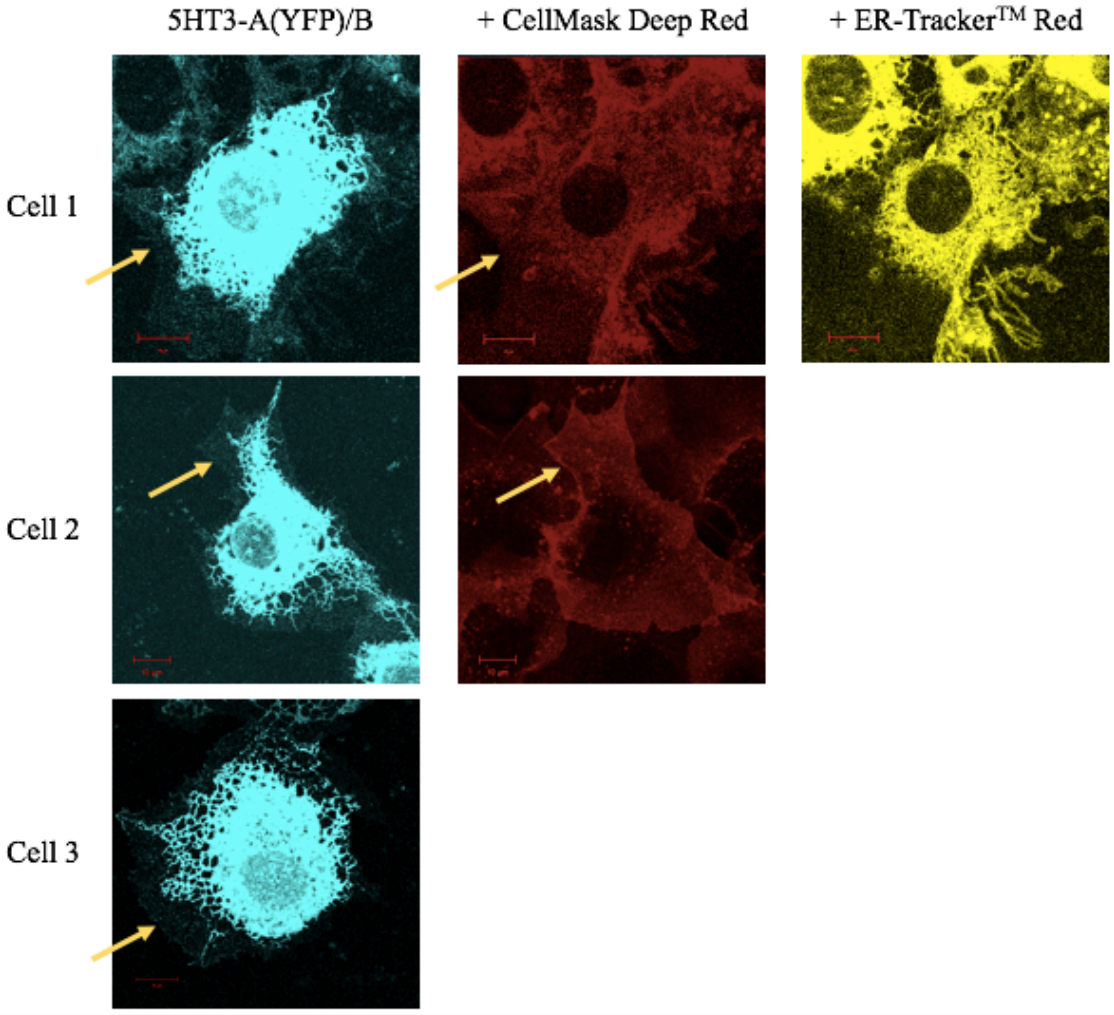

Figure 4.4. Confocal images of COS-7 cells transfected with $5HT_3$-A(YFP)-B stained with ER-Tracker™ Red and CellMask Deep Red. Each column represents a different emission channel for that particular fluorescent protein. Yellow arrow points to the perimeter of the cell membrane. Scale bar is ten microns.

Mapping the phasors of different regions of the cell in the x-y plane

To understand how lifetime of our $5HT_3$-fluorescent protein fusions may vary within a cell, we measure the lifetime phasors for different regions of the cell using FLIM and analyzing using the phasor approach. We zoom in on the outer region primarily for plasma membrane, and also select inner regions corresponding to the nucleus, ER, and Golgi. The phasor coordinates for each region do not show any marked trends within the cell expressing $5HT_3$-A(CFP)/B(YFP) and across two different cells (Figure 4.5). We hope to see reproducibility of the phasor plots for each region, but this approach of zooming into regions may not be most suitable. Post-acquisition "masking" of the signal from whole cell imaging to filter the signal to the outer region, i.e. possibly plasma membrane, is an attractive alternative.

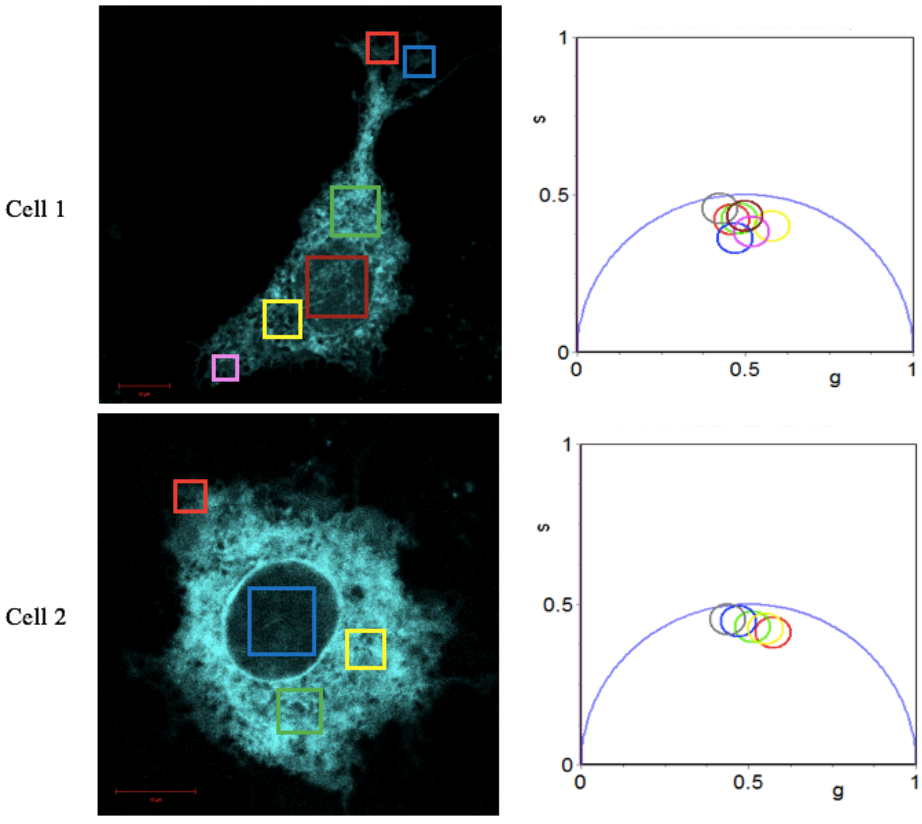

Figure 4.5. Confocal image (left) and phasor plot (right) of COS-7 cells transfected with $5HT_3$-A(CFP)/B(YFP). Phasor coordinates are not shown. Gray circle in the phasor plot indicates phasor from imaging the whole cell. The colors in the phasor plot correspond to imaging the region of interest as indicated in the confocal image. Scale bar is ten microns.

The periphery of the COS-7 cells appears to have a longer lifetime than the inner regions surrounding the nucleus (Figure 4.6). The shortened lifetime in the inner regions, corresponding to the ER and/or Golgi, may be due to intermolecular homoFRET from interactions of CFPs across neighboring receptors. We hypothesize that the lifetime (coordinates highlighted in the red circle) of the outer region most closely represents lifetime of 5HT3-A(CFP)/B on the plasma membrane.

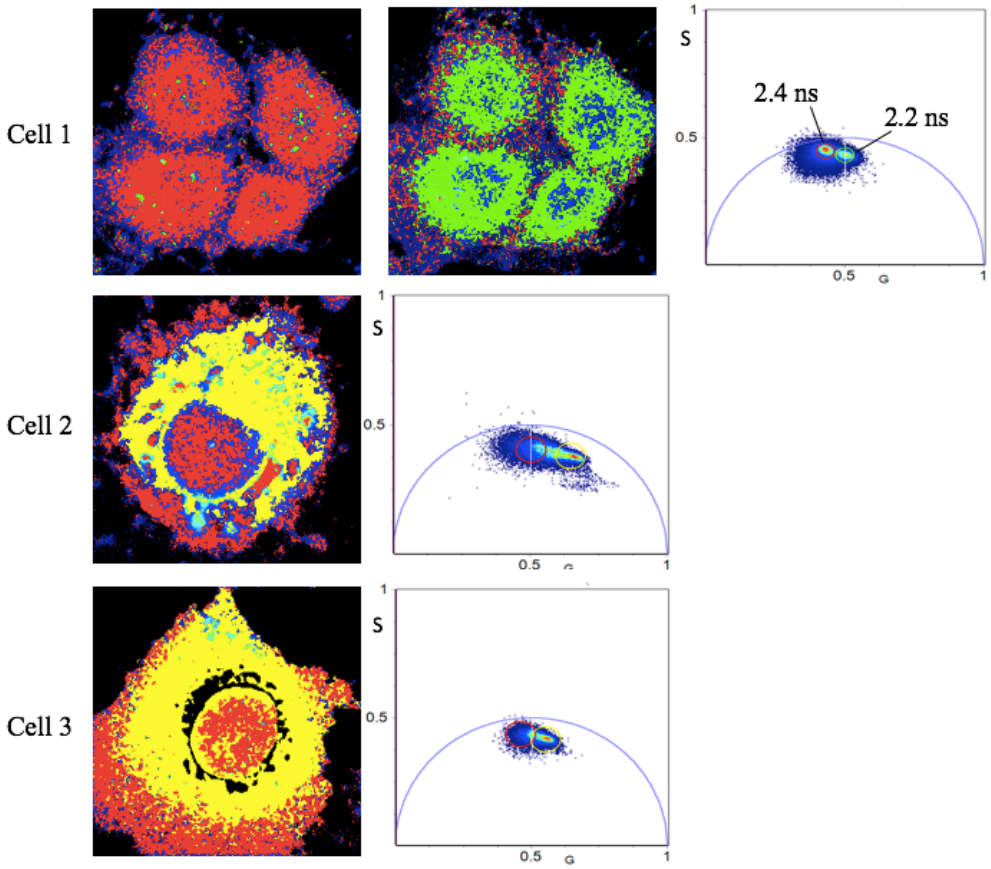

Figure 4.6. FLIM image and phasor plot of COS-7 cells transfected with $5HT_3$-A(CFP)/B. Points encircled in the phasor plot are highlighted by that color in the FLIM image.

Mapping the phasors of the whole cell in different z-planes

The morphology of COS-7 cells is similar to a fried sunny-side egg. We tested if lifetimes vary in the z-axial direction by imaging in the x-y plane as before but changing the focus, essentially imaging at different z cross-sections. The phasor plots of COS-7 cells expressing

$5HT_3$-A(CFP)/B(YFP) show little variability across different z cross-sections, but variability across different cells (Figure 4.7). The signal is dominated by fluorescence from the ER and/or Golgi. We then apply a post-acquisition mask of these measurements, removing the signal associated with the center of the cell (Figure 4.8). The resulting phasor lifetimes are on average shorter than that of whole cells without masking (Table 4.1). The important questions that remain are: 1) how significant is this lifetime difference, and 2) is the lifetime from masking a true representation of fluorescence signal from plasma membrane? These questions are difficult to answer.

	Lifetime (ns)	*N*
Whole cell	2.16 ± 0.16	4
Masked cell	2.24 ± 0.17	4

Table 4.1. Fluorescence data, $5HT_3$-A(CFP)/B(YFP). All values are reported as mean ± standard error of mean.

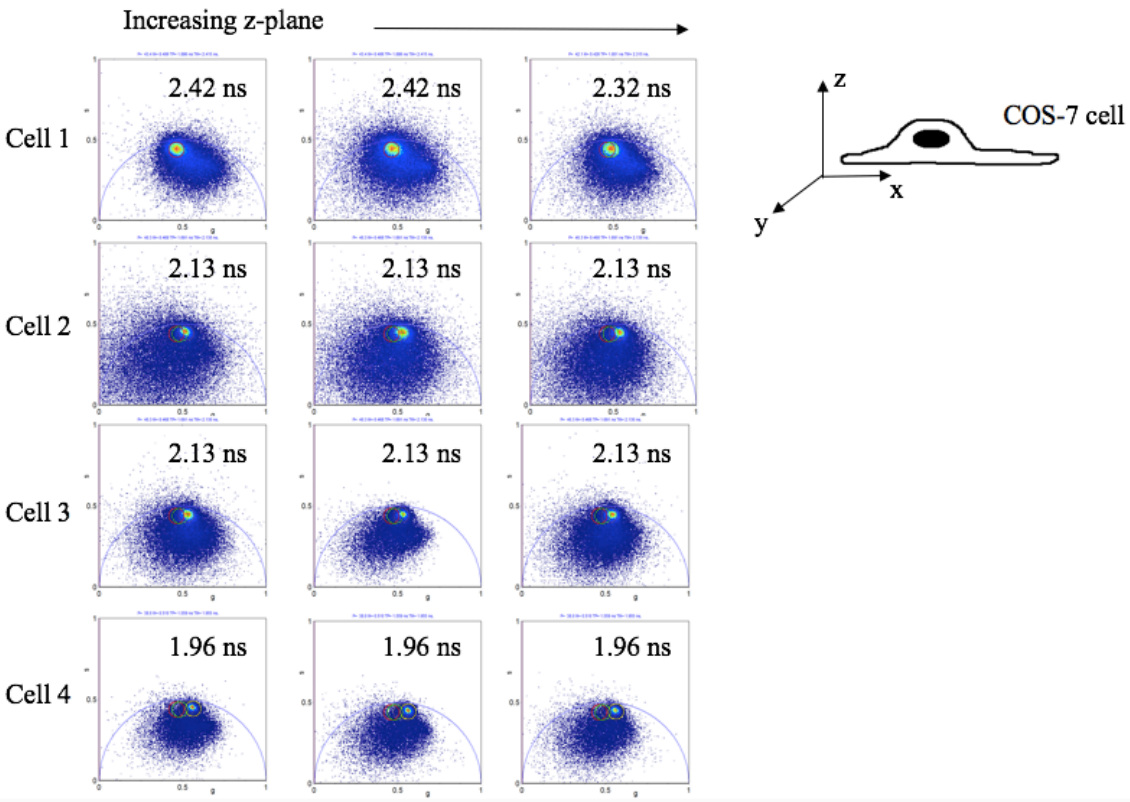

Figure 4.7. Phasor plots of COS-7 cells transfected with $5HT_3$-A(CFP)/B(YFP). Each column represents a different cross-section in the z-axial direction.

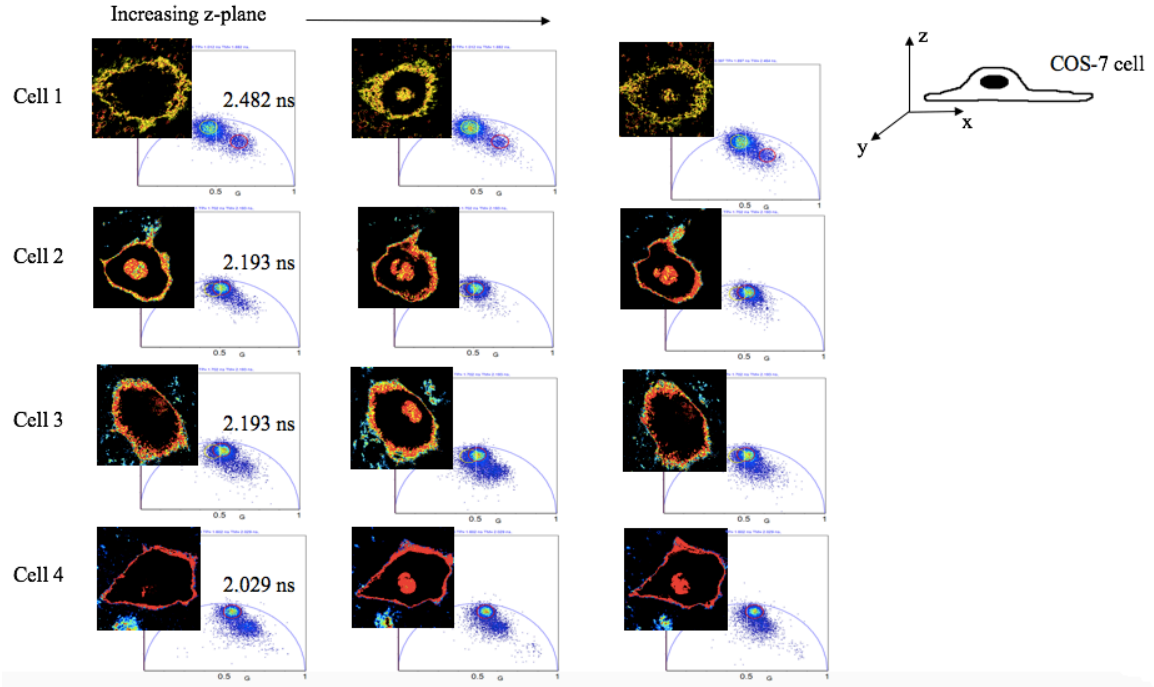

Figure 4.8. Phasor plots and FLIM image with masking of COS-7 cells transfected with $5HT_3$-A(CFP)/B(YFP). Each column represents a different cross-section in the z-axial direction.

Calculating FRET efficiency

We moved forward to making preliminary attempts to calculate FRET efficiencies despite still needing to verify our signals. The requirements for calculating FRET efficiency in the phasor approach are the phasors of the donor only, donor with acceptor (D/A), and cellular autofluorescence (AF). The autofluorescence phasor is taken from imaging untransfected COS-7 cells, and the donor phasor is taken from the masked signal of $5HT_3$-A(CFP)/B; these phasors are used as a constant input into the FRET calculator in the software. The phasor that we measure across various cells is that of D/A, $5HT_3$-A(CFP)/B(YFP). Figure 4.9 shows a schematic for the generation of the FRET trajectory and the resulting FRET efficiency (E) calculated to be 42.2% for that one particular cell expressing $5HT_3$-A(CFP)/B(YFP); this is the same data as in Cell 1 of Figure 10. FRET efficiencies were calculated for three other cells, averaging 36.6% with a standard error mean (SEM) of 1.1% (Figure 4.10).

The previous study studying $5HT_3$-AB stoichiometry, on which this study is built from, had a FRET efficiency of 26.1 ± 0.7% for the same protein constructs expressed in HEK283T

cells for membrane sheets and 15.7 ± 0.5% for whole cells[20] (Table 4.2). Our FRET result is at least 1.4 times greater than the published results. Continued investigation is needed to determine the best way to validate our FLIM-FRET approach.

	Lifetime (ns)	FRET efficiency (%)	*N*
$5HT_3$-A(CFP)/B	2.32 ± 0.18		4
$5HT_3$-A(CFP)/B(YFP)	2.24 ± 0.17	36.58 ± 2.14%	4

Table 4.2. Fluorescence data, masked cell. All values are reported as mean ± standard error of mean.

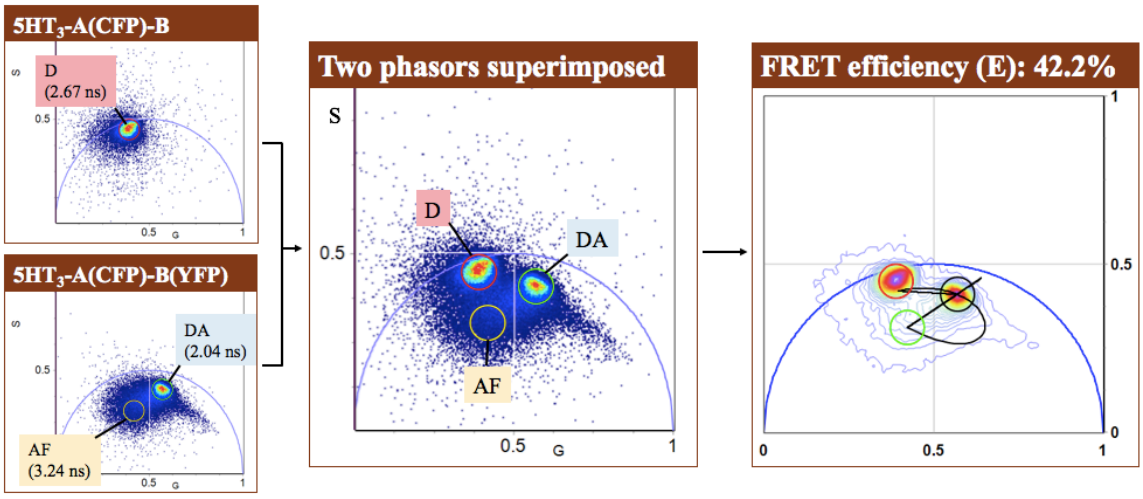

Figure 4.9. Phasor plots of $5HT_3$-A(CFP)/B (donor only, D) and $5HT_3$-A(CFP)/B(YFP) (donor CFP and acceptor YFP, D/A). Autofluorescence (AF) phasor is highlighted in the D/A phasor plot. Measured lifetime of CFP in COS-7 cells is 2.67 ns, compared to lifetimes of 2.9[53] and 3[53] ns in published studies. Most right plot shows the FRET trajectory, as calculated using the phasor approach.

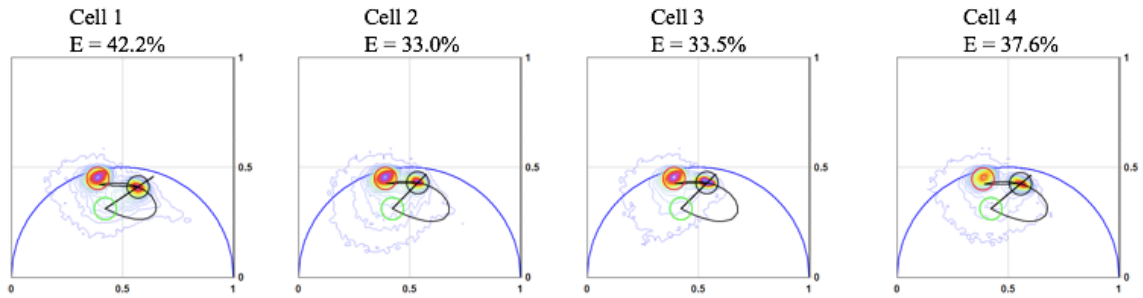

Figure 4.10. FRET trajectories and efficiencies (E) for four COS-7 cells expressing $5HT_3$-A(CFP)/B(YFP).

4.4 Conclusions

Efforts towards building a FLIM-FRET assay to study $5HT_3$-A/B receptors and reproduce published FRET results have been made. Nonetheless, great strides are still needed to determine the best method to deconstruct plasma membrane signal from the rest of the cell. For future efforts, we will need to investigate potential intramolecular homoFRET of CFP within a single receptor, as there are three $5HT_3$-A subunits (i.e., three CFPs) in $5HT_3$-A(CFP)/B(YFP). We can address the homoFRET issue by biasing transfection ratios so that there is one CFP per $5HT_3$-A/B receptor. Additionally, we will need to validate that post-acquisition masking of whole cell signal represents receptor signal on the plasma membrane, which can be addressed by performing membrane stripping of COS-7 cells and comparing the phasor results.

4.5 Experimental Methods

FLIM imaging is described in Chapter 3 Experimental Methods.

4.5.1 COS-7 Preparation and Transfection

COS-7 cells were cultured in Dulbecco's modified Eagle's medium/nutrient mix (DMEM) F12 (1:1) with 10% fetal bovine serum and gentamycin on 100 mm culture plates at 37°C and 5% CO_2 in a humidified atmosphere. Cells for imaging at 60–80% confluency were transfected on 4-well slide dishes pre-coated with poly-d-lysine (MatTek) with 100 ng of plasmid DNA using Qiagen Effectene. cDNA constructs of monomeric-enhanced CFP and YFP introduced in frame into the M3-M4 loops of the human $5HT_3$-A and $5HT_3$-B subunits were prepared by Tim Miles. $5HT_3$-A and $5HT_3$-B subunits were all mixed at a 1:1 ratio for a $5HT_3$-A_3B_2 stoichiometry[20]. Cells were imaged one day after transfection.

4.5.2 COS-7 Cell Staining

COS-7 cells transfected $5HT_3$-A/B constructs were stained by incubating with ER-Tracker™ Red and CellMask Deep Red (ThermoFisher Scientific) with a final concentration of 500 ng/mL for 5 minutes, washed twice with PBS, and then placed in phenol red-free DMEM solution. Cells were imaged immediately after washing. 100 μg of ER-Tracker™ Red and CellMask Deep Red were dissolved in 110 μL of DMSO.

4.5.3 Confocal Imaging

Live cells were imaged at room temperature on a Zeiss LSM710 confocal laser scanning microscope equipped with a Plan-Apochromat 63x, 1.4 oil DIC M27 or alpha Plan-Apochromat 100x, 1.46 oil DIC M27 objective lens. YFP, ER-Tracker™ Red, and CellMask Deep Red fluorescence signals were acquired by 514, 561, and 633 nm excitation, respectively, and the emission spectra were collected for the ranges 517–613, 579–644, and 661–740 nm, respectively. The pinhole sizes ranged from 49 to 92 microns.

Chapter 5

ACUTE EFFECTS OF MENTHOL STEREOISOMERS ON LOW-AFFINITY AND HIGH-AFFINITY α4β2 NACHRS

5.1 Abstract

Previously, Henderson, et al. have found that menthol alone enhances the upregulation of nAChRs in the midbrain, favors the expression of the low-affinity subtype stoichiometry of the α4β2 nAChR, reduces the firing frequency in DA neurons, and eliminates nicotine reward-related behavior. In that study, a racemate of menthol, the (–) and (+) stereoisomers, was used. The present work parsed the effects of the stereoisomers, finding that a the (–) stereoisomer is the active form while the (+) stereoisomer led to null effects – in chronic studies. Interestingly in acute studies, however, the two menthol stereoisomers do not show differing inhibitory effects on the α4β2 nAChR nor do they show a favorability towards either subtype stoichiometry (i.e., $(\alpha4)_3(\beta2)_2$ (low-affinity) and $(\alpha4)_2(\beta2)_3$ (high-affinity)). The effective concentration of menthol on α4β2 nAChRs is also several orders of magnitude larger in acute studies (33 μM (present work) and 111 μM (Hans, 2012)) than in chronic studies (500 nM).

5.2 Introduction

Smoking is one of the leading causes of death in the United States.[54] Since the targeted marketing and promotion of menthol-flavored cigarettes that started around the 1930s, over 80% of all menthol smokers are African American, and menthol cigarettes constitute about 27% of the total US cigarette market. It was also recently exposed that all cigarettes contain some amount of menthol despite not being marketed as such. It is the last sole remaining flavorant that is allowed to be added to cigarettes.[55] This demographic data raises controversy for menthol cigarettes because studies have shown that mentholated cigarette smokers have a lower cessation (quit) rate than "non-mentholated" cigarette smokers. Could this observation be a product of the menthol users themselves, or is something happening at a physiological and biochemical level making them more addicted? Extensive studies have pointed to a biochemical effect.

Menthol is a monocyclic terpene alcohol used in a variety of products for its minty fresh effect. The topical application of menthol to the skin or mucosal membranes makes it an attractive additive to many cosmetic products, oral health care products (e.g. cough drops and toothpaste), and tobacco cigarettes. Although menthol has been used for medicinal purposes for thousands of years and is still currently well-received for oral and cosmetic products, its use as a flavor additive in cigarettes remains controversial.

nAChRs and Smoking Addiction

Addiction to smoking due to nicotine is not uncommon knowledge. Biologically, nicotine activates nAChRs on dopaminergic neurons in the brain's mesolimbic reward system and in turn increases dopamine levels. Nicotine also interacts with nAChRs on excitatory glutamatergic and inhibitory gamma aminobutyric acid (GABAergic) neurons in the ventral tegmental area (VTA) of the brain, which either stimulate or inhibit dopaminergic neurons. The nicotinic receptor exists in 12 isoforms (variants). Based on extensive preclinical studies, the β2-, α4-, α6-, and α7-containing isoforms appear to promote the addictive, reinforcing effects of nicotine.[56]

α4β2 nAChRs and Smoking Addiction

The α4β2 receptor is the most abundant nAChR in the brain and is directly involved in tobacco addiction. Nicotine plays a dual role with α4β2 nAChRs in its addiction: upregulation and desensitization. The nicotine-induced upregulation of α4β2 receptors has been indicated as the crucial mechanism in nicotine addiction. α4β2 nAChRs are also found in most brain regions with high-affinity nicotine binding sites. α4β2 nAChRs can be formed in two stoichiometries: $(\alpha4)_2(\beta2)_3$ that has high-affinity for nicotine and $(\alpha4)_3(\beta2)_2$ that has low-affinity. Receptor desensitization due to chronic exposure to agonist (e.g. nicotine) leads to upregulation. Smokers inhale enough nicotine in cigarettes to cause α4β2 desensitization and upregulation in their brains.[57]

Menthol and Smoking Addiction

Menthol may cause smokers to have elevated nicotine concentrations in their plasma by alleviating airway irritation.[58-59] It is also possible that menthol alters the metabolism of nicotine[60], leading to increased systemic nicotine exposure, and may increase the nicotine concentration in blood by ~20%[58, 61]. Altogether, these observations are still insufficient to account for menthol's role in upregulation of β2-containing nAChRs previously observed[62], which is important as upregulation is ultimately the central mechanism to smoking addiction. However, a recent 2016 finding by Henderson, et al. has revealed that menthol alone also contributes on a biochemical level to smoking addiction. They found that menthol, by itself, enhances the upregulation of nAChRs in the midbrain, favors the expression of the low-affinity stoichiometry of the α4β2 receptor $(\alpha4)_3(\beta2)_2$, reduces the firing frequency in dopaminergic neurons, and eliminates nicotine reward-related behavior.

In the Henderson, et al. 2016 study, a racemate of menthol was used, that is, a 50:50 mixture of the (–)- and (+)- enantiomers (Figure 5.1). Both the natural (–)-menthol and synthetic (±)-menthol, which is racemic and has different taste characteristics from the natural (–)-menthol, have been found in tobacco.[63] In new studies with colleague Brandon Henderson, we found that only the (–)-menthol contributes to the effects seen in chronic studies, whereas (+)-

menthol led to null effects. Thus, we investigated the biophysical characteristics of (–)-menthol versus (+)-menthol on the α4β2 receptor.

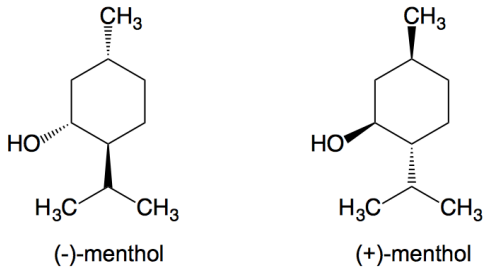

Figure 5.1. Chemical structure of (–)-menthol and (+)-menthol.

5.3 Results and Discussion

Hans, et al. has shown that menthol is a negative allosteric modulator. However, in this study, only the the (–)-enantiomer of menthol was studied. We examined the effect of (–)-menthol and (+)-menthol for both the the high-affinity $(\alpha4)_2(\beta2)_3$ and the low-affinity $(\alpha4)_3(\beta2)_2$ receptor in *Xenopus laevis* oocytes.

We first performed competition binding assays to investigate the negative allostery of menthol. When either (–)-menthol or (+)-menthol (50 μM) was co-applied with ACh, we observed an approximately 40% reduction in ACh-induced current amplitude – for both stoichiometries. ACh and menthol co-applications did not incur a marked change in the EC_{50} concentrations as compared to ACh-only induced activation (Figure 5.2 and Table 5.1). The maximum size of ACh-induced current ranged up to 1.05 μA and 13.6 μA with EC_{50} values of 0.61 ± 1.03 μM (n = 15) and 99.8 ± 1.0 μM (n = 19) for $(\alpha4)_2(\beta2)_3$ and $(\alpha4)_3(\beta2)_2$, respectively (Table 5.1). This reinforces the finding in Hans, et al. that (–)-menthol is a non-competitive binder that inhibits α4β2 receptor function and also further reveals that (+)-menthol non-competitively inhibits receptor function in a similar manner.

We further dissected the inhibitory effect of menthol into each stoichiometry of α4β2, namely the high-affinity $(\alpha4)_2(\beta2)_3$ and the low-affinity $(\alpha4)_3(\beta2)_2$. Menthol, both stereoisomers, had very similar dose-response curves and IC_{50} concentrations for ACh-induced activation for both $(\alpha4)_2(\beta2)_3$ and $(\alpha4)_3(\beta2)_2$ (Figure 5.3 and Table 5.2). Both IC_{50} experiments and the competition binding assays indicate that menthol does act directly on the α4β2 nAChR, and acute studies in *Xenopus* oocytes suggest that the two stereoisomers of menthol used in cigarettes, (–)-menthol and (+)-menthol, do not show favorability nor inhibitory differences on the receptor.

Findings in chronic studies by colleague Brandon Henderson showed stereoisomer effects on the receptor as well as menthol driving favorability towards the low-affinity receptor. These findings in conjunction with our acute studies suggest the possibility of multiple menthol binding sites. It is also possible that menthol acts on a secondary target that mediates the effects

as seen in the chronic studies. We sought to identify the binding sites for menthol on the α4β2 nAChR next, as described in the following chapter.

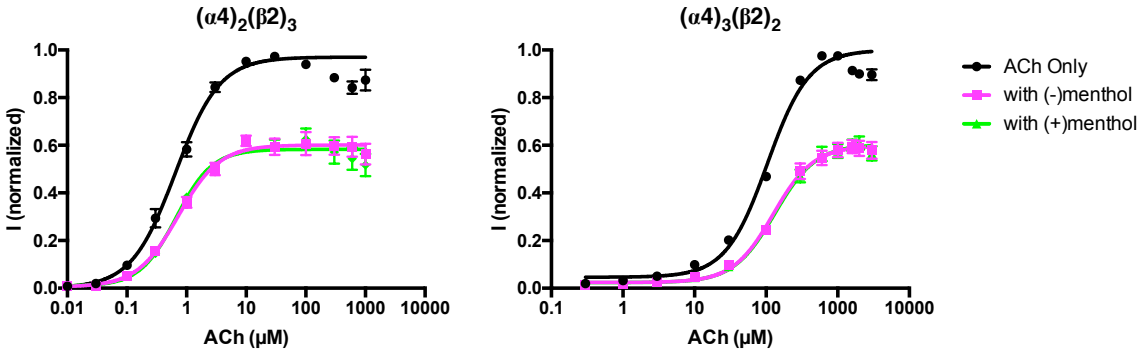

Figure 5.2. Concentration-response relationships of acetylcholine and of (–)-menthol and (+)-menthol in competition binding assays for $(\alpha4)_2(\beta2)_3$ and $(\alpha4)_3(\beta2)_2$. In the co-applications with ACh, 50 μM of menthol used. The maximum response from acetylcholine potentiation in the presence of either menthol stereoisomer is ~60% of the maximum response without menthol.

Receptor		n_H	EC_{50} (μM)	n	I_{max} (μA)
$(\alpha4)_2(\beta2)_3$	ACh Only	1.27 ± 0.05	0.61 ± 1.03	15	0.04 – 1.05
	with (–)-menthol	1.38 ± 0.08	0.66 ± 1.05	12	0.05 – 0.82
	with (+)-menthol	1.51 ± 0.10	0.64 ± 1.05	15	0.03 – 0.85
$(\alpha4)_3(\beta2)_2$	ACh Only	1.74 ± 0.07	99.8 ± 1.0	19	0.2 – 13.6
	with (–)-menthol	1.58 ± 0.04	120.8 ± 1.0	18	0.1 – 9.9
	with (+)-menthol	1.56 ± 0.04	126.4 ± 1.0	19	0.1 – 9.3

Table 5.1. Competition binding assays of menthol with acetylcholine potentiation of $(\alpha4)_2(\beta2)_3$ and $(\alpha4)_3(\beta2)_2$ nAChRs.

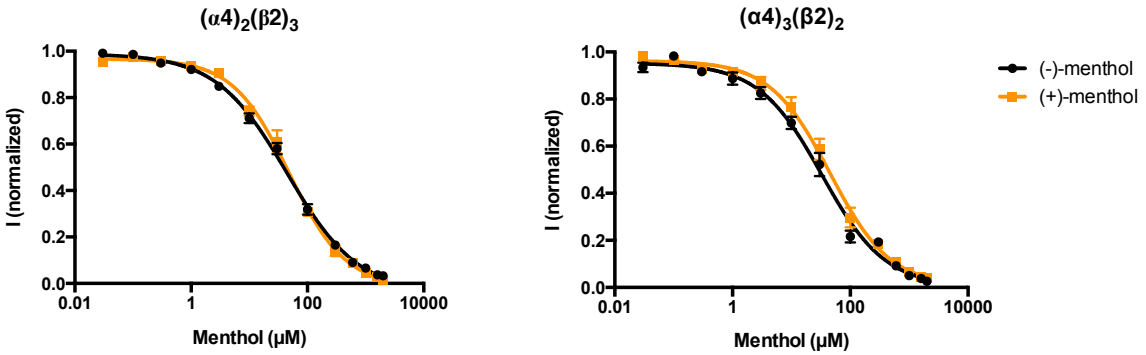

Figure 5.3. Menthol-IC50 curves. Concentration-response relationships of menthol for $(\alpha4)_2(\beta2)_3$ with 2 μM acetylcholine and for $(\alpha4)_3(\beta2)_2$ with 100 μM acetylcholine.

Receptor		n_H	IC_{50} (μM)	n	I_{max} (μA)
$(\alpha4)_2(\beta2)_3$	(–)-menthol	-0.71 ± 0.02	44.9 ± 1.04	10	0.08 – 1.34
	(+)-menthol	-0.90 ± 0.03	48.3 ± 1.04	10	0.12 – 0.97
$(\alpha4)_3(\beta2)_2$	(–)-menthol	-0.81 ± 0.03	33.1 ± 1.06	10	0.09 – 1.30
	(+)-menthol	-0.85 ± 0.03	45.5 ± 1.05	10	0.13 – 1.37

Table 5.2. Concentration-response relationships of menthol for $(\alpha4)_2(\beta2)_3$ with 2 μM acetylcholine and for $(\alpha4)_3(\beta2)_2$ with 100 μM acetylcholine.

5.4 Methods

5.4.1 Molecular Biology

The α4 and β2 subunits of rat nAChR are in the pGEM vector. The plasmid DNAs were linearized by *Not*I restriction digest. The mRNAs were prepared from linearized DNA, using a T7 mMessage mMachine kit (Ambion), and were purified with the RNeasy Mini kit (Qiagen). Concentration of mRNA was determined by absorption on the Nanodrop 2000 Spectrophotometer (Thermo Scientific).

5.4.2 Oocyte Preparation and Injection

Xenopus laevis stage V and VI oocytes were harvested and injected with mRNAs as previously described.[1] The α4 and β2 mRNAs were mixed in a 1:10 ratio by mass to obtain the $(\alpha4)_2(\beta2)_3$ or in a 10:1 ratio to obtain the $(\alpha4)_3(\beta2)_2$ receptor. For all studies for identifying a menthol binding site, a 10:1 ratio to obtain the $(\alpha4)_3(\beta2)_2$ receptor was used. A total of 50 nL of the mRNA mixture were injected into each oocyte, delivering a mRNA mass total of 22 ng. After injection, the oocytes were incubated at 18 °C in ND96 medium (96 mM NaCl, 2 mM KCl, 1 mM $MgCl_2$, 5 mM HEPES at pH 7.5) enriched with theophylline, sodium pyruvate, and gentamycin for 24h or 48 h before recording.

5.4.3 Chemical Preparation

Acetylcholine Cl (ACh) was purchased from Sigma-Aldrich and dissolved to 1 M stock solutions in ND96 Ca^{2+} free buffer (96 mM NaCl, 2 mM KCl, 1 mM $MgCl_2$, 5 mM HEPES at pH 7.5). (+)-menthol and (–)-menthol were purchased from Sigma-Aldrich and dissolved to 1 M stock solutions in methanol. All drug solutions contain less than 0.1% of methanol.

5.4.4 Electrophysiology

All electrophysiology recordings were made using the OpusXpress 6000A (Axon Instruments) in two-electrode voltage clamp mode at a holding potential of –60 mV. ND96 Ca^{2+} free solution was used as the running buffer. All drugs were applied as a 1 mL dose in ND96

Ca^{2+} free solution. All ACh-EC50 experiments used ACh doses applied over 15 seconds followed by a 2 min buffer wash at a rate of 3 mL min^{-1}.

For all menthol-IC50 experiments, first two doses of ACh at the EC_{50} concentration was applied to ensure proper current waveforms and receptor function. Subsequently, a menthol only dose was applied over 15 s followed by a 30 s buffer wash at a rate of 3 mL min^{-1}. A dose of menthol and ACh co-application was then applied over 15 s followed by a 5 min buffer wash at a rate of 3 mL min^{-1}. This was iterated for all concentration ranges of menthol with ACh at the ACh-EC_{50} concentration.

For all competition binding assays assays, an ACh dose was applied over 15 seconds followed by a 2 min buffer wash at a rate of 3 mL min^{-1}. Then, an ACh dose with 50 μM (–)-menthol was applied over 15 s followed by a 3.3 min buffer wash at a rate of 3 mL min^{-1}. Lastly, an ACh dose with 50 μM (+)-menthol was applied over 15 s followed by a 3.3 min buffer wash at a rate of 3 mL min^{-1}. This was iterated for all concentration ranges of ACh.

Data were sampled at 50 Hz and then low-pass filtered at 5 Hz.

5.4.5 Data Analysis

To assess the potency of ACh, concentration-response relationships for ACh were fitted using

$$I/I_{max} = 1 - [1/(1 + (EC_{50}/[A])^{n_H})\,]$$

where I/I_{max} is the relative current induced by varying concentrations of ACh ([A]). EC_{50} is the value of [ACh] that elicits a half-maximum response, and n_H is the Hill coefficient. For the competition binding assays, the drug applications of ACh and its co-application with (–)- or (+)-menthol were applied to the same cell, and the I_{max} of the largest ACh-induced current without menthol was for normalization.

To assess the potency of antagonism, inhibition-concentration relationships for menthol were fitted using

$$I/I_{max} = 1 - [1/(1 + (IC_{50}/[M])^{n_H})\ ]$$

where I/I_{max} is the relative current induced by ACh in the presence of varying concentrations of menthol ([M]). IC_{50} is the value of [menthol] that elicits a half-maximum response, and n_H is the Hill coefficient.

The concentration-response relationships for each cell were fitted to one Hill term to generate EC_{50}, IC_{50}, and Hill coefficient (n_H) values using GraphPad Prism. Error bars represent the standard error of the mean (SEM) values.

Uninjected cells can occasionally give current responses up to ~200 nA. Only cells that gave responses larger than ~200 nA were reported, and other cells were reported as non-responsive (NR).

Chapter 6

IDENTIFICATION OF A MENTHOL BINDING SITE ON α4β2 NACHRS

6.1 Abstract

The binding pocket, site, and mode of menthol binding to the α4β2 receptor is currently unknown. We hypothesize that menthol binds in the TMD. Computational docking studies show multiple menthol binding sites intra- and inter-subunit in the TMD of the human α4β2 nAChR. Initial attempts to experimentally find the binding site(s) have been made. Single mutations have either led to nonfunctional receptors or small changes in the $IC_{50,}$ indicating minor changes to menthol binding. There is a possibility that several residues together contribute to menthol binding and may induce a larger, i.e. more meaningful, shift in the IC_{50}. We can continue to probe these sites by performing double or triple mutations.

6.2 Introduction

Menthol is not only interesting from a drug addiction standpoint but also a biophysical standpoint. It is a negative allosteric modulator of the $\alpha4\beta2$ nAChR[64], but the binding mode of menthol to $\alpha4\beta2$ nAChR is currently unknown. Some hypothesized that menthol inhibits function by favoring the desensitized state.[65] The effective inhibitory concentration of menthol on $\alpha4\beta2$ nAChRs (IC_{50}) found in acute studies is 33 μM (present work) or 111 μM[64], which is likely higher than the concentrations found *in vivo*. In chronic studies, nanomolar concentration ranges are used. The order of magnitude difference in effective concentrations between acute and chronic studies suggest the possibility of multiple binding sites. Many general anesthetics that menthol is similar to in chemical structure and size have multiple binding sites in the TMD of LGICs.

Targeting the General Anesthetics (Propofol) Binding Site

Based its structural and chemical similarity to general anesthetics, we hypothesize that menthol's binding mode is similar to that of general anesthetics. General anesthetics are a class of drugs that induce a reversible loss of consciousness in humans by targeting the neuronal pathway. There are two theories for their mode of action. Early research supported the theory that the drugs act in a nonspecific manner, disordering and increasing the fluidity of the lipid membrane. Accumulating evidence indicates that they directly interact with ion channels in the central nervous system via an allosteric mechanism.[66]

General anesthetics can either potentiate or inhibit the ion channel. Most anesthetics inhibit cationic Cys-loop LGICs (e.g. nAChR and 5HT3) but potentiate anionic Cys-loop LGICs (e.g. $GABA_AR$ and GlyR). The binding affinity also varies for each receptor and to different states (e.g. open, closed, and desensitized). Many studies revealed binding sites for these molecules on Cys-loop receptors to be intra- and/or inter-subunit in the TMD (Figure 6.1).

Menthol is chemically and structurally similar to Propofol (Diprivan), an anesthetic that slows brain and nervous system activity, causing sleepiness and relaxation before and during medical procedures such as surgery. A number of studies have revealed specific Propofol

binding sites on $GABA_AR$ and GLIC, a bacterial homolog of vertebrate Cys-loop LGICs, in the intra- and inter-subunit region of the TMD (Figure 6.1). We hypothesize that menthol may bind to the human α4β2 nAChR at sites analogous to the Propofol binding sites. We use these sites as a guide for analyzing computational docking results and selecting residues to experimentally screen.

Computational Docking

A 3.9 Å X-ray crystal structure of the human α4β2 nAChR was reported recently in October 2016, revealing structural details of the ECD and TMD.[10] Prior to this, mostly homology models of the α4β2 ECD based on the acetylcholine binding protein (AChBP) have been used in computational studies (e.g. docking and MD) to identify and study drug binding sites. One limitation is that homology models may not be very accurate although many binding sites have been accurately revealed with them. The major limitation of the model is that drug binding studies are limited to drugs that bind to the ECD only and not the TMD or ICD. This is particularly important for many allosteric drugs, namely general anesthetics and Propofol, as they are known to bind to the TMD. The recent crystal structure of human α4β2 nAChR provides a more reliable protein model for computational studies in identifying drug binding sites, particularly in the TMD. Computational docking allows identification of binding pockets and understanding of binding modes. Molecular dynamics allows deeper investigation of binding interactions.

In this chapter, we describe our efforts in identifying the residues involved in menthol binding using computational modeling and docking and experimental mutagenesis screening.

6.3 Results and Discussion

Computational Docking

To predict which pockets menthol binds to in the α4β2 receptor, we employ computational docking using AutoDock VINA. We dock the chair conformation of (–)-menthol to three conformational snapshots of the human α4β2 protein model. At 0 ns, the protein is likely in the desensitized state. At 2.5 and 100 ns, conformational space is sampled, but the conformations are unlikely to be representative of a different receptor state, e.g. the open state, as this transition takes place on a longer timescale. Building the protein model and performing the conformational sampling are described in Appendix 1.

We dock menthol to the whole protein (blind docking) and focus the docking to the TMD (refined docking) by refining the search box (Figure 6.2). The results show binding sites in the agonist site, near the Cys loop, in the channel pore, in the intra-subunit cavity, and less so in the interfacial cavity. We compare these results to the Propofol binding sites to select residues to experimentally screen (Figure 6.3).

Experimental Screening via Mutagenesis of Target Residues

The human α4β2 protein model is used in all computational studies, while the rat α4β2 protein is expressed in oocytes in the experimental mutagenesis studies. The protein sequence identity between the α4 subunit from rat (*Rattus norvegicus*) and from human (*Homo sapien*) is 83.07% and for the β2 subunit is 93.23%. This sequence identity is high enough to reasonably use the rat protein in experimental studies to inform the human model. Also, the residues selected for testing are in the same in the rat and human protein sequence (Figure 6.4 and 6.5).

Menthol does not bind in the native agonist site

Menthol is known to be a negative allosteric modulator to the α4β2 nAChR. Although it is unlikely that menthol binds in the native agonist site, we tested this pocket anyways based on the blind docking study, revealing a potential menthol binding in the agonist pocket (Figure

6.2). A prior study conducted by Chris Marotta in the Dougherty lab weakly suggested that menthol may bind here as well. He showed a weak IC_{50} fold-shift with mutations H144V, Q152F, and T154L on the α4 subunit. We repeated this study to verify the effects. The α4-H144V, Q152F, and T154L mutation impacted the EC_{50} by a fold-shift of 0.74 (Figure 6.6 and Table 6.1). The IC_{50} of the wildtype and this mutant differ by only a factor of 2 (Table 6.2), indicating that menthol unlikely binds at the agonist site, as previous studies have already suggested. Thus, we continue probing other pockets of the protein.

Menthol does not bind in a pocket near the Cys-loop

Docking studies also revealed a potential binding site near the Cys loop (Figure 6.2 and 6.3). Analyzing this pocket, we hypothesized that menthol may form a hydrogen bond with nearby residues. We analyzed the orientation of the docking poses and selected electrically charged residues that were within a 2-4 Å proximity to the hydroxyl group of menthol. Six residues were selected for screening. α4-E182, α4-DE51, and α4-Q55 were mutated to alanines and resulted in non-functional receptors, i.e., no ACh-induced current response. Smaller perturbations, α4-E52L, α4-E182Q, and β2-S44A, led to functional receptors and resulted in IC_{50} fold shifts of 0.7, 0.73, and 1.82, respectively (Figure 6.7 and Table 6.2). Fold-shifts less than 2 suggests that these mutations do make large individual contributions to menthol binding.

Intra-subunit in the TMD

A highly probable pocket for menthol binding would be near the general anesthetic binding sites, i.e., within the intra- and inter-subunit cavity formed by the M1 to M4 helices in the TMD. Docking studies also showed menthol poses in this region (Figure 6.2). In this pocket, hydrophobic interactions seem to dominate binding. We identified and tested residues, which were mostly hydrophobic and neighbored docked states of menthol within 5 Å (Figure 6.2 and 6.3).

Twelve residues were identified in the intra-subunit region on the M1 and M3 helices in the TMD of the α4 subunit, of which half led to no ACh-induced current response. All the intra-subunit mutations, with the exception of α4-G281, which is on the M3 helix and faces the M2

helix, faced the center of the M1 and M3 helices. Mutations of all the residues that led to no responses, with the exception of α4-G281, were in the upper region of the M1 and M3 helices. Meanwhile, mutations that led to responses and thus were subsequently characterized were in the lower region of the helices. α4-G281F and α4-G281A mutations notably led to a gain of function by 3.5 and 7.7 in the EC_{50} (Table 6.1). The α4-G281F mutation showed the highest loss of function by 3.27 in IC_{50}, but a 3-fold change is not significant enough to suggest this as a menthol binding site (Figure 6.8 and Table 6.2).

The upper region of the cavity formed by the M1 and M3 helices on the GABA and GLIC receptors is where Propofol binds. Based on our hypothesis that menthol is likely to bind in this region as well, we are unable to test this because mutations in this region led to non-responsive receptors. We can make even smaller mutagenic perturbations, but that runs the risk of small IC_{50} fold shifts. We can also perform molecular dynamic (MD) simulations and observe the stability of menthol binding in this pocket over time.

Inter-subunit in the TMD

We also probed the inter-subunit region between the α4 and β2 subunits in the TMD. The two residues that retained ACh-induced current response, α4-F286A and β2-I218A, had less than a 2-fold loss of in IC_{50} (1.64 and 1.85 fold-shift), which suggests that menthol does not bind strongly to these residues (Figure 6.9 and Table 6.2). The two other residues that led to non-responsive receptors were also near the top of the M3 (α4 subunit) and M1 (β2 subunit) helices. We further tested an interfacial pocket by combining the α4-G281A and β2-I218A mutations, and the resulting IC_{50} fold-shift (0.72) was even lower than the individual mutations themselves (Figure 6.10 and Table 6.2). This may be because mutating a glycine to the larger residue alanine fills the cavity, while an isoleucine to the smaller residue alanine compensates for the other mutation.

Channel Pore

α4-L265 and β2-L257 both line the pore, so mutations to these residues could test if menthol inhibits by being a channel blocker. A β2-L257A mutation led to a 500 fold gain of

ACh-induced function, EC_{50} (Figure 6.9 and Table 6.1). Neither mutation induced a fold shift larger than 2 in the IC_{50} value, suggesting that menthol may not be a channel blocker by interacting with these residues (Figure 6.9 and Table 6.2). Other sites that line the pore can be tested as well.

6.4 Conclusions

In conclusion, a specific binding site has not been identified. Nonetheless, the data for menthol on α4β2 receptors and its allosteric, non-competitive nature strongly suggests that menthol does bind to the receptor. The insurmountable non-competitive inhibition as observed in the studies described in Chapter 5 and by Hans, et al. has never been found to be an off-target effect. Most mutations that were screened for menthol binding showed less than a 2-fold shift in IC_{50} in dose response experiments with menthol. These results suggest that none of the mutations singly have a large contribution to menthol binding. A larger set of a combination of mutations could be tested next, as multiple residues could be required for menthol binding.

It is uncertain where menthol binds on the protein. Much of our approach thus far has been based on the binding modes of another drug (Propofol) and computational docking. We could narrow our search space by performing photoaffinity labeling experiments with menthol, as this technique has been exhaustively applied for identifying the binding pockets of many allosteric drugs in the past, including Propofol.

6.5 Methods

Oocyte preparation and injection, chemical preparation, electrophysiology, and data analysis is described in Chapter 5 Experimental Methods.

6.5.1 Computational Modeling and Docking

We built a human α4β2 receptor model based on the published X-ray crystal structure (PDB ID: 5kxi), in which missing residues were modeled and the whole protein was equilibrated in a solvated and lipid membrane system (Appendix 1). Docking of (–)-menthol to the whole protein model (blind docking) and then to the TMD of the model (refined docking) was performed using AutoDock VINA. The search volume was a 100 by 100 by 100 Å box to include the whole protein (blind docking) and a 100 by 100 by 70 Å box to include only the TMD (refined docking). The chair conformation of (–)-menthol was used. All waters and ions were removed from the structures prior to docking. All hydrogen atoms and partial charges were also added, and nonpolar hydrogens were merged. 100 poses of menthol were generated per docking run.

6.5.2 Construct Preparation

All mutant constructs were prepared by QuikChange mutagenesis on the respective subunits. The mutation was verified by sequencing (Laragen). The α4 and β2 subunits of rat nAChR are in the pGEM vector. The plasmid DNAs were linearized by *Not*I restriction digest. The mRNAs were prepared from linearized DNA, using a T7 mMessage mMachine kit (Ambion), and were purified with the RNeasy Mini kit (Qiagen). Concentration of mRNA was determined by absorption on the Nanodrop 2000 Spectrophotometer (Thermo Scientific).

6.6 Figures

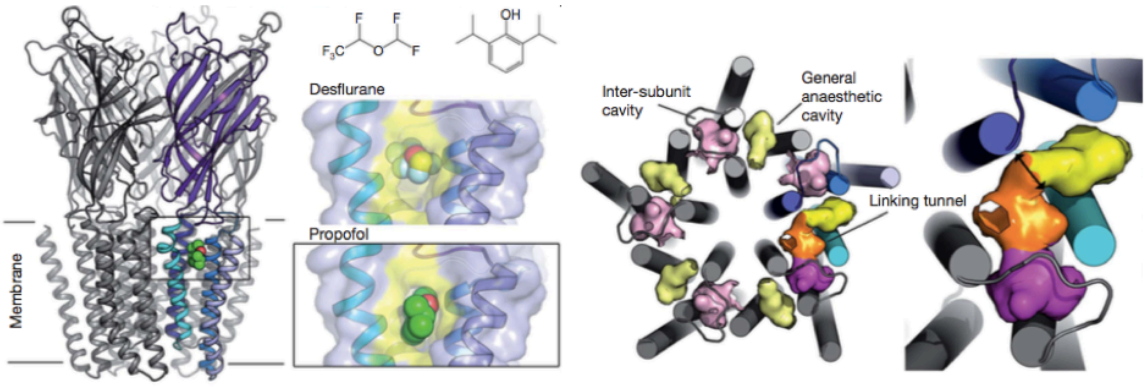

Figure 6.1. Intra- and inter-subunit binding sites for Propofol and general anesthetics on GLIC. Figure taken from Nury, et al.[67]

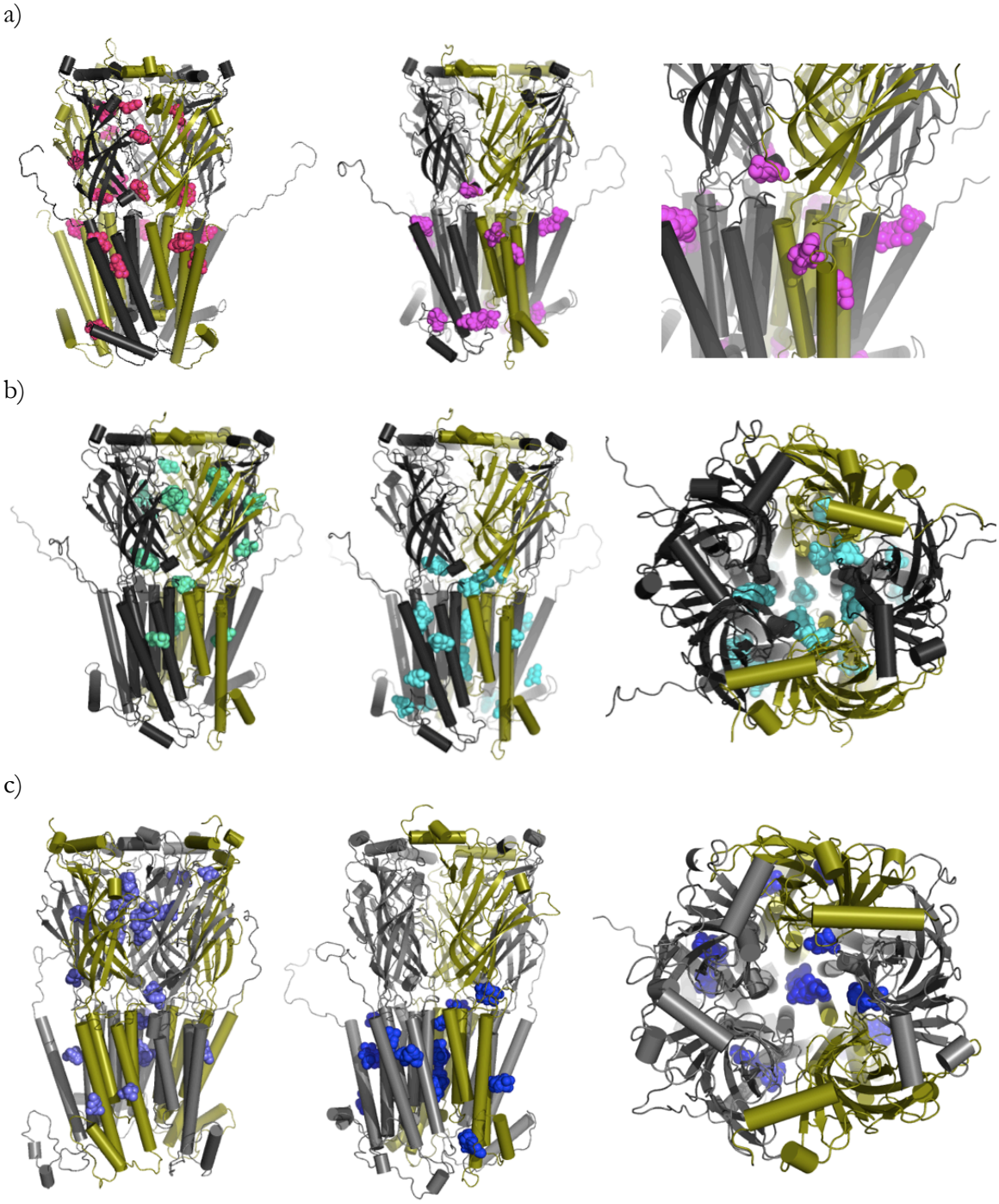

Figure 6.2. Menthol binding sites. Blind (left) and refined (TMD) docking (middle and right) of human α4β2 nAChR, shown in cartoon representation. α4 subunit colored in deep olive. β2 subunit colored in gray. Menthol shown as spheres in various colors. Conformational snapshots taken from molecular dynamic (MD) simulations at a) 0 ns, b) 2.5 ns, and c) 100 ns (Appendix 1). Shown are 100 states of menthol per docking run.

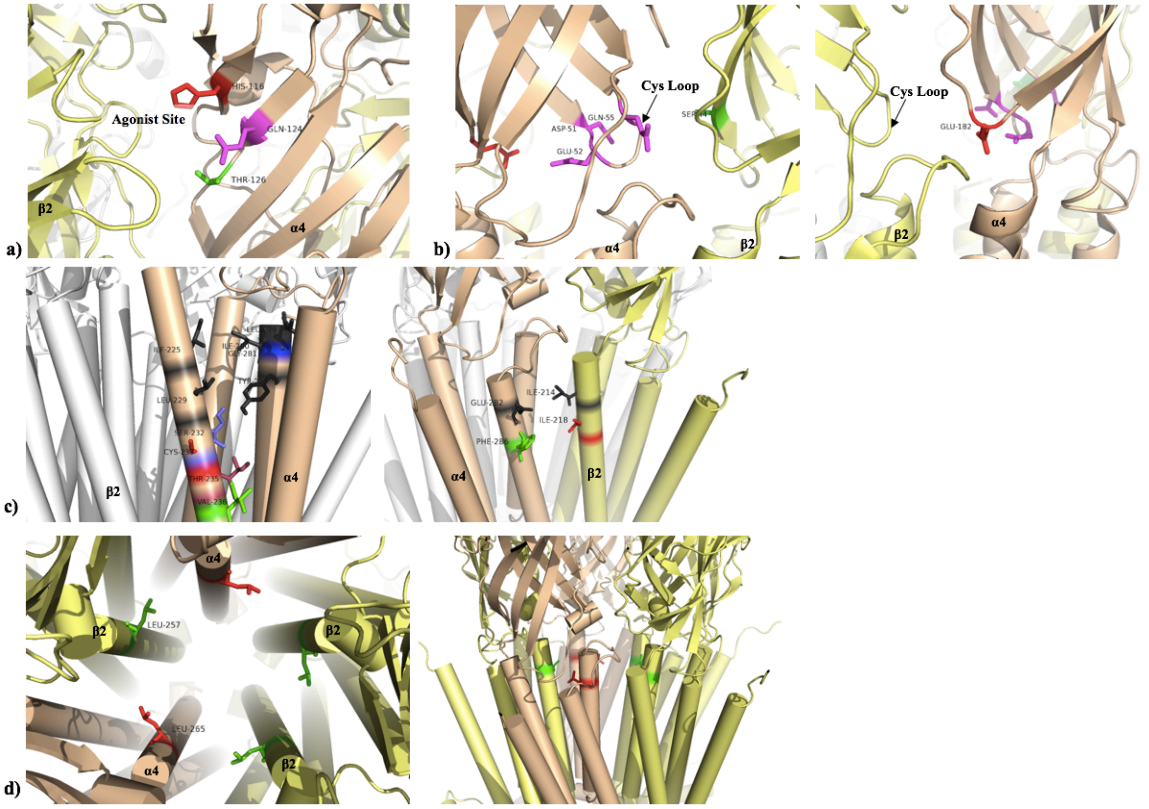

Figure 6.3. Residues selected for experimental mutagenesis screening in a) the agonist site, b) near the Cys loop on both the α4-β2 interface and β2-α4 interface, c) the intra-subunit cavity of the α4 subunit, and d) the channel pore. Residues shown as black are mutations that led to non-responsive receptors to ACh activation.

```
α7_HUMAN EFQRKLYKELVKNYNPLERPVANDSQPLTVYFSLSLLQIMDVDEKNQVLTTNIWLQMSWT 83
α4_HUMAN HAEERLLKKLFSGYNKWSRPVANISDVVLVRFGLSIAQLIDVDEKNQMMTTNVWVKQEWH 94
α3_HUMAN EAEHRLFERLFEDYNEIIRPVANVSDPVIIHFEVSMSQLVKVDEVNQIMETNLWLKQIWN 92
α4_MOUSE HAEERLLKRLFSGYNKWSRPVANISDVVLVRFGLSIAQLIDVDEKNQMMTTNVWVKQEWH 96
α4_RAT   HAEERLLKRLFSGYNKWSRPVANISDVVLVRFGLSIAQLIDVDEKNQMMTTNVWVKQEWH 96
α3_RAT   EAEHRLFQYLFEDYNEIIRPVANVSHPVIIQFEVSMSQLVKVDEVNQIMETNLWLKQIWN 86
α2_HUMAN ETEDRLFKHLFRGYNRWARPVPNTSDVVIVRFGLSIAQLIDVDEKNQMMTTNVWLKQEWS 116
α3_MOUSE EAEHRLFQYLFEDYNEIIRPVANVSHPVIIQFEVSMSQLVKVDEVNQIMETNLWLKQIWN 86
α6_HUMAN ATEERLFHKLFSHYNQFIRPVENVSDPVTVHFEVAITQLANVDEVNQIMETNLWLRHIWN 91
α2_RAT   HAEDRLFKHLFGGYNRWARPVPNTSDVVIVRFGLSIAQLIDVDEKNQMMTTNVWLKQEWN 93
           : :* . *.  **   *** * *. : : * ::: *: .*** **:: **:*::  *

α7_HUMAN DHYLQWNVSEYPGVKTVRFPDGQIWKPDILLYNSADERFDATFHTNVLVNSSGHCQYLPP 143
α4_HUMAN DYKLRWDPADYENVTSIRIPSELIWRPDIVLYNNADGDFAVTHLTKAHLFHDGRVQWTPP 154
α3_HUMAN DYKLKWNPSDYGGAEFMRVPAQKIWKPDIVLYNNAVGDFQVDDKTKALLKYTGEVTWIPP 152
α4_MOUSE DYKLRWDPGDYENVTSIRIPSELIWRPDIVLYNNADGDFAVTHLTKAHLFYDGRVQWTPP 156
α4_RAT   DYKLRWDPGDYENVTSIRIPSELIWRPDIVLYNNADGDFAVTHLTKAHLFYDGRVQWTPP 156
α3_RAT   DYKLKWKPSDYQGVEFMRVPAEKIWKPDIVLYNNADGDFQVDDKTKALLKYTGEVTWIPP 146
α2_HUMAN DYKLRWNPTDFGNITSLRVPSEMIWIPDIVLYNNADGEFAVTHMTKAHLFSTGTVHWVPP 176
α3_MOUSE DYKLKWKPSDYQGVEFMRVPAEKIWKPDIVLYNNADGDFQVDDKTKALLKYTGEVTWIPP 146
α6_HUMAN DYKLRWDPMEYDGIETLRVPADKIWKPDIVLYNNAVGDFQVEGKTKALLKYNGMITWTPP 151
α2_RAT   DYKLRWDPAEFGNVTSLRVPSEMIWIPDIVLYNNADGEFAVTHMTKAHLFFTGTVHWVPP 153
         *: *:*.  :: .   :*.*   ** ***:***.*   * .   *:. :   *   : **

α7_HUMAN GIFKSSCYIDVRWFPFDVQHCKLKFGSWSYGGWSLDLQMQ--EADISGYIPNGEWDLVGI 201
α4_HUMAN AIYKSSCSIDVTFFPFDQQNCTMKFGSWTYDKAKIDLVNMHSRVDQLDFWESGEWVIVDA 214
α3_HUMAN AIFKSSCKIDVTYFPFDYQNCTMKFGSWSYDKAKIDLVLIGSSMNLKDYWESGEWAIIKA 212
α4_MOUSE AIYKSSCSIDVTFFPFDQQNCTMKFGSWTYDKAKIDLVSMHSRVDQLDFWESGEWVIVDA 216
α4_RAT   AIYKSSCSIDVTFFPFDQQNCTMKFGSWTYDKAKIDLVSMHSRVDQLDFWESGEWVIVDA 216
α3_RAT   AIFKSSCKIDVTYFPFDYQNCTMKFGSWSYDKAKIDLVLIGSSMNLKDYWESGEWAIIKA 206
α2_HUMAN AIYKSSCSIDVTFFPFDQQNCKMKFGSWTYDKAKIDLEQMEQTVDLKDYWESGEWAIVNA 236
α3_MOUSE AIFKSSCKIDVTYFPFDYQNCTMKFGSWSYDKAKIDLVLIGSSMNLKDYWESGEWAIIKA 206
α6_HUMAN AIFKSSCPMDITFFPFDHQNCSLKFGSWTYDKAEIDLLIIGSKVDMNDFWENSEWEIIDA 211
α2_RAT   AIYKSSCSIDVTFFPFDQQNCKMKFGSWTYDKAKIDLEQMERTVDLKDYWESGEWAIINA 213
         .*:**** :*: :**** *:*.:*****:*.  .:**       :  .:  ..** ::

α7_HUMAN PGKRSERFYECCKEPYPDVTFTVTMRRRTLYYGLNLLIPCVLISALALLVFLLPADSGEK 261
α4_HUMAN VGTYNTRKYECCAEIYPDITYAFVIRRLPLFYTINLIIPCLLISCLTVLVFYLPSECGEK 274
α3_HUMAN PGYKHDIKYNCCEEIYPDITYSLYIRRLPLFYTINLIIPCLLISFLTVLVFYLPSDCGEK 272
α4_MOUSE VGTYNTRKYECCAEIYPDITYAFIIRRLPLFYTINLIIPCLLISCLTVLVFYLPSECGEK 276
α4_RAT   VGTYNTRKYECCAEIYPDITYAFIIRRLPLFYTINLIIPCLLISCLTVLVFYLPSECGEK 276
α3_RAT   PGYKHEIKYNCCEEIYQDITYSLYIRRLPLFYTINLIIPCLLISFLTVLVFYLPSDCGEK 266
α2_HUMAN TGTYNSKKYDCCAEIYPDVTYAFVIRRLPLFYTINLIIPCLLISCLTVLVFYLPSDCGEK 296
α3_MOUSE PGYKHEIKYNCCEEIYQDITYSLYIRRLPLFYTINLIIPCLLISFLTVLVFYLPSDCGEK 266
α6_HUMAN SGYKHDIKYNCCEEIYTDITYSFYIRRLPMFYTINLIIPCLFISFLTVLVFYLPSDCGEK 271
α2_RAT   TGTYNSKKYDCCAEIYPDVTYYFVIRRLPLFYTINLIIPCLLISCLTVLVFYLPSECGEK 273
          *      *:** * * *:*: . :**  ::* :**:***::** *::*** **::.***

α7_HUMAN ISLGITVLLSLTVFMLLVAEIMPA-TSDSVPLIAQYFASTMIIVGLSVVVTVIVLQYHHH 320
α4_HUMAN ITLCISVLLSLTVFLLLITEIIPS-TSLVIPLIGEYLLFTMIFVTLSIVITVFVLNVHHR 333
α3_HUMAN VTLCISVLLSLTVFLLVITETIPS-TSLVIPLIGEYLLFTMIFVTLSIVITVFVLNVHYR 331
α4_MOUSE VTLCISVLLSLTVFLLLITEIIPS-TSLVIPLIGEYLLFTMIFVTLSIVITVFVLNVHHR 335
α4_RAT   VTLCISVLLSLTVFLLLITEIIPSPTSLVIPLIGEYLLFTMIFVTLSIVITVFVLNVHHR 336
α3_RAT   VTLCISVLLSLTVFLLVITETIPS-TSLVIPLIGEYLLFTMIFVTLSIVITVFVLNVHYR 325
α2_HUMAN ITLCISVLLSLTVFLLLITEIIPS-TSLVIPLIGEYLLFTMIFVTLSIVITVFVLNVHHR 355
α3_MOUSE VTLCISVLLSLTVFLLVITETIPS-TSLVIPLIGEYLLFTMIFVTLSIVITVFVLNVHYR 325
α6_HUMAN VTLCISVLLSLTVFLLVITETIPS-TSLVVPLVGEYLLFTMIFVTLSIVVTVFVLNIHYR 330
α2_RAT   ITLCISVLLSLTVFLLLITEIIPS-TSLVIPLIGEYLLFTMIFVTLSIVITVFVLNVHHR 332
         ::* *:*********:*:::* :*: **  :**:.:*:  ***:* **:*:**:**: *::
```

Figure 6.4. Sequence alignment using CLUSTALO of α subunits from various species. Highlighted in gray are the residues in the agonist pocket that were experimentally tested; yellow are residues near the Cys-loop; cyan are the intra-subunit residues; magenta are the interfacial residues; green is the channel pore. Sequences are truncated, showing only rows containing target residues.

```
β2_MOUSE MVSLAQLISVHEREQIMTTNVWLTQEWEDYRLTWKPEDFDNMKKVRLPSKHIWLPDVVLY 120
β2_HUMAN MVSLAQLISVHEREQIMTTNVWLTQEWEDYRLTWKPEEFDNMKKVRLPSKHIWLPDVVLY 120
β2_RAT   MVSLAQLISVHEREQIMTTNVWLTQEWEDYRLTWKPEDFDNMKKVRLPSKHIWLPDVVLY 119
         ************************************:**********************

β2_MOUSE TEIDLVLKSDVASLDDFTPSGEWDIIALPGRRNENPDDSTYVDITYDFIIRRKPLFYTIN 240
β2_HUMAN TEIDLVLKSEVASLDDFTPSGEWDIVALPGRRNENPDDSTYVDITYDFIIRRKPLFYTIN 240
β2_RAT   TEIDLVLKSDVASLDDFTPSGEWDIIALPGRRNENPDDSTYVDITYDFIIRRKPLFYTIN 239
         *********:***************:**********************************

β2_MOUSE LIIPCVLITSLAILVFYLPSDCGEKMTLCISVLLALTVFLLIISKIVPPTSLDVPLVGKY 300
β2_HUMAN LIIPCVLITSLAILVFYLPSDCGEKMTLCISVLLALTVFLLIISKIVPPTSLDVPLVGKY 300
β2_RAT   LIIPCVLITSLAILVFYLPSDCGEKMTLCISVLLALTVFLLIISKIVPPTSLDVPLVGKY 299
         ************************************************************
```

Figure 6.5. Sequence alignment using CLUSTALO of β subunits from various species. Highlighted in yellow are the residues near the Cys-loop that were experimentally tested; magenta are the interfacial residues; green is the channel pore. Sequences are truncated, showing only rows containing target residues.

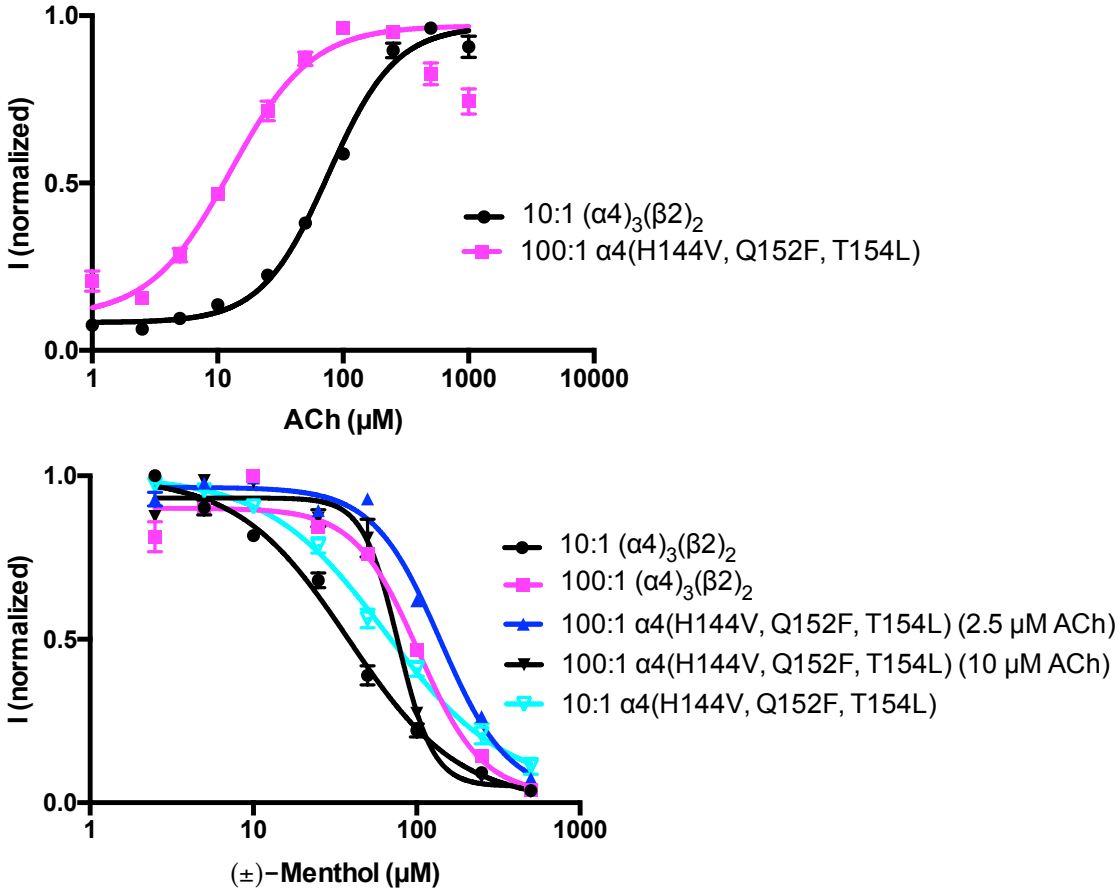

Figure 6.6. Dose-response curves for mutations at the agonist site and wild type.

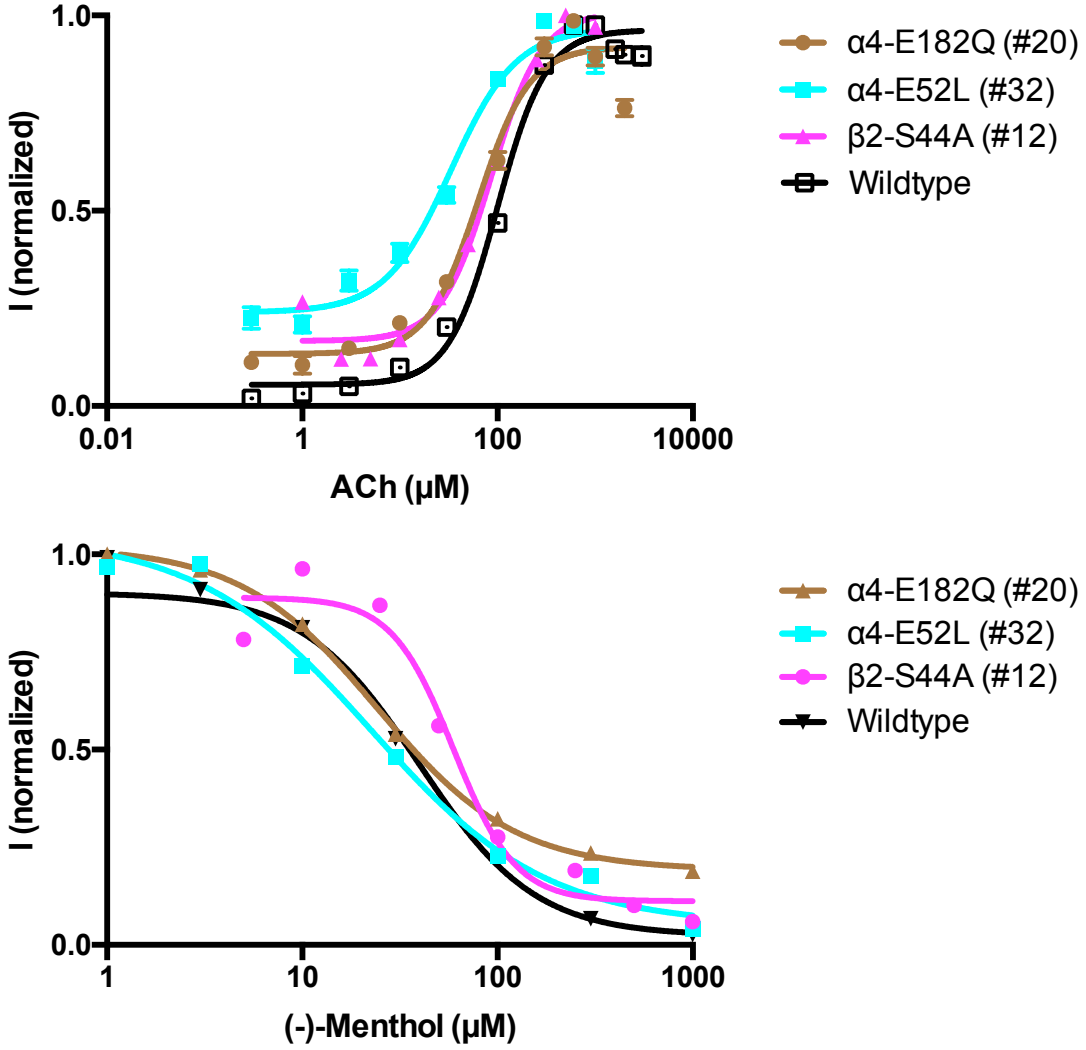

Figure 6.7. Dose-response curves for mutations at the Cys loop site and wild type. Number in parenthesis is the mutation code linked to laboratory notebooks and data.

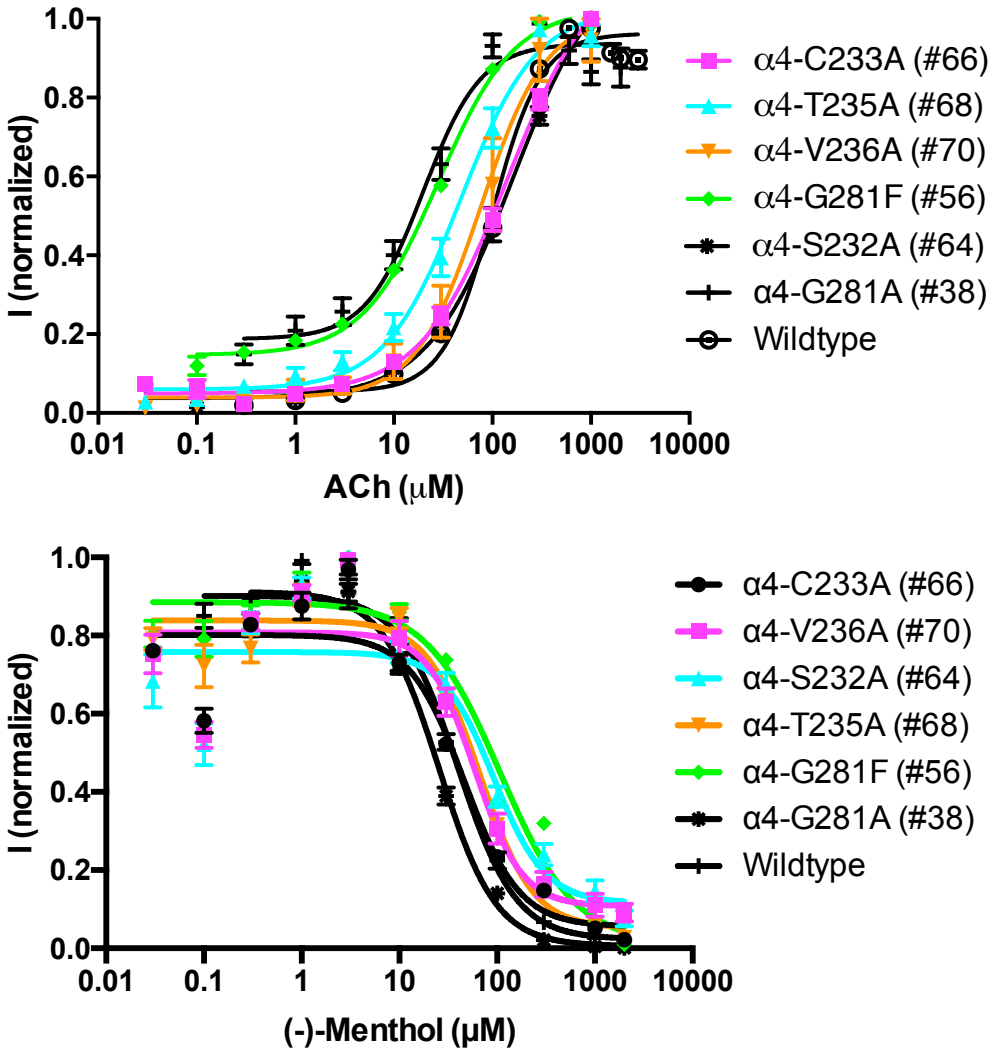

Figure 6.8. Dose-response curves for mutations in the intra-subunit cavity of α4 subunit and wild type. Number in parenthesis is the mutation code linked to laboratory notebooks and data.

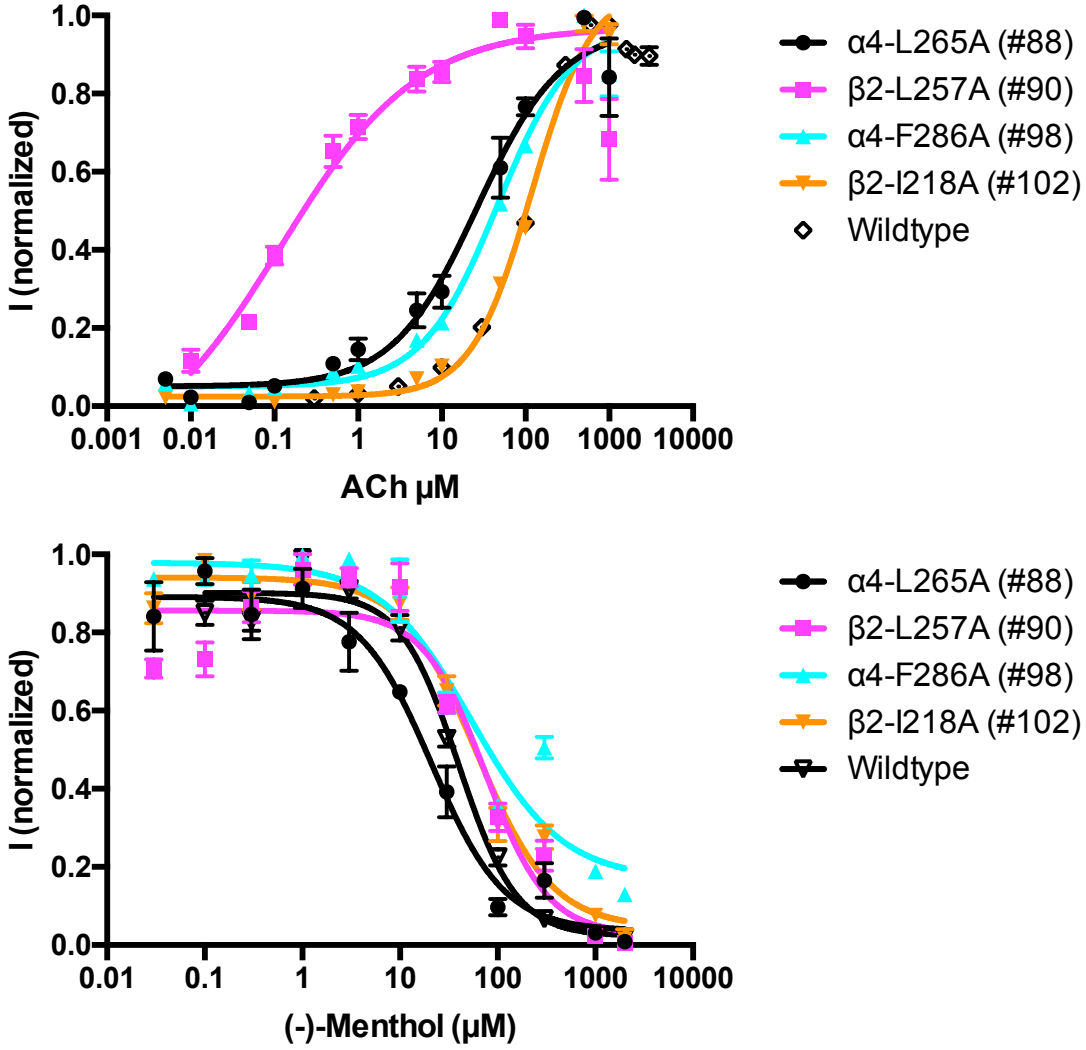

Figure 6.9. Dose-response curves for mutations in the inter-subunit cavity formed by the α4-β2 interface and wild type. Number in parenthesis is the mutation code linked to laboratory notebooks and data.

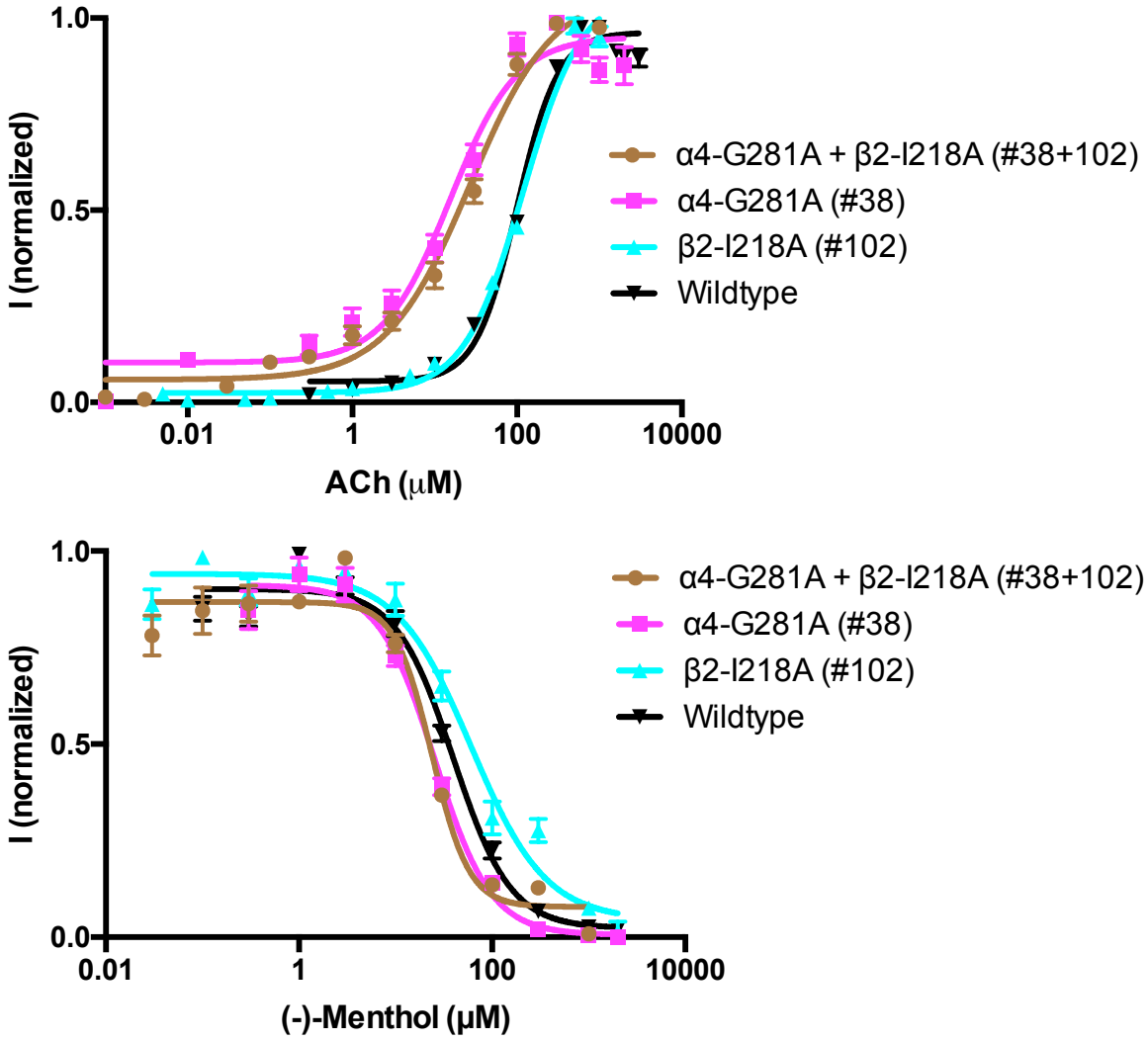

Figure 6.10. Dose-response curves for a double mutation as well as the single mutations in the inter-subunit cavity formed by the α4-β2 interface and wild type. Number in parenthesis is the mutation code linked to laboratory notebooks and data.

Table 6.1: Dose-response values for ACh

	EC_{50} (μM)	$\lvert I_{max} \rvert$ (μA)	n_H	N	Fold
Wild type	99.8 ± 1.00	0.2 – 13.6	1.74 ± 0.07	19	
Agonist Site					
α4-H144V, Q152F, T154L	72.2 ± 1.1	1.4 – 5.3	1.26 ± 0.12	12	0.72
Near Cys Loop					
α4-E52L	33.3 ± 1.08	1.0 – 12.5	1.3 ± 0.13	7	0.33
α4-E182Q	63.5 ± 1.07	0.006 – 0.35	1.6 ± 0.16	8	0.64
β2-S44A	86.1 ± 1.1	0.4 – 0.6	1.7 ± 0.25	2	0.86
α4-E182A	NR			8	
α4-DE51AA	NR			8	
α4-Q55A	NR			8	
Intra-subunit					
α4-C233A	143.4 ± 1.06	1.3 – 9.3	0.99 ± 0.04	6	1.43
α4-T235A	47.72 ± 1.08	1.0 – 4.8	1.13 ± 0.08	5	0.48
α4-V236A	76.23 ± 1.15	0.2 – 2.3	1.31 ± 0.20	2	0.76
α4-G281F	28.24 ± 1.07	0.4 – 1.5	1.13 ± 0.08	2	0.28
α4-S232A	162 ± 1.09	0.1 – 0.2	0.99 ± 0.05	4	1.62
α4-G281A	13.3 ± 1.17	1.6 – 17.1	0.87 ± 0.11	6	0.13
α4-I280A	NR			8	
α4-I225A	NR			8	
α4-L279A	NR			8	
α4-Y283A	NR			8	
α4-L229A	NR			8	
α4-G281W	NR			8	
Inter-subunit					
α4-F286A	46.5 ± 1.2	0.18 – 0.45	1.0 ± 0.1	2	0.47
β2-I218A	118.6 ± 1.1	0.59 – 2	2.2 ± 0.1	3	1.19
α4-E282D	NR			4	
α4-E282A	NR			4	
β2-I214A	NR			4	
α4-G281A + β2-I218A	26.6 ± 1.1	0.22 – 9.6	0.86 ± 0.06	6	0.26
Channel Pore					
α4-L265A	26.5 ± 1.3	0.24 – 3.26	0.9 ± 0.2	3	0.27
β2-L257A	0.2 ± 1.4	3.37 – 10.1	1.0 ± 0.3	4	0.002

Table 6.2: Dose-response values for (–)-menthol

	IC_{50} (uM)	$\lvert I_{max} \rvert$ (μA)	n_H	N	Fold
Wild type	33.1 ± 1.06	0.09 – 1.30	-0.81 ± 0.03	10	
Agonist Site					
α4-H144V, Q152F, T154L	64.42 ± 1.03	0.14 – 1.7	-1.20 ± 0.05	15	1.94
Near Cys Loop					
α4-E52L	22.7 ± 1.15	0.04 – 0.26	-0.97 ± 0.14	6	0.70
α4-E182Q	24.3 ± 1.18	0.02 – 0.07	-1.23 ± 0.25	3	0.73
β2-S44A	59.6 ± 1.05	0.14 – 1.18	-2.9 ± 0.34	8	1.82
Intra-subunit					
α4-C233A	46.08 ± 1.13	1.2 – 8.6	-1.53 ± 0.24	8	1.39
α4-T235A	66.57 ± 1.09	0.6 – 5.4	-1.60 ± 0.19	8	2.03
α4-V236A	58.86 ± 1.15	0.1 – 0.7	-1.79 ± 0.34	8	1.79
α4-G281F	107.5 ± 1.17	0.1 – 0.7	-1.14 ± 0.18	5	3.27
α4-S232A	91.95 ± 1.27	0.04 – 0.4	-1.63 ± 0.58	5	2.76
α4-G281A	41.9 ± 1.12	0.93 – 19.9	-1.30 ± 0.17	13	1.27
Inter-subunit					
α4-F286A	54.2 ± 1.5	0.054 – 0.058	-0.9 ± 0.3	2	1.64
β2-I218A	60.9 ± 1.2	0.03 – 0.56	-1.1 ± 0.2	4	1.85
α4-G281A + β2-I218A	23.8 ± 1.1	0.5 – 3.6	-2.2 ± 0.3	6	0.72
Channel Pore					
α4-L265A	21.1 ± 1.2	0.4 – 1.1	-1.2 ± 0.2	3	0.64
β2-L257A	62.8 ± 1.2	0.5 – 13.2	-1.1 ± 0.2	3	1.91

Fold = (mutant EC_{50} or IC_{50})/(wildtype EC_{50} or IC_{50})
NR = non-responsive

Appendix 1

MOLECULAR DYNAMICS SIMULATION SYSTEM SETUP AND EQUILIBRATION FOR THE HUMAN α4β2 NACHR

*The work described in this section was done and written by Shyam Saladi with minor adaptations by Betty Wong.

Modeling

To model the human α4β2 nAChR, the X-ray crystal structure (PDB 5kxi) of the human α4β2 nAChR resolved to 3.94Å[10] was used as the starting template. The structure omitted a number of missing residues both as a result of the genetic modifications to improve protein expression and as a result of lack of density after X-ray crystallography. Residues unable to be resolved from the crystallography are shown in Appendix 1.1.

We performed a sequence alignment between the protein sequence of the expression construct and the native α4 and β2 protein sequences to determine any additional residues with MAFFT using G-INS-i[68]. As expected, this analysis shows the replacement of the M3-M4 linker by the "MX" linker as noted by Morales-Perez, et al. but no additional missing residues. Since Morales-Perez, et al. show that this construct has functionally similar activity to the full-length protein, and since known allosteric modulators are not found to bind in this region[69], we choose to model the α4β2 structure with the MX linker. Given the lack of direct structural information for the entire M3-M4 linker, further work may include the development of a reliable modelling procedure and experimental assays to ascertain the atomistic structure of this region. Missing residues were then modeled using Modeller[70] (see Appendix 1.1) using a harmonic lower bound restraint on the N- and C-terminal regions to ensure they did not enter the membrane plane.

Building the System

With a set of full, contiguous subunit chains, protons were added, and geometry was checked and fixed using Reduce[71]. The simulation system was built using CHARMM-GUI[72-74]. Disulfide bonds and the protonation state of ionizable side chains were determined using Propka[75-76] and specified to CHARMM-GUI for patching.

The system was built into a hexagonal box to minimize "dead" volume within the simulation cell with 20 Å of spacing in the z-direction (*i.e.* along pore axis of the protein) between periodic images. The lipid membrane was built using POPC lipids at 1.5 times the size of the protein in the x-y plane again to provide adequate room to avoid the protein from interacting with its periodic images. As the crystal structure does not provide direct information on the position of the lipid membrane, the location was calculated using OPM[77] omitting the entire MX linker since, as an interfacial segment, it can complicate this orientation calculation. The final model does include the MX region, as noted above.

The system was solvated with TIP3P water and then neutralized and brought to 150 mM NaCl using CHARMM-GUI's Monte-Carlo replacement method for a total of 436,742 atoms. All standard residues were assigned CHARMM36 force field parameters.[78-79] Non-standard residues (*i.e.* nicotine, menthol) were parameterized using CGenFF[80] (Appendix 1.3) and manually verified to be physically reasonable.

Molecular Dynamics

The system was gradually equilibrated by the stepwise reduction of initially imposed restraints before a production simulation by modifying the procedure provided by CHARMM-GUI (see Appendix 1.2). The initial system was first energy minimized with conjugate gradient descent for 1,000 steps to eliminate poor contacts. The surface tension of the membrane was targeted to 17 dyne/cm, which has been shown to reproduce bulk experimental measurements for POPC membranes[81]. All simulations were carried out with GPU-accelerated NAMD 2.12[82] for a total simulation time of 100 ns with all other simulation parameters provided in Appendix 1.2.

Docking

Snapshots of the protein at its initial state (*i.e.* 0 ns), at 2.5 ns, and at 100 ns of production dynamics were taken and used for menthol docking (See Chapter 6 Methods). Poses were manually filtered for uniqueness and then built into the system at 100ns; poses docked to an earlier snapshot were inserted after aligning the protein to the 100ns snapshot. Each pose was then inspected within the context of the entire system for egregious contacts (*e.g.* lipid piercing to the menthol ring) and fixed by moving the non-menthol residue. The stability of the pose was then assessed by at least 5000 steps of conjugate gradient minimization to minimize any problematic contacts (*e.g.* steric clashes) followed by 1ns of molecular dynamics using the same setup as the production simulation described above.

Appendix 1.1 Modeling missing residues

Missing residues that were either unresolved or truncated on the X-ray structure (PDB 5kxi) were determined through a sequence alignment. In summary, the following residues were missing and needed to be built.

- On the α4 subunit
  - 7 residues at the N terminus
  - 11 residues on the MX linker (between M3 and M4)
  - 5 residues at the C terminus
- On the β2 subunit
  - 15 residues on the MX linker (between M3 and M4)
  - 30 residues at the C terminus (including the Strep-tag)

Highlighted residues indicate that they were built using Modeller:

α4 Subunit Alignment

N-terminus

```
5KXI:A,D_SOLVED ---------------------------------AHAEERLLKKLFSGYNKWSRPVANISD
Hs_ACHA4_P43681 MELGGPGAPRLLPPLLLLLGTGLLRASSHVETRAHAEERLLKKLFSGYNKWSRPVANISD
5KXI:A,D_FULL   -------------------------SSHVETRAHAEERLLKKLFSGYNKWSRPVANISD
```

M3-M4 linker through C-terminus

```
5KXI:A,D_SOLVED LVIPLIGEYLLFTMIFVTLSIVITVFVLNVHHRSPRTHTMPTWVRRVFLDIVPRLLL---
Hs_ACHA4_P43681 LVIPLIGEYLLFTMIFVTLSIVITVFVLNVHHRSPRTHTMPTWVRRVFLDIVPRLLLMKR
5KXI:A,D_FULL   LVIPLIGEYLLFTMIFVTLSIVITVFVLNVHHRSPRTHTMPTWVRRVFLDIVPRLLLMKR

5KXI:A,D_SOLVED ------------------------------------------------------------
Hs_ACHA4_P43681 PSVVKDNCRRLIESMHKMASAPRFWPEPEGEPPATSGTQSLHPPSPSFCVPLDVPAEPGP
5KXI:A,D_FULL   PSVV--------------------------------------------------------

5KXI:A,D_SOLVED ------------------------------------------------------------
Hs_ACHA4_P43681 SCKSPSDQLPPQQPLEAEKASPHPSPGPCRPPHGTQAPGLAKARSLSVQHMSSPGEAVEG
5KXI:A,D_FULL   ------------------------------------------------------------

5KXI:A,D_SOLVED ------------------------------------------------------------
Hs_ACHA4_P43681 GVRCRSRSIQYCVPRDDAAPEADGQAAGALASRNTHSAELPPPDQPSPCKCTCKKEPSSV
5KXI:A,D_FULL   ------------------------------------------------------------

5KXI:A,D_SOLVED ---------------------------------------------ERSVKEDWKYVAMVI
Hs_ACHA4_P43681 SPSATVKTRSTKAPPPHLPLSPALTRAVEGVQYIADHLKAEDTDF--SVKEDWKYVAMVI
5KXI:A,D_FULL   ----------------------------------------DTDFERSVKEDWKYVAMVI

5KXI:A,D_SOLVED DRIFLWMFIIVCLLGTVGLFLPPW-----
Hs_ACHA4_P43681 DRIFLWMFIIVCLLGTVGLFLPPWLAGMI
5KXI:A,D_FULL   DRIFLWMFIIVCLLGTVGLFLPPWLAGMI
```

β2 Subunit Alignment

N-terminus

```
5KXI:B,C,E_SOLV ------------------------TDTEERLVEHLLDPSRYNKLIRPATNGSELVTVQL
Hs_ACHB2_P17787 MARRCGPVALLLGFGLLRLCSGVWGTDTEERLVEHLLDPSRYNKLIRPATNGSELVTVQL
5KXI:B,C,E_FULL ------------------------TDTEERLVEHLLDPSRYNKLIRPATNGSELVTVQL
```

M3-M4 linker through C-terminus

```
5KXI:B,C,E_SOLV LMFTMVLVTFSIVTSVCVLNVHHRSPTTHTMAPWVKVVFLEKLPALLF------------
Hs_ACHB2_P17787 LMFTMVLVTFSIVTSVCVLNVHHRSPTTHTMAPWVKVVFLEKLPALLFMQQPRHHCARQR
5KXI:B,C,E_FULL LMFTMVLVTFSIVTSVCVLNVHHRSPTTHTMAPWVKVVFLEKLPALLFMQQPRHH-----

5KXI:B,C,E_SOLV ------------------------------------------------------------
Hs_ACHB2_P17787 LRLRRRQREREGAGALFFREAPGADSCTCFVNRASVQGLAGAFGAEPAPVAGPGRSGEPC
5KXI:B,C,E_FULL ------------------------------------------------------------

5KXI:B,C,E_SOLV ----------------------------SEDWKYVAMVIDRLFLWIFVFVCVFGTIGMF
Hs_ACHB2_P17787 GCGLREAVDGVRFIADHMRSEDDDQ--SVSEDWKYVAMVIDRLFLWIFVFVCVFGTIGMF
5KXI:B,C,E_FULL ----------------------DDDQERSVSEDWKYVAMVIDRLFLWIFVFVCVFGTIGMF

5KXI:B,C,E_SOLV LQPL-----------------------------
Hs_ACHB2_P17787 LQPLFQNYTTTTFLHSDHSAPSSK----------
5KXI:B,C,E_FULL LQPLFQNYTTTTFLHSDHSAPSSKSAWSHPQFEK
```

Appendix 1.2 Simulation Parameters

General Parameters	
Nonbonded exclusion	scaled1-4 (unitary factor)
Cutoff distance	12 Å
Switch distance	10 Å
Pairlists distance	16 Å
Steps per cycle	20
Pairlists per cycle	2
Rigid bonds	All heavy to H
Electrostatics	Particle Mesh Ewald (spline order 6)
vdw Force Switching	Yes
Atom wrapping	All to nearest periodic image
Write frequency	
Restart file	1000 steps
Trajectory snapshot	1000 steps
Extended system snapshot	1000 steps
Energy calculation	125 steps
Timing estimate	1000 steps
Temperature and Pressure Control	
Damping	1.0
Coupled to hydrogens	Off
Barostat type	Nosé-Hoover
Piston target	1.01325 bar
Piston period	50 fs
Piston decay	25 fs
Surface tension	17 dyn/cm
Pressure control	Group
Unit cell	Flexible with constant x-y ratio

	Equilibration	*Production 1*	*Production 2*
Timestep	1 fs or 2 fs	2 fs	2 fs
Temperature reassignment	500 steps	NA	
Temperature	303.15 K		310.15 K
Non-bonded	Every step		
Full Electrostatics	Every step	Every other step	

Appendix 1.3 Force Field Parameters for Nicotine

Force field parameters for nicotine calculated by CGenFF

```
RESI NCT       1.000 ! param penalty=  95.000 ; charge penalty=  58.371
GROUP            ! CHARGE   CH_PENALTY
ATOM C1     CG3C52 -0.120 !   21.922
ATOM C2     CG3C53 -0.054 !   53.239
ATOM N3     NG3P1  -0.223 !   34.812
ATOM C4     CG3C54 -0.364 !   12.847
ATOM C5     CG3C52 -0.108 !   13.232
ATOM H6     HGA2    0.090 !    1.500
ATOM H7     HGA2    0.090 !    1.500
ATOM H8     HGA1    0.090 !    3.922
ATOM H9     HGA2    0.280 !    0.794
ATOM H10    HGA2    0.280 !    0.794
ATOM H11    HGA2    0.090 !    0.030
ATOM H12    HGA2    0.090 !    0.030
ATOM C13    CG2R61  0.177 !    0.000
ATOM C14    CG2R61 -0.114 !    2.150
ATOM C15    CG2R61 -0.122 !    5.722
ATOM C16    CG2R61  0.135 !   58.371
ATOM C17    CG2R61  0.166 !   10.101
ATOM N18    NG2R60 -0.602 !    7.891
ATOM H19    HGR62   0.122 !    0.000
ATOM H20    HGR61   0.115 !    0.000
ATOM H21    HGR61   0.115 !    0.340
ATOM H22    HGR62   0.122 !    0.390
ATOM C23    CG334   0.178 !   11.329
ATOM H24    HGA3    0.090 !    0.460
ATOM H25    HGA3    0.090 !    0.460
ATOM H26    HGA3    0.090 !    0.460
ATOM HN3    HGP2    0.297 !   19.436
```

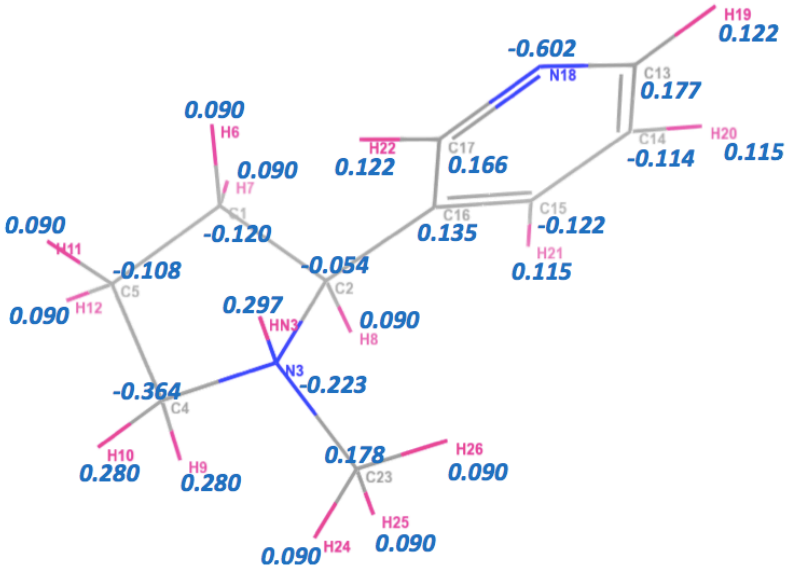

Appendix 1.4 Force Field Parameters for (–)-Menthol

Parameters are for the chair conformation of (–)-Menthol. The chair conformation of (–)-Menthol was built by Rezvan Shahoei in Emad Tajkhorshid's lab at University of Illinois at Urbana-Champaign.

```
RESI MEN       0.000 ! param penalty=   0.900 ; charge penalty=   0.213
GROUP            ! CHARGE   CH_PENALTY
ATOM C5     CG311  -0.091 !     0.000
ATOM C10    CG331  -0.268 !     0.000
ATOM H101   HGA3    0.090 !     0.000
ATOM H102   HGA3    0.090 !     0.000
ATOM H103   HGA3    0.090 !     0.000
ATOM H5     HGA1    0.090 !     0.000
ATOM C4     CG321  -0.182 !     0.000
ATOM H41    HGA2    0.090 !     0.000
ATOM H42    HGA2    0.090 !     0.000
ATOM C3     CG321  -0.178 !     0.190
ATOM H31    HGA2    0.090 !     0.000
ATOM H32    HGA2    0.090 !     0.000
ATOM C2     CG311  -0.103 !     0.070
ATOM C7     CG311  -0.079 !     0.064
ATOM C8     CG331  -0.273 !     0.045
ATOM H81    HGA3    0.090 !     0.000
ATOM H82    HGA3    0.090 !     0.000
ATOM H83    HGA3    0.090 !     0.000
ATOM C9     CG331  -0.273 !     0.045
ATOM H91    HGA3    0.090 !     0.000
ATOM H92    HGA3    0.090 !     0.000
ATOM H93    HGA3    0.090 !     0.000
ATOM H7     HGA1    0.090 !     0.000
ATOM H2     HGA1    0.090 !     0.000
ATOM C1     CG311   0.146 !     0.200
ATOM H1     HGA1    0.090 !     0.000
ATOM O1     OG311  -0.652 !     0.213
ATOM HO1    HGP1    0.419 !     0.000
ATOM C6     CG321  -0.176 !     0.000
ATOM H61    HGA2    0.090 !     0.000
ATOM H62    HGA2    0.090 !     0.000
```

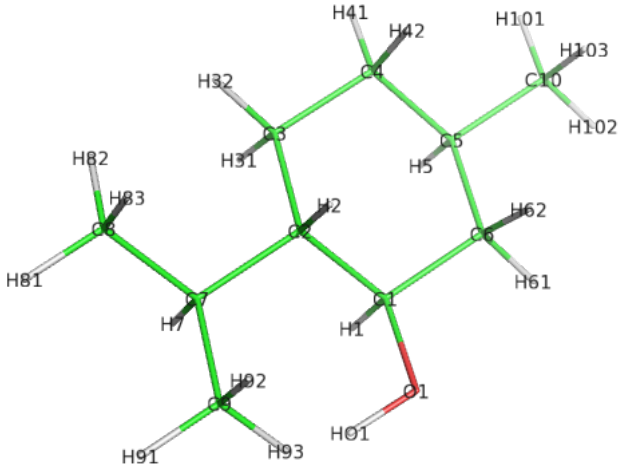

REFERENCES

1. Eric R. Kandel, J. H. S., Thomas M. Jessell, *Principles of Neural Science*. 2000; Vol. Fourth.
2. Bagal, S. K.; Brown, A. D.; Cox, P. J.; Omoto, K.; Owen, R. M.; Pryde, D. C.; Sidders, B.; Skerratt, S. E.; Stevens, E. B.; Storer, R. I.; Swain, N. A., Ion channels as therapeutic targets: a drug discovery perspective. *Journal of medicinal chemistry* **2013,** *56* (3), 593-624.
3. Van Arnam, E. B. Chemical-scale studies of G protein-coupled receptors and ligand-gated ion channels. Dissertation (Ph.D.), California Institute of Technology, 2014.
4. Unwin, N., Refined structure of the nicotinic acetylcholine receptor at 4A resolution. *Journal of molecular biology* **2005,** *346* (4), 967-89.
5. daCosta, C. J.; Baenziger, J. E., Gating of pentameric ligand-gated ion channels: structural insights and ambiguities. *Structure* **2013,** *21* (8), 1271-83.
6. Hurst, R.; Rollema, H.; Bertrand, D., Nicotinic acetylcholine receptors: from basic science to therapeutics. *Pharmacology & therapeutics* **2013,** *137* (1), 22-54.
7. Hogg, R. C.; Buisson, B.; Bertrand, D., Allosteric modulation of ligand-gated ion channels. *Biochemical pharmacology* **2005,** *70* (9), 1267-1276.
8. Katjus Ïa Brejc, W. J. v. D., Remco V. Klaassen, Mascha Schuurmans, John van der Oost, August B. Smit, Titia K. Sixma, Crystal structure of an ACh-binding protein reveals the ligand-binding domain of nicotinic receptors. *Nature* **2001,** *411*, 269-276.
9. Dellisanti, C. D.; Yao, Y.; Stroud, J. C.; Wang, Z. Z.; Chen, L., Crystal structure of the extracellular domain of nAChR alpha1 bound to alpha-bungarotoxin at 1.94 A resolution. *Nature neuroscience* **2007,** *10* (8), 953-62.
10. Morales-Perez, C. L.; Noviello, C. M.; Hibbs, R. E., X-ray structure of the human α4β2 nicotinic receptor. *Nature* **2016,** *538* (7625), 411-415.
11. Taly, A.; Corringer, P. J.; Guedin, D.; Lestage, P.; Changeux, J. P., Nicotinic receptors: allosteric transitions and therapeutic targets in the nervous system. *Nature reviews. Drug discovery* **2009,** *8* (9), 733-50.
12. Xiu, X.; Puskar, N. L.; Shanata, J. A.; Lester, H. A.; Dougherty, D. A., Nicotine binding to brain receptors requires a strong cation-pi interaction. *Nature* **2009,** *458* (7237), 534-7.
13. Carpenter, E. P.; Beis, K.; Cameron, A. D.; Iwata, S., Overcoming the challenges of membrane protein crystallography. *Current opinion in structural biology* **2008,** *18* (5), 581-6.
14. Gamper, N., *Ion Channels: Methods and Protocols*. Second ed.; Humana Press: 2013.
15. Wang, L.; Xie, J.; Schultz, P. G., EXPANDING THE GENETIC CODE. *Annual Review of Biophysics and Biomolecular Structure* **2006,** *35* (1), 225-249.
16. Monahan, S. L.; Lester, H. A.; Dougherty, D. A., Site-Specific Incorporation of Unnatural Amino Acids into Receptors Expressed in Mammalian Cells. *Chemistry & Biology* **2003,** *10* (6), 573-580.
17. Dougherty, D. A.; Van Arnam, E. B., In Vivo Incorporation of Non-canonical Amino Acids by Using the Chemical Aminoacylation Strategy: A Broadly Applicable Mechanistic Tool. *Chembiochem : a European journal of chemical biology* **2014**, n/a-n/a.
18. Van Arnam, E. Chemical-Scale Studies of G Protein-Coupled Receptors and Ligand-Gated Ion Channels. California Institute of Technology, Pasadena, CA, 2014.
19. Weber, W.-M., Ion currents of Xenopus laevis oocytes: state of the art. *Biochimica et Biophysica Acta (BBA) - Biomembranes* **1999,** *1421* (2), 213-233.
20. Miles, T. F.; Dougherty, D. A.; Lester, H. A., The 5-HT3AB receptor shows an A3B2 stoichiometry at the plasma membrane. *Biophysical journal* **2013,** *105* (4), 887-98.
21. Pantoja, R.; Rodriguez, E. A.; Dibas, M. I.; Dougherty, D. A.; Lester, H. A., Single-molecule imaging of a fluorescent unnatural amino acid incorporated into nicotinic receptors. *Biophysical journal* **2009,** *96* (1), 226-37.
22. Ramil, C. P. L., Q., Bioorthogonal chemistry: strategies and recent developments. *Chem Comm* **2013,** *49*, 11007-11022.

23.Devaraj, N. K.; Hilderbrand, S.; Upadhyay, R.; Mazitschek, R.; Weissleder, R., Bioorthogonal turn-on probes for imaging small molecules inside living cells. *Angewandte Chemie* **2010,** *49* (16), 2869-72.
24.Meimetis, L. G. C., JCT; Giedt, R. J.; Kohler, R. H.; Weissleder, R., Ultrafluorogenic Coumarin-Tetrazine Probes for Real-Time Biological Imaging. *Angewandte Chemie* **2014,** *53*, 1-5.
25.Carlson, J. C. T.; Meimetis, L. G.; Hilderbrand, S. A.; Weissleder, R., BODIPY–Tetrazine Derivatives as Superbright Bioorthogonal Turn-on Probes. *Angewandte Chemie International Edition* **2013,** *52* (27), 6917-6920.
26.Meimetis, L. G.; Carlson, J. C. T.; Giedt, R. J.; Kohler, R. H.; Weissleder, R., Ultrafluorogenic Coumarin–Tetrazine Probes for Real-Time Biological Imaging. *Angewandte Chemie International Edition* **2014,** *53* (29), 7531-7534.
27.Keller, R. C. A. S., J. R.; Dekruijff, B., Characterization of the Resonance Energy Transfer Couple Coumarin-BODIPY and Its Possible Applications in Protein-Lipid Research. *Biochemical and Biophysical Research Communications* **1995,** *207* (2), 508-514.
28.Saraogi, I. D. Z. S. C. S.-o. S., Site-Specific Fluorescent Labeling of Nascent Proteins on the Translating Ribosome. *Journal of the American Chemical Society* **2011,** *133* (38), 14936-14939.
29.Roy, R. H., Sungchul; Ha, Taekjip A practical guide to single-molecule FRET. *Nature methods* **2008,** *5* (6), 507-516.
30.Roy, R.; Hohng, S.; Ha, T., A practical guide to single-molecule FRET. *Nat Meth* **2008,** *5* (6), 507-516.
31.Gallivan, J. P.; Lester, H. A.; Dougherty, D. A., Site-specific incorporation of biotinylated amino acids to identify surface-exposed residues in integral membrane proteins. *Chemistry & Biology* **1997,** *4* (10), 739-749.
32.Nikić, I.; Plass, T.; Schraidt, O.; Szymański, J.; Briggs, J.; Schultz, C.; Lemke, E., Minimal tags for rapid dual-color live-cell labeling and super-resolution microscopy. *Angewandte Chemie (International ed. in English)* **2014,** *53* (8), 2245-2249.
33.Kaihang, W.; Amit, S.; Daniel, J. C.; Nabil, W. W.; Kathrin, L.; Stephen, W.; Ryan, A. M.; Jason, W. C., Optimized orthogonal translation of unnatural amino acids enables spontaneous protein double-labelling and FRET. *Nature Chemistry* **2014,** *6*.
34.Borisenko, V. L., T.; Hesse, J.; Füreder-Kitzmüller, E.; Fertig, N.; Behrends, J.C.; Woolley, G. A.; Schütz, G., Simultaneous optical and electrical recording of single gramacidin channels. *Biophysical journal* **2003,** *84*, 612-622.
35.Wiles, C.; Watts, P.; Haswell, S. J., Clean and selective oxidation of aromatic alcohols using silica-supported Jones' reagent in a pressure-driven flow reactor. *Tetrahedron Letters* **2006,** *47* (30), 5261-5264.
36.Yang, J.; Karver, M. R.; Li, W.; Sahu, S.; Devaraj, N. K., Metal-Catalyzed One-Pot Synthesis of Tetrazines Directly from Aliphatic Nitriles and Hydrazine. *Angewandte Chemie International Edition* **2012,** *51* (21), 5222-5225.
37.Soenen, D. R.; Zimpleman, J. M.; Boger, D. L., Synthesis and Inverse Electron Demand Diels−Alder Reactions of 3,6-Bis(3,4-dimethoxybenzoyl)-1,2,4,5-tetrazine. *The Journal of organic chemistry* **2003,** *68* (9), 3593-3598.
38.Wallrabe, H. P., Ammasi, Imaging protein molecules using FRET and FLIM microscopy. *Curr Opin Biotech* **2005,** *16*, 19-27.
39.Mannuzzu, L. M. M., M. M.; Isacoff, E. Y., Direct physical measure of conformational rearrangement underlying potassium channel gating. *Science* **1996,** *271*, 213-216.
40.Cha, A. B., F., Characterizing voltage-dependent conformational changes in the Shaker K+ channel with fluorescence. *Neuron* **1997,** *19*, 1127-1140.
41.Cha, A. S., G. E.; Selvin, P. R.; Benzanilla, F., Atomic scale movement of the voltage sensing region in a potassium channel measured via spectroscopy. *Nature* **1999,** *402* (809-813).
42.Weiss, S., Measuring conformational dynamics of biomolecules by single molecule fluorescence spectroscopy. *Nature Structural Biology* **2000,** *7*, 724-729.
43.Kelkar, D. A.; Chattopadhyay, A., The gramicidin ion channel: A model membrane protein. *Biochimica et Biophysica Acta (BBA) - Biomembranes* **2007,** *1768* (9), 2011-2025.
44.Piston, D. W.; Kremers, G. J., Fluorescent protein FRET: the good, the bad and the ugly. *Trends in biochemical sciences* **2007,** *32* (9), 407-14.
45.Berezin, M. Y. A., Samuel, Fluorescence Lifetime Measurements and Biological Imaging. *Chem Rev* **2010,** *110* (5), 2641-2684.

46.Digman, M. A.; Caiolfa, V. R.; Zamai, M.; Gratton, E., The Phasor Approach to Fluorescence Lifetime Imaging Analysis. *Biophysical journal* **2008,** *94* (2), L14-L16.
47.Day, R. N.; Davidson, M. W., Fluorescent proteins for FRET microscopy: monitoring protein interactions in living cells. *BioEssays : news and reviews in molecular, cellular and developmental biology* **2012,** *34* (5), 341-50.
48.Stringari, C.; Cinquin, A.; Cinquin, O.; Digman, M. A.; Donovan, P. J.; Gratton, E., Phasor approach to fluorescence lifetime microscopy distinguishes different metabolic states of germ cells in a live tissue. *Proceedings of the National Academy of Sciences* **2011,** *108* (33), 13582-13587.
49.Furr, H. C., Analysis of Retinoids and Carotenoids: Problems Resolved and Unsolved. *The Journal of Nutrition* **2004,** *134* (1), 281S-285S.
50.Blumberg, B.; Bolado, J.; Derguini, F.; Craig, A. G.; Moreno, T. A.; Chakravarti, D.; Heyman, R. A.; Buck, J.; Evans, R. M., Novel retinoic acid receptor ligands in Xenopus embryos. *Proceedings of the National Academy of Sciences* **1996,** *93* (10), 4873-4878.
51.Inc., I. Fluorescence Quantum Yields (QY) and Lifetimes (τ) for Alexa Fluor Dyes. https://www.thermofisher.com/us/en/home/references/molecular-probes-the-handbook/tables/fluorescence-quantum-yields-and-lifetimes-for-alexa-fluor-dyes.html.
52.Alberts B, J. A., Lewis J, et al. The Endoplasmic Reticulum. https://www.ncbi.nlm.nih.gov/books/NBK26841/.
53.Borst, J. W.; Willemse, M.; Slijkhuis, R.; van der Krogt, G.; Laptenok, S. P.; Jalink, K.; Wieringa, B.; Fransen, J. A. M., ATP Changes the Fluorescence Lifetime of Cyan Fluorescent Protein via an Interaction with His148. *PloS one* **2010,** *5* (11), e13862.
54.Organization, W. H. *Report on the global tobacco epidemic*; Geneva: World Health Organization, 2008.
55.Xiao, C.; Miwa, J. M.; Henderson, B. J.; Wang, Y.; Deshpande, P.; McKinney, S. L.; Lester, H. A., Nicotinic Receptor Subtype-Selective Circuit Patterns in the Subthalamic Nucleus. *The Journal of Neuroscience* **2015,** *35* (9), 3734.
56.D'Souza, M. S.; Markou, A., Neuronal Mechanisms Underlying Development of Nicotine Dependence: Implications for Novel Smoking-Cessation Treatments. *Addiction Science & Clinical Practice* **2011,** *6* (1), 4-16.
57.Ortells, M. O.; Barrantes, G. E., Tobacco addiction: a biochemical model of nicotine dependence. *Medical hypotheses* **2010,** *74* (5), 884-94.
58.Benowitz, N. L.; Herrera, B.; Jacob, P., 3rd, Mentholated cigarette smoking inhibits nicotine metabolism. *The Journal of pharmacology and experimental therapeutics* **2004,** *310* (3), 1208-15.
59.Alsharari, S. D.; King, J. R.; Nordman, J. C.; Muldoon, P. P.; Jackson, A.; Zhu, A. Z. X.; Tyndale, R. F.; Kabbani, N.; Damaj, M. I., Effects of Menthol on Nicotine Pharmacokinetic, Pharmacology and Dependence in Mice. *PloS one* **2015,** *10* (9), e0137070.
60.Ashley, M.; Dixon, M.; Sisodiya, A.; Prasad, K., Lack of effect of menthol level and type on smokers' estimated mouth level exposures to tar and nicotine and perceived sensory characteristics of cigarette smoke. *Regulatory toxicology and pharmacology : RTP* **2012,** *63* (3), 381-90.
61.Ahijevych, K.; Garrett, B. E., The role of menthol in cigarettes as a reinforcer of smoking behavior. *Nicotine & tobacco research : official journal of the Society for Research on Nicotine and Tobacco* **2010,** *12 Suppl 2*, S110-6.
62.Brody, A. L.; Mukhin, A. G.; La Charite, J.; Ta, K.; Farahi, J.; Sugar, C. A.; Mamoun, M. S.; Vellios, E.; Archie, M.; Kozman, M.; Phuong, J.; Arlorio, F.; Mandelkern, M. A., Up-regulation of nicotinic acetylcholine receptors in menthol cigarette smokers. *The international journal of neuropsychopharmacology* **2013,** *16* (5), 957-66.
63.Company, L. T. Characterization of Menthol. http://www.fda.gov/downloads/AdvisoryCommittees/CommitteesMeetingMaterials/TobaccoProductsScientificAdvisoryCommittee/UCM220039.pdf (accessed April 27, 2017).
64.Hans, M.; Wilhelm, M.; Swandulla, D., Menthol Suppresses Nicotinic Acetylcholine Receptor Functioning in Sensory Neurons via Allosteric Modulation. *Chemical Senses* **2012,** *37* (5), 463-469.
65.Ton, H. T.; Smart, A. E.; Aguilar, B. L.; Olson, T. T.; Kellar, K. J.; Ahern, G. P., Menthol Enhances the Desensitization of Human alpha3beta4 Nicotinic Acetylcholine Receptors. *Molecular pharmacology* **2015,** *88* (2), 256-64.
66.Dilger, J. P., The effects of general anaesthetics on ligand-gated ion channels. *BJA: British Journal of Anaesthesia* **2002,** *89* (1), 41-51.

67.Nury, H.; Van Renterghem, C.; Weng, Y.; Tran, A.; Baaden, M.; Dufresne, V.; Changeux, J. P.; Sonner, J. M.; Delarue, M.; Corringer, P. J., X-ray structures of general anaesthetics bound to a pentameric ligand-gated ion channel. *Nature* **2011,** *469* (7330), 428-31.
68.Katoh, K.; Standley, D. M., MAFFT multiple sequence alignment software version 7: improvements in performance and usability. *Molecular biology and evolution* **2013,** *30* (4), 772-80.
69.Wang, J.; Lindstrom, J., Orthosteric and allosteric potentiation of heteromeric neuronal nicotinic acetylcholine receptors. *British Journal of Pharmacology* **2017**, n/a-n/a.
70.Webb, B.; Sali, A., Comparative Protein Structure Modeling Using MODELLER. *Current protocols in bioinformatics* **2016,** *54*, 5.6.1-5.6.37.
71.Word, J. M.; Lovell, S. C.; Richardson, J. S.; Richardson, D. C., Asparagine and glutamine: using hydrogen atom contacts in the choice of side-chain amide orientation. *Journal of molecular biology* **1999,** *285* (4), 1735-47.
72.Jo, S.; Kim, T.; Iyer, V. G.; Im, W., CHARMM-GUI: A web-based graphical user interface for CHARMM. *Journal of Computational Chemistry* **2008,** *29* (11), 1859-1865.
73.Jo, S.; Kim, T.; Im, W., Automated Builder and Database of Protein/Membrane Complexes for Molecular Dynamics Simulations. *PloS one* **2007,** *2* (9), e880.
74.Lee, J.; Cheng, X.; Swails, J. M.; Yeom, M. S.; Eastman, P. K.; Lemkul, J. A.; Wei, S.; Buckner, J.; Jeong, J. C.; Qi, Y.; Jo, S.; Pande, V. S.; Case, D. A.; Brooks, C. L.; MacKerell, A. D.; Klauda, J. B.; Im, W., CHARMM-GUI Input Generator for NAMD, GROMACS, AMBER, OpenMM, and CHARMM/OpenMM Simulations Using the CHARMM36 Additive Force Field. *Journal of Chemical Theory and Computation* **2016,** *12* (1), 405-413.
75.Søndergaard, C. R.; Olsson, M. H. M.; Rostkowski, M.; Jensen, J. H., Improved Treatment of Ligands and Coupling Effects in Empirical Calculation and Rationalization of pKa Values. *Journal of Chemical Theory and Computation* **2011,** *7* (7), 2284-2295.
76.Olsson, M. H. M.; Søndergaard, C. R.; Rostkowski, M.; Jensen, J. H., PROPKA3: Consistent Treatment of Internal and Surface Residues in Empirical pKa Predictions. *Journal of Chemical Theory and Computation* **2011,** *7* (2), 525-537.
77.Lomize, A. L.; Pogozheva, I. D.; Mosberg, H. I., Anisotropic solvent model of the lipid bilayer. 2. Energetics of insertion of small molecules, peptides, and proteins in membranes. *Journal of chemical information and modeling* **2011,** *51* (4), 930-46.
78.Best, R. B.; Zhu, X.; Shim, J.; Lopes, P. E. M.; Mittal, J.; Feig, M.; MacKerell, A. D., Optimization of the additive CHARMM all-atom protein force field targeting improved sampling of the backbone φ, ψ and side-chain χ(1) and χ(2) dihedral angles. *Journal of chemical theory and computation* **2012,** *8* (9), 3257-3273.
79.Guvench, O.; Mallajosyula, S. S.; Raman, E. P.; Hatcher, E.; Vanommeslaeghe, K.; Foster, T. J.; Jamison, F. W.; MacKerell, A. D., CHARMM Additive All-Atom Force Field for Carbohydrate Derivatives and Its Utility in Polysaccharide and Carbohydrate–Protein Modeling. *Journal of Chemical Theory and Computation* **2011,** *7* (10), 3162-3180.
80.Vanommeslaeghe, K.; Hatcher, E.; Acharya, C.; Kundu, S.; Zhong, S.; Shim, J.; Darian, E.; Guvench, O.; Lopes, P.; Vorobyov, I.; Mackerell, A. D., Jr., CHARMM general force field: A force field for drug-like molecules compatible with the CHARMM all-atom additive biological force fields. *J Comput Chem* **2010,** *31* (4), 671-90.
81.Skjevik, A. A.; Madej, B. D.; Walker, R. C.; Teigen, K., LIPID11: a modular framework for lipid simulations using amber. *The journal of physical chemistry. B* **2012,** *116* (36), 11124-36.
82.Phillips, J. C.; Braun, R.; Wang, W.; Gumbart, J.; Tajkhorshid, E.; Villa, E.; Chipot, C.; Skeel, R. D.; Kale, L.; Schulten, K., Scalable molecular dynamics with NAMD. *J Comput Chem* **2005,** *26* (16), 1781-802.